# Development of a tandem mass spectrometer for probing high-energy electron transfer dissociation

**Hirofumi Nagao**

*Division of Sustainable Energy and Environmental Engineering,*
*Graduate School of Engineering, Osaka University*

March 2010

# Development of a tandem mass spectrometer for probing high-energy electron transfer dissociation

**Hirofumi Nagao**

*Division of Sustainable Energy and Environmental Engineering,*
*Graduate School of Engineering, Osaka University*

March 2010

Director

Professor Kunio Awazu

Reviewer

Professor Hiroshi Horiike
Professor Shigehiro Nishijima
Associate Professor Michisato Toyoda

# Contents

# Abbreviation List

- mass spectrometry (MS)
- mass-to-charge ratio (m/z)
- matrix-assisted laser desorption/ionization (MALDI)
- electrospray ionization (ESI)
- tandem mass spectrometry (MS/MS)
- posttranslational modification (PTMs)
- electron ionization (EI)
- fast atom bombardment (FAB)
- first mass spectrometer (MS-1)
- infrared ray (IR)
- ultraviolet (UV)
- second mass spectrometer (MS-2)
- time-of-flight (TOF)
- tandem TOF mass spectrometers with MALDI ion source (MALDI-TOF/TOF)
- collision induced dissociation (CID)
- multi-turn tandem TOF mass spectrometer (MULTUM-TOF/TOF)
- electron transfer dissociation (ETD)
- microchannel plate (MCP)
- fragmentation efficiency (FE)
- collection efficiency (CE)
- electron capture dissociation (ECD)
- fourier transform ion cyclotron resonance mass spectrometer (FT-ICR MS)
- tandem TOF mass spectrometer with ESI ion source (ESI-TOF/TOF)
- electrostatic analyzer (ESA)
- density functional theory (DFT)
- multistage mass spectrometry ($MS^n$)
- spherical jellium model (SJM)
- closed-shell (CS)
- negative to neutral to positive (NeNePo)
- kinetic energy release (KER)
- collisional activation (CA)

- ionization energy (IE)
- appearance energy (AE)
- bond energy (BE)
- dissociation energy (DE)
- orthogonal acceleration (OA)

# Unit List

- Amount of substance (mol)
- Current (A)
- Angle (°)
- Efficiency (%)
- Energy (eV)
- Frequency (Hz)
- Length (m)
- Mass (g)
- Pressure (Pa)
- Temperature (℃)
- Time (s)
- Voltage (V)

# Chapter 1

## Introduction

### Mass spectrometry (MS)

Mass spectrometry (MS) is a powerful analytical technique that is used to identify unknown compounds, to quantify known compounds, and to elucidate the structure and chemical properties of molecules. Detection of compounds can be accomplished with very minute quantities (as little as $10^{-12}$ g, or $10^{-15}$ moles for a compound of mass 1000 Daltons). This means that compounds can be identified at very low concentrations (one part in $10^{12}$) in chemically complex mixtures. As a result, MS is widely used, e.g., to determine the composition of molecular species found in space, to detect and identify the use of steroids in athletes, and to establish the elemental composition of semiconductor materials. Thus MS is now an indispensable tool in chemistry, physics, biology, pharmacy, and medicine because of its high sensitivity and specificity.

The basic principle of MS is to generate ions from inorganic or organic compounds by any suitable methods, to separate these ions by their *mass-to-charge ratio* (*m/z*) and to identify them by their respective *m/z* and abundance. Various methods have been developed for ionization and separation, allowing compounds to be analyzed efficiently for any purpose. Continuous development and improvement of instruments and techniques have expanded the range of MS research and applications. For example, MS has become one of the most useful tools in the analysis of biological samples such as proteins and peptides, since the development of "soft" ionization methods such as matrix-assisted laser desorption/ionization (MALDI) [1-5] and electrospray ionization (ESI) [6-8]. The continuing development and improvement of instruments and techniques is therefore necessary further to expand the scope of this technique.

Currently, the structural analysis of many biological samples is readily performed using MS. However, it is still often insufficient for the determination of protein and peptide structure. In order to determine their structure completely, high sensitivity, high mass resolution, and high mass accuracy are required in MS instruments, and there is at present much room for improvement. MS instruments capable of determining the structure of biological samples efficiently are in high demand. In view of this pressing

need, the development of new MS instruments for the structural analysis of biological samples is described in this thesis.

## Tandem mass spectrometry (MS/MS)

The function of proteins and peptides is related to their structure (e.g., amino acid sequence, type and site of post-translational modifications (PTMs)). For this reason, in order to investigate a protein's function, it is necessary to determine its structure. For example, PTMs such as phosphorylation, sulfation, and glycosylation of proteins are of great importance in the activation, localization, and regulation of protein function in vivo. Thus, identifying PTMs of proteins of interest will provide insights into their function and, in the long run, benefit the study of many diseases. It is therefore clear that the determination of protein and peptide structure is one of the most important goals in bioscience.

Although a single MS analysis provides mass information, it often provides little structural information. In such biological applications, two coupled stages of mass analysis, termed "tandem mass spectrometry (MS/MS) [9-11]", are required in order fully to identify and characterize proteins. A schematic view of MS/MS is shown in Fig. 1.1.

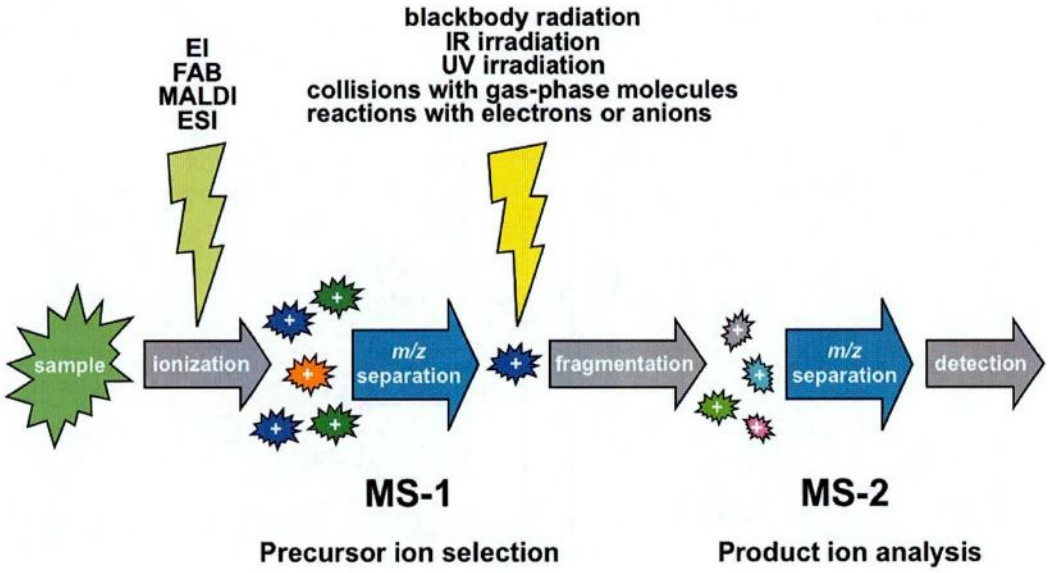


**Fig. 1.1.** Schematic view of MS/MS experiments.

In such experiments, the sample is ionized by various methods such as electron ionization (EI) [12], fast atom bombardment (FAB) [13-16], MALDI, and ESI. The first mass spectrometer (MS-1) provides separation and selection based upon the *m/z* of the ions, called precursor ions. Mass-selected precursor ions are then fragmented by various dissociation methods. There is a variety of excitation methods which have been used to generate peptide fragments, including blackbody radiation [17], infrared (IR) multiphoton excitation [18], ultraviolet (UV) laser excitation [19-23], and collisions with a target gas [24] or surfaces [25]. The ions formed by these excitation methods are called product ions. The product ions are once again mass-separated based upon their *m/z* values by the second mass spectrometer (MS-2) and then detected. Various types of mass spectrometers, such as magnetic sector [26-28], time-of-flight (TOF) [3, 29, 30], ion trap [31-34], and quadrupole mass analyzer [35,36], are used as MS-1 and MS-2.

Roepstorff and Fohlman have proposed a fragmentation notation for peptide fragmentation [37,38], as shown in Figure 1.2. Charge retention on the N terminus leads to ions defined as *a*, *b*, and *c*, while charge retention on the C terminus produces ions defined as *x*, *y*, and *z*. The *d*-, *v*-, and *w*-type ions are formed by the loss of side chains of *a*-, *y*-, and *z*-type ions, respectively. Structural information on proteins and peptides can be obtained from these fragment ion peaks, and therefore MS/MS is now widely used in protein biochemistry and in proteomics for the identification and characterization of proteins [39].

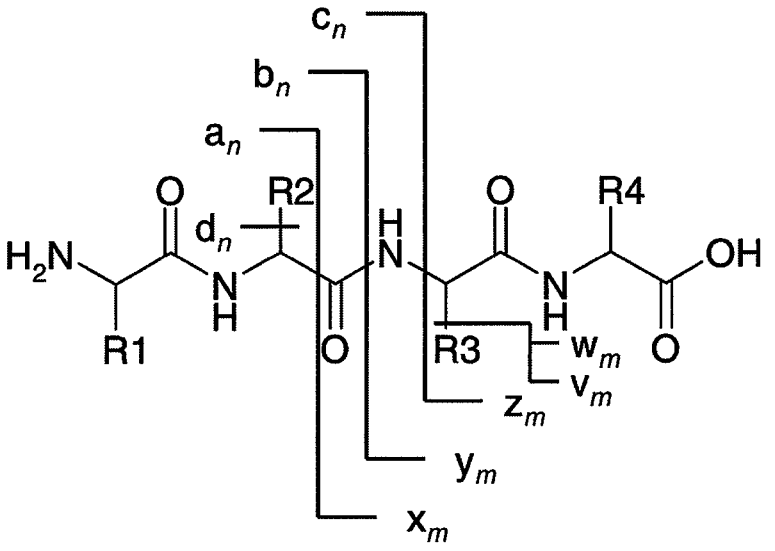


**Fig. 1.2.** Peptide fragmentation notation.

## Tandem time-of-flight (TOF) mass spectrometry

Structural analysis using MALDI in combination with MS/MS has been used quite extensively in structural biochemistry [40,41]. For example, tandem mass spectrometers with a MALDI ion source have been developed in which a magnetic sector [42], an ion trap [43], or a quadrupole mass analyzer [44] has been used as the MS-1 with the TOF mass spectrometer as the MS-2. Instruments in which both the MS-1 and MS-2 are TOF mass spectrometers, so-called "tandem TOF mass spectrometers", have also been constructed [45-49]. The pulsed nature of MALDI sources allows the use of relatively simple TOF mass spectrometers, which can generate a complete mass spectrum per ionization event, with, in principle, unlimited mass range. The capability of TOF mass spectrometers to collect all ions simultaneously makes them suitable as the MS-2 of tandem mass spectrometers with a MALDI ion source. As a result, tandem TOF mass spectrometers have excellent sensitivity. Currently, various tandem TOF mass spectrometers with a MALDI ion source, "MALDI-TOF/TOF", have been developed and are widely used for analyses of biological samples [45-49].

High-energy collision-induced dissociation (CID) is generally adopted as the dissociation method in MALDI-TOF/TOF. In this method, mass-selected precursor ions are accelerated to kinetic energies of 1 - 20 keV and allowed to collide with a target gas (usually a rare gas) under single collision conditions. When only a fraction of the collision energy in the center-of-mass system is converted into internal energy of the precursor ions, the precursor ions are fragmented. The high internal energy of the excited ions then produces a variety of backbone fragmentations (yielding N-terminal *a*-, *b*-, and C-terminal *y*-fragment ions) as well as side-chain fragmentations (yielding N-terminal *d*- and C-terminal *v*-, *w*-fragment ions) [50-54].

Recently, a new multi-turn tandem TOF/TOF mass spectrometer "MULTUM-TOF/TOF" was designed and constructed in our group [49, 55, 56], consisting of a MALDI ion source, a multi-turn TOF mass spectrometer, a collision cell, and a quadratic-field ion mirror. The multi-turn TOF mass spectrometer [57-60] overcame the problem of precursor ion selection in TOF mass spectrometers arising from insufficient time separation between two adjacent TOF peaks, by forcing the ions to fly in a closed orbit and passing around the same orbit many times. As a result, the mass resolution in precursor ion selection increased with increasing total TOF. The quadratic-field ion mirror, which was itself a type of a TOF mass spectrometer, allowed

high resolution in simultaneous fragment ion separation. It was demonstrated that MULTUM-TOF/TOF was useful for the structural analysis of biological molecules such as polypeptides [49], phosphopeptides [55], and phosphatides [56]. As is the case with MALDI-TOF/TOF in general, this method also suffered from the low efficiency (ca. 5 - 10%) of high-energy CID [61-63]. Improving the dissociation efficiency of TOF/TOF would allow measurements of small amount of sample, thus expanding the applicability of this technique. For these reasons, the enhancement of the dissociation efficiency of TOF/TOF is one of the most important research challenges in tandem TOF mass spectrometry.

## High-energy electron transfer dissociation (ETD)

In this thesis, a new dissociation method using alkali metal targets, termed "high-energy electron transfer dissociation (ETD)", is proposed as an alternative to high-energy CID in order to enhance the dissociation efficiency of TOF/TOF. Additionally, two types of tandem mass spectrometers (tandem magnetic sector type and tandem TOF type) for performing high-energy ETD experiments were developed. Using the magnetic sector instrument, the dissociation efficiency of high-energy ETD was evaluated by comparing fragment ion intensities in high-energy CID and high-energy ETD spectra of protonated polypeptides. In addition, the usefulness of high-energy ETD in structural analysis was demonstrated by measuring spectra of protonated polypeptides and phosphopeptides. After this evaluation, a tandem TOF mass spectrometer for performing high-energy ETD experiments was developed.

## Outline of this thesis

### Chapter 2:

The improvement of dissociation efficiency in TOF/TOF mass spectrometry is a significant problem in the biosciences. Improved efficiency would allow the measurements of small amount of sample, expanding the range of applicability of this technique. It was found necessary to investigate the root causes of the low efficiency of high-energy CID before attempting to enhance this efficiency, as discussed in this chapter. In brief, this low efficiency could be attributed to the small cross section ($10^{-16}$ $cm^2$) of collisional excitation using rare gases. Accordingly, it was proposed that alkali metal targets be used as the collision gas. These targets had larger cross sections ($10^{-14}$

$cm^2$) for electron transfer and generated excited species by electron transfer from the alkali metal target to the positive ions with high efficiency. The larger excited cross section was found to be advantageous for the dissociation of biomolecular ions in this research. This new dissociation method using alkali metal targets was termed "high-energy ETD". The principles of high-energy ETD will be described in this chapter.

**Chapter 3:**

In order to investigate the dissociation efficiency of high-energy ETD and evaluate its usefulness in structural analysis, a prototype tandem sector mass spectrometer was developed for performing high-energy ETD experiments. The concept of this instrument will be described here.

**Chapter 4:**

Because it was thought important to understand the differences in dissociation behavior between rare gas targets and alkali metal targets, both types of dissociation were investigated. The dissociation of inorganic samples, which are simple species, was investigated at first since the analysis of biological samples is rather more difficult. Some samples such as silver bromide and tungsten hexacarbonyl were initially used. In section 4.2, unimolecular dissociation and high-energy CID of $Ag_xBr^+$ ($x$ = 2, 4, 6, 8, 10) clusters were investigated using a rare gas target. In section 4.3, dissociation channels for the silver bromide cluster $Ag_2Br$ and the silver cluster $Ag_3$ and their ions were studied using an alkali metal target. In section 4.4, high-energy ETD of doubly charged tungsten hexacarbonyl $W(CO)_6^{2+}$ ions was investigated using alkali metal targets. It was expected that fundamental data obtained by these investigation would prove useful in interpreting the high-energy ETD experiments on biomolecular ions. The results presented in sections 4.2 - 4.4 indicated that this instrument had the potential to generate high-energy ETD spectra of inorganic ions. However, its sensitivity and mass range were insufficient to obtain high-energy ETD spectra of biomolecular ions, and therefore needed to be improved. After the necessary improvements were made, high-energy ETD spectra of polypeptides (Section 4.5) and phosphopeptides (Section 4.6) were measured. The results from these polypeptides demonstrated that high-energy ETD allowed the determination of their amino acid sequence. In addition, the efficiency

of high-energy ETD was about six times higher than that of high-energy CID. The results from phosphopeptides indicated that the high-energy ETD did not depend strongly on the type of phosphorylated amino acid, and therefore that this method was useful in determining the amino acid sequence of phosphopeptides, and also the positions of the phosphate groups in these molecules.

**Chapter 5:**

The results of chapter 4 demonstrated the usefulness of high-energy ETD in the structural analysis of biomolecular ions. However, the mass resolution of MS-2 and the sensitivity of the tandem magnetic sector mass spectrometer were not enough to study larger biological molecules. A new tandem TOF mass spectrometer with an ESI ion source "ESI-TOF/TOF" was designed and constructed in order to achieve the desired aim of high resolution in fragment ion analysis, high quality structural information via high-energy ETD, and simultaneous detection of all fragment ions. It consisted of an orthogonal accelerator ESI ion source, a linear TOF mass spectrometer, a collision cell for alkali metal targets, a quadratic-field ion mirror, and a microchannel plate (MCP) detector. High-energy ETD spectra of doubly protonated angiotensin II, substance P, bradykinin, and phosphopeptides could be obtained. Several *c*- and *z*-type fragment ions formed by the high-energy ETD process could be clearly observed in all cases. It was therefore demonstrated that high-energy ETD could be performed in ESI-TOF/TOF, desirable for the structural analysis of tryptic peptides.

**Chapter 6:**

The achievements of this study and directions for future research are summarized.

## References


[1] M. Karas, D. Bachmann, U. Bahr, F. Hillenkamp, Int. J. Mass Spectrom. Ion Process. 78 (1987) 53.

[2] M. Karas, F. Hillenkamp, Anal. Chem. 60 (1988) 2299.

[3] M. Karas, J. Mass Spectrom. 32 (1997) 1.

[4] M. Karas, D. Bachmann, F. Hillenkamp, Anal. Chem. 57 (1985) 2935.

[5] M. Karas, U. Bahr, A. Ingendoh, F. Hillenkamp, Angew. Chem. 101 (1989) 805.

[6] J.B. Fenn, M. Mann, C.K. Meng, S.F. Wong, C.M. Whitehouse, Science 246 (1989) 64.

[7] J.B. Fenn, M. Mann, C.K. Meng, S.F. Wong, C.M. Whitehouse, Mass Spectrom. Rev. 9 (1990) 37.

[8] R.D. Smith, J.A. Loo, C.G. Edmonds, C.J. Barinaga, H.R. Udseth, Anal. Chem. 62 (1990) 882.

[9] J.R. Chapman, *In Protein and Peptide Analysis by Mass Spectrometry*, Humana Press, New Jersey, 1996.

[10] W.S. Hancock, *In New Methods in Peptide Mapping for the Characterization of Proteins*, CRC press, Boca Raton, 1996.

[11] M. Kinter, N.E. Sherman, *In Protein Sequencing and Identification Using Tandem Mass Spectrometry*, Wiley Interscience, New York, 2000; .

[12] F.H. Field, J.L. Franklin, *In Electron Impact Phenomena and the Properties of Gaseous Ions; 1st ed*, Academic Press, New York, 1957.

[13] M. Barber, R.S. Bordoli, G.J. Elliott, R.D. Sedgwick, A.N. Tyler, Anal. Chem. 54 (1982) 645A.

[14] H.R. Morris, M. Panico, M. Barber, R.S. Bordoli, R.D. Sedgwick, A. Tyler, Biochem. Biophys. Res. Commun. 101 (1981) 623.

[15] M. Barber, R.S. Bordoli, R.D. Sedgwick, A.N. Tyler, J. Chem. Soc, Chem. Commun. (1981) 325.

[16] M. Barber, R.S. Bordoli, R.D. Sedgwick, A.N. Tyler, Nature 293 (1981) 270.

[17] W.D. Price, P.D. Schnier, E.R. Williams, Anal. Chem. 68 (1996) 859.

[18] D.P. Little, J.P. Speir, M.W. Senko, P.B. O'Connor, F.W. McLafferty, Anal. Chem. 66 (1994) 2809.

[19] W.D. Bowers, S.S. Delbert, R.L. Hunter, R.T. McIver Jr., J. Am. Chem. Soc. 106 (1984) 7288.

[20] S.A. Martin, J.A. Hill, C. Kittrell, K. Biemann, J. Am. Soc. Mass Spectrom. 1 (1990) 107.

[21] D.C. Barbacci, D.H. Russell, J. Am. Soc. Mass Spectrom. 10 (1999) 1038.

[22] J.Y. Oh, J.H. Moon, M.S. Kim, J. Am. Soc. Mass Spectrom. 15 (2004) 1248.

[23] M.S. Thompson, W. Cui, J.P. Reilly, Angew. Chem., Int. Ed. 43 (2004) 4791.

[24] D.F. Hunt, W.M. Bone, J. Shabanowitz, J. Rhodes, J.M. Ballard, Anal. Chem. 53 (1981) 1704.

[25] E.R. Williams, K.D. Henry, F.W. McLafferty, J. Shabanowitz, D.F. Hunt, J. Am. Soc. Mass Spectrom. 1 (1990) 413.

[26] A.O. Nier, Int. J. Mass Spectom. Ion Process. 100 (1990) 1.

[27] A.O. Nier, J. Am. Soc. Mass Spectrom. 2 (1991) 447.

[28] A.O. Nier, J. Chem. Educ. 66 (1989) 385.

[29] M.M. Wolff, W.E. Stephens, Rev. Sci. Instrum. 24 (1953) 616.

[30] W.C. Wiley, I.H. McLaren, Rev. Sci. Instrum. 26 (1955) 1150.

[31] R.E. March, R.J. Hughes, *In Quadrupole Storage Mass Spectrometry*, John Wiley & Sons, Chichester, 1989.

[32] R.E. March, Rapid Commun. Mass Spectrom. 12 (1998) 1543.

[33] R.E. March, Int. J. Mass Spectom. 200 (2000) 285.

[34] G. Stafford, J. Am. Soc. Mass Spectrom. 13 (2002) 589.

[35] W. Paul, M. Raether, Z. Phys 140 (1955) 262.

[36] W. Paul, H. Steinwedel, Z. Naturforsch 8A (1953) 448.

[37] K. Biemann, Biol. Mass Spectrom. 16 (1988) 99.

[38] P. Roepstorff, J. Fohlman, Biomed. Mass Spectrom. 11 (1984) 601.

[39] R. Aebersold, M. Mann, Nature 422 (2003) 198.

[40] M. Tyers, M. Mann, Nature 422 (2003) 193.

[41] S. Hanash, Nature 422 (2003) 226.

[42] U.N. Andersen, A.W. Colburn, A.A. Makarov, E.N. Raptakis, D.J. Reynolds, P.J. Derrick, S.C. Davis, A.D. Hoffman, S. Thomson, Rev. Sci. Instrum. 69 (1998) 1650.

[43] R.L. Martin, F.L. Brancia, Rapid Commun. Mass Spectrom. 17 (2003) 1358.

[44] H.R. Morris, T. Paxton, A. Dell, J. Langhorne, M. Berg, R.S. Bordoli, J. Hoyes, R.H. Bateman, Rapid Commun. Mass Spectrom. 10 (1996) 889.

[45] M.M. Cordero, T.J. Cornish, R.J. Cotter, J. Am. Soc. Mass Spectrom. 7 (1996)

590.

[46] D.J. Beussman, P.R. Vlasak, R.D. McLane, M.A. Seeterlin, C.G. Enke, Anal. Chem. 67 (1995) 3952.

[47] A.E. Giannakopulos, B. Thomas, A.W. Colburn, D.J. Reynolds, E.N. Raptakis, A.A. Makarov, P.J. Derrick, Rev. Sci. Instrum. 73 (2002) 2115.

[48] M.A. Seeterlin, P.R. Vlasak, D.J. Beussman, R.D. McLane, C.G. Enke, J. Am. Soc. Mass Spectrom. 4 (1993) 751.

[49] M. Toyoda, A.E. Giannakopulos, A.W. Colburn, P.J. Derrick, Rev. Sci. Instrum. 78 (2007) 074101.

[50] K. Biemann, S.A. Martin, Mass Spectrom. Rev. 6 (1987) 1.

[51] R.S. Johnson, S.A. Martin, K. Biemann, Int. J. Mass Spectom. Ion Process. 86 (1988) 137.

[52] R.A.J. O'Hair, M.L. Styles, G.E. Reid, J. Am. Soc. Mass Spectrom. 9 (1998) 1275.

[53] I.A. Papayannopoulos, Mass Spectrom. Rev. 14 (1995) 49.

[54] J.T. Stults, J. Lai, S. McCune, R. Wetzel, Anal. Chem. 65 (1993) 1703.

[55] S. Shimma, H. Nagao, A.E. Giannakopulos, S. Hayakawa, K. Awazu, M. Toyoda, J. Mass Spectrom. 43 (2008) 535.

[56] S. Shimma, H. Nagao, M. Toyoda, J. Mass Spectrom. Soc. Jpn. 55 (2007) 343.

[57] D. Okumura, M. Toyoda, M. Ishihara, I. Katakuse, J. Mass Spectrom. 39 (2004) 86.

[58] D. Okumura, M. Toyoda, M. Ishihara, I. Katakuse, Nucl. Inst. Meth Phys. Res. A 519 (2004) 331.

[59] M. Toyoda, M. Ishihara, S. Yamaguchi, H. Ito, T. Matsuo, R. Roll, H. Rosenbauer, J. Mass Spectrom. 35 (2000) 163.

[60] M. Toyoda, D. Okumura, M. Ishihara, I. Katakuse, J. Mass Spectrom. 38 (2003) 1125.

[61] G.L. Glish, P.J. Todd, Anal. Chem. 54 (1982) 842.

[62] F.W. McLafferty, P.J. Todd, D.C. McGilvery, M.A. Baldwin, J. Am. Chem. Soc. 102 (1980) 3360.

[63] G.L. Glish, S.A. McLuckey, T.Y. Ridley, R.G. Cooks, Int. J. Mass Spectom. Ion Phys. 41 (1982) 157.

# Chapter 2

## High-energy electron transfer dissociation (ETD)

### 2.1 Introduction

MALDI-TOF/TOF is useful in the structural analysis of biological samples. However, it is disadvantageous that the high-energy CID efficiency is low [1-3]. If the dissociation efficiency of TOF/TOF is improved, it is expected that the measurements of micro amount of samples are offered, and then the range of researches and applications is expanded. Therefore improving the dissociation efficiency of TOF/TOF is important. In order to enhance the dissociation efficiency, it is essential to investigate the cause of the low efficiency of high-energy CID. In this chapter, high-energy CID efficiency will be discussed in the beginning. Subsequently, the dissociation method to overcome the low efficiency of high-energy CID will be discussed.

The reaction scheme of high-energy CID is shown in the following scheme (2-1),

**Scheme (2-1)**

$$AB^+ + T \rightarrow AB^{+*} + T,$$

$$AB^{+*} \rightarrow A^+ + B \text{ (or } A + B^+),$$

where $AB^+$ and T indicate a precursor ion and a rare gas target, respectively. The excited species ($AB^{+*}$) are produced from their corresponding precursor ions ($AB^+$) by collision with a rare gas target. The fragment ions ($A^+$ or $B^+$) are formed from the dissociation of the excited ions ($AB^{+*}$). The CID efficiency, which is given by the equation (2-1), is defined as the total fragment ion current ($F_{out}$) divided by the ion current of the precursor ion ($P_{in}$) entering the collision region [1]. The CID efficiency is the product of two other parameters, the fragmentation efficiency (*FE*) and the collection efficiency (*CE*). The *FE*, which is given by the equation (2-2), is defined as the total fragment ion current divided by the total ion current (fragment ions and precursor ions ($P_{out}$)) exiting from the collision region. The *CE*, which is given by the equation (2-3), is the total ion current out of the collision region divided by the precursor ion current into the collision region. The precursor ion attenuation, which is given by equation (2-4), is defined as the ion current (subtract $P_{out}$ from $P_{in}$) divided by the precursor ion current ($P_{in}$). The attenuation of precursor ion is caused by the

collision with target gas since the collision with target gas leads to the fragmentation, scattering, and neutralization of the precursor ions. Thus precursor ion attenuation increases with increasing gas pressure.

$$CID\ \ efficiency = FE \times CE = \frac{F_{out}}{P_{in}} \tag{2-1}$$

$$FE = \frac{F_{out}}{P_{out} + F_{out}} \tag{2-2}$$

$$CE = \frac{P_{out} + F_{out}}{P_{in}} \tag{2-3}$$

$$precursor\ ion\ attenuation = \frac{P_{in} - P_{out}}{P_{in}} \tag{2-4}$$

High-energy CID efficiency of the methane ions with He gas target was measured by Gllsh and co-worker [3]. According to the measured result, the *CE* decreases almost linearly with increasing precursor ion attenuation due to scattering and neutralization. The *FE* increases, linearly with increasing precursor ion attenuation at first due to increasing probability of interaction of an ion with the target gas. In higher precursor ion attenuation, the *FE* increases more rapidly because of multiple collisions. As a result, the maximum CID efficiency occurs as a plateau in the range of 70 - 80% attenuation and is about 7.5%. The reported high-energy CID efficiency is normally about 5 - 10% [2, 3]. Therefore, it can be concluded that CID efficiency dose not increase just by increasing the pressure of target gas.

## 2.2 Method for improving dissociation efficiency

Above discussion led us to the conclusion that the *FE* needs to increase under the condition where *CE* dose not decrease, in order to enhance the CID efficiency. In order to achieve this, the ratio of $F_{out}$ to $P_{out}$ is essential to be increase. In the case of the collision between precursor ions and target gas, $F_{out}$ is given by the equation (2-5)

$$F_{out} = P_{in}[1 - \exp(-\sigma \times D \times L)] \tag{2-5}$$

where $\sigma$, $D$, and $L$ indicate cross section, density of target, and length of collision cell, respectively. In order to increase $F_{out}$, $\sigma$ needs to be increased. The cross section ($\sigma_{CA}$) of the collisional activation on collision with rare gas has been estimated to be in order of $10^{-16}$ $cm^2$ [4]. This value is comparable in the cross section ($\sim 10^{-16}$ $cm^2$) of the scattering. This comparable value is attributed to the low efficiency of high-energy CID.

Therefore, target gas, which has small cross section of the scattering and large cross section of the excitation, is necessary to be adopted in order to improve the dissociation efficiency.

According to the report [4-6], when alkali metal gas is used as target gas, high-energy collision leads to electron transfer from alkali metal atom to precursor ion and the formation of excited neutral species. Then these excited neutrals are spontaneously fragmented by excess internal energy. The neutral fragments (A + B) obtained from the dissociation of the excited neutrals ($AB^*$) were mass-analyzed and detected as the negative ions ($A^-$ + $B^-$) which are formed by another electron capture from alkali metal target, as shown in the following reaction scheme (2-1),

**Scheme (2-1)**

$$AB^+ + T \rightarrow AB^* + T^+,$$

$$AB^* \rightarrow A + B,$$

$$A \text{ (or } B) + T \rightarrow A^- \text{ (or } B^-),$$

where $AB^+$ and T indicate a precursor ion and an alkali metal target, respectively. This reaction, which is known as charge inversion mass spectrometry [4-6], is often used for the investigation of dissociation of the neutral species. The neutral fragment yield ($F_{out(neutral)}$) of charge inversion involving electron transfer in a single collision is described by the equation (2-6):

$$F_{out(neutral)} = P_{in} \times \sigma_{ET1} \times D \times L \tag{2-6}$$

Similarly, the negative ion yield ($F_{out(negative)}$) of charge inversion reactions involving successive single-electron transfers on two collisions is described by the equation (2-7):

$$F_{out(negative)} = \frac{P_{in} \times \sigma_{ET1} \times \sigma_{ET2} \times D^2 \times L^2}{2} \tag{2-7}$$

where $\sigma_{ET1}$ and $\sigma_{ET2}$ are single-electron transfer cross sections of the first and second collisions, respectively. Equations (2-6) and (2-7) do not apply under high target density conditions, because scattering of both the projectile and the secondary particle may affect the collection efficiency of the secondary particle. The value of $\sigma_{ET1}$ is reported to be in order of $10^{-14}$ $cm^2$ [4]. This value is much larger than the cross section of the collisional activation ($10^{-16}$ $cm^2$) and scattering ($10^{-16}$ $cm^2$) [4]. If the excitation induced by electron transfer is applied to MALDI-TOF/TOF, the drawback of dissociation efficiency of MALDI-TOF/TOF can be solved. However, in charge inversion mass spectrometry, the cross section of $\sigma_{ET2}$ is in the order of $10^{-16}$ $cm^2$ [4]. As a result, this

overall reaction efficiency is lower than high-energy CID efficiency. The dissociation method using electron transfer under single collision conditions, which results in fragment ions, is essential in order to achieve high dissociation efficiency. Consequently, I proposed new dissociation method using the electron transfer reaction under the single collision conditions, as shown in the following reaction scheme (2-3).

**Scheme (2-3)**

$$AB^{2+} + T \rightarrow AB^{+*} + T^{+},$$

$$AB^{+*} \rightarrow A^{+} + B \text{ (or } A + B^{+}).$$

In this method, multiply protonated peptides are used as precursor ions since neutral species, which are re-ionized to be detected, are formed by electron transfer in the case of singly protonated peptides. For example, the case of doubly protonated peptides for precursor ions is shown in scheme (2-3). The excited charge reduced species ($AB^{+*}$) are expected to be produced from their corresponding doubly protonated ions ($AB^{2+}$) by electron transfer from the alkali metal target. The fragment ions ($A^{+}$ or $B^{+}$) may be obtained from the dissociation of the excited ions ($AB^{+*}$). Fragment ions can be detected efficiently in this reaction since inefficient negative ionization of neutral species is not needed.

## 2.3 Dissociation induced by electron capture and transfer

Dissociation of multiple protonated peptides induced by electron capture has already been reported. McLafferty and co-workers developed electron capture dissociation (ECD) [7-10]. In ECD experiments, slow electrons (≈6 eV) are introduced along magnetic field lines of a fourier transform ion cyclotron resonance mass spectrometer (FT-ICR MS) and captured by trapped multiply protonated peptides. One of the reported dissociation mechanisms [11-19] of ECD is shown in Fig. 2.1

It is presume that electron capture in a charged group of the protonated peptide, followed by hydrogen transfer to a proximate amide carbonyl forming an aminoketyl intermediate. The latter undergoes a $\beta$-fission, breaking the N-C$\alpha$ bond and forming incipient fragments denoted as a *c*-type ion and a *z*-type ion. Capture of a thermal electron by a protonated peptide induces cleavage of the peptide backbone at N-C$\alpha$ bonds to yield complementary N-terminal *c*-type and C-terminal *z*-type fragment ions. ECD is believed to be non-ergodic [7], i.e., the cleavage happens prior to any intramolecular energy redistribution. This characteristic of ECD is useful in the

structural analysis of multiply protonated peptides with PTMs since the modification groups are preserved in the case of ECD, as shown in Fig. 2.2. Therefore ECD is useful tool for determining the type and site of PTMs as well as amino acid sequence.

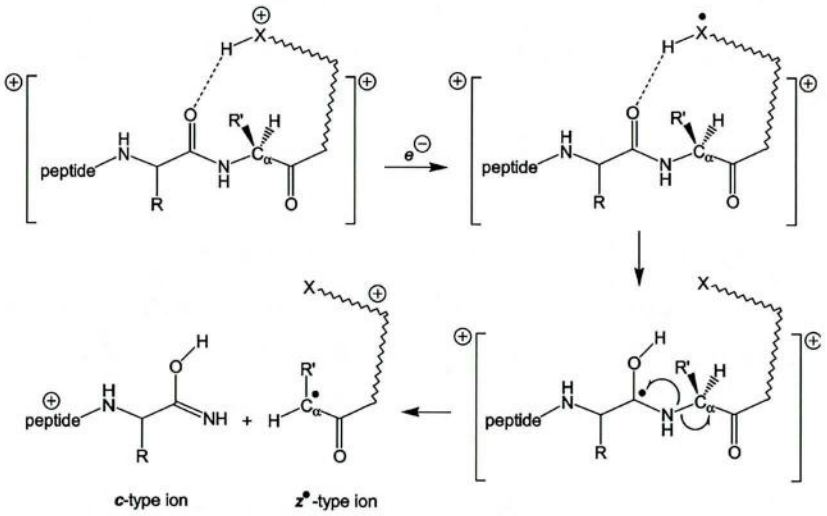


**Fig. 2.1.** Dissociation mechanism of ECD.

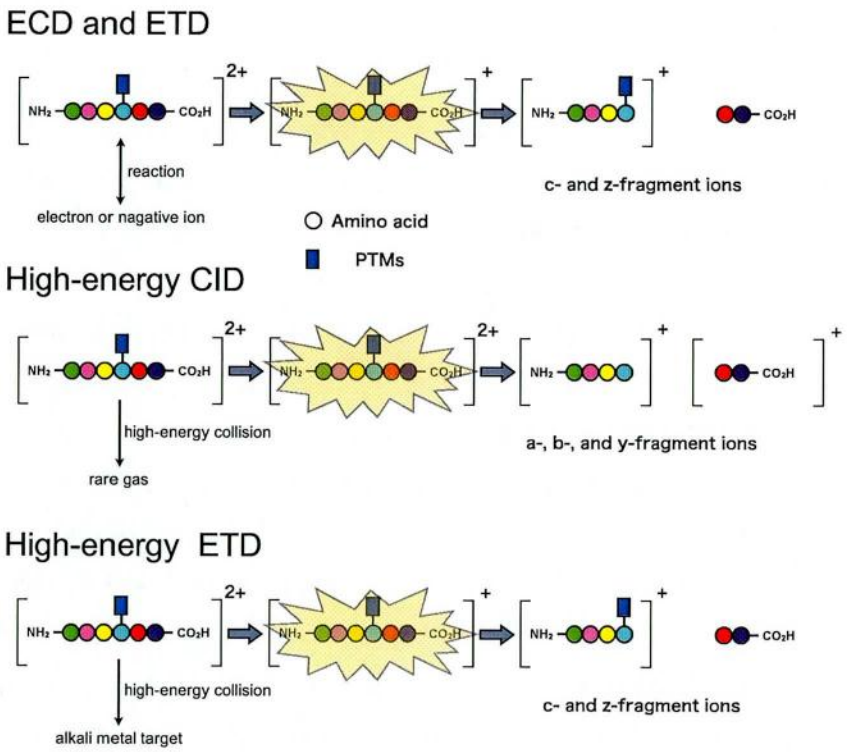


**Fig. 2.2.** Dissociation of protonated peptides with PTMs by various dissociation methods.

As a similar fragmentation technique, electron transfer dissociation (ETD) was recently proposed [20-22] by Hunt and co-workers. In ETD experiments, multiply protonated peptides react with singly charged anions in a linear ion trap. The singly charged anion transfer an electron to the multiply protonated peptide and induces fragmentation of the peptide backbone along pathways that are similar to those observed in ECD. Both ECD and ETD are widely used in determining the type and site of PTMs and the amino acid sequence of peptides with PTMs [7-10, 20-22].

## 2.4 Principle and advantage of high-energy ETD

The dissociation method using alkali metal targets, which is proposed in this research, is based on ETD. However, there is clearly difference between ETD and this dissociation method. The dissociation processes of our methods took place in the high-energy collision, unlike ETD. The dissociation process of multiple protonated peptides is discussed. When multiply protonated peptides are accelerated at several kV and collided with the alkali metal target, excited charge-reduced species are expected to be formed by electron transfer form alkali metal targets, and then fragmented, as shown in scheme (2-3). This new dissociation method is termed "high-energy electron transfer dissociation (ETD)" to distinguish ETD.

It is expected that there are some advantage of high-energy ETD over high-energy CID. (1) While fragment ions are formed from the collisional activation in the case of high-energy CID, fragment ions results from the electron transfer in the case of high-energy ETD. The cross section of the electron transfer on collision with the alkali metal target is a hundred times higher than that of collisional activation on collision with rare gas. Therefore it is expected that high-energy ETD efficiency is much higher than high-energy CID efficiency. (2) In case of high-energy CID of peptides with PTMs, many types of modification groups are considered to be easily lost during the collisional process because the bonds between peptides and modification groups are relatively weak bond in the molecules, as shown in Fig. 2.2. Therefore it is often difficult to determine the modification site in high-energy CID. Both ECD and ETD are dissociation methods using electron capture of protonated peptides, and high-energy ETD is also the dissociation method using electron transfer from the alkali metal target to protonated peptides. Therefore it is expected that *c*- and *z*-type fragment ions with no loss of PTMs are formed in the high-energy ETD of peptides. As a result,

high-energy ETD also is expected to have the potential to determine the modification site and amino acid sequence of peptides with PTMs. In this thesis, dissociation efficiency of high-energy ETD will be evaluate and demonstrate the usefulness in the structural analysis of high-energy ETD.

In the next chapter, development of a tandem mass spectrometer for performing high-energy ETD is described.

## References


[1] R.A. Yost, C.G. Enke, D.C. McGilvery, D. Smith, J.D. Morrison, Int. J. Mass Spectrom. Ion Phys. 30 (1979) 127.

[2] F.W. McLafferty, P.J. Todd, D.C. McGilvery, M.A. Baldwin, J. Am. Chem. Soc. 102 (1980) 3360.

[3] G.L. Glish, P.J. Todd, Anal. Chem. 54 (1982) 842.

[4] S. Hayakawa, J. Mass Spectrom. 39 (2004) 111.

[5] S. Hayakawa, K. Harada, K. Arakawa, N. Morishita, J. Chem. Phys. 112 (2000) 8432.

[6] S. Hayakawa, K. Harada, N. Watanabe, K. Arakawa, N. Morishita, Int. J. Mass Spectrom. 202 (2000) A1.

[7] R.A. Zubarev, N.L. Kelleher, F.W. McLafferty, J. Am. Chem. Soc. 120 (1998) 3265.

[8] R.A. Zubarev, N.A. Kruger, E.K. Fridriksson, M.A. Lewis, D.M. Horn, B.K. Carpenter, F.W. McLafferty, J. Am. Chem. Soc. 121 (1999) 2857.

[9] R.A. Zubarev, D.M. Horn, E.K. Fridriksson, N.L. Kelleher, N.A. Kruger, M.A. Lewis, B.K. Carpenter, F.W. McLafferty, Anal. Chem. 72 (2000) 563.

[10] R.A. Zubarev, Mass Spectrom. Rev. 22 (2003) 57.

[11] F. Turecek, J. Am. Chem. Soc. 125 (2003) 5954.

[12] F. Turecek, E.A. Syrstad, J. Am. Chem. Soc. 125 (2003) 3353.

[13] E.A. Syrstad, F. Turecek, J. Am. Soc. Mass Spectrom. 16 (2005) 208.

[14] X. Chen, F. Turecek, J. Am. Chem. Soc. 128 (2006) 12520.

[15] N. Leymarie, E.A. Berg, M.E. McComb, P.B. O'Connor, J. Grogan, F.G. Oppenheim, C.E. Costello, Anal. Chem. 74 (2002) 4124.

[16] N. Leymarie, C.E. Costello, P.B. O'Connor, J. Am. Chem. Soc. 125 (2003) 8949.

[17] C. Lin, J.J. Cournoyer, P.B. O'Connor, J. Am. Soc. Mass Spectrom. 17 (2006) 1605.

[18] M.A. Belyayev, J.J. Cournoyer, C. Lin, P.B. O'Connor, J. Am. Soc. Mass Spectrom. 17 (2006) 1428.

[19] P.B. O'Connor, C. Lin, J.J. Cournoyer, J.L. Pittman, M. Belyayev, B.A. Budnik. J. Am. Soc. Mass Spectrom. 17 (2006) 576.

[20] J.E.P. Syka, J.J. Coon, M.J. Schroeder, J. Shabanowitz, D.F. Hunt, Proc. Natl. Acad. Sci. U. S. A. 101 (2004) 9528.

[21] J.J. Coon, J.E.P. Syka, J.C. Schwartz, J. Shabanowitz, D.F. Hunt, Int. J. Mass Spectrom. 236 (2004) 33.

[22] P.A. Chrisman, S.J. Pitteri, J.M. Hogan, S.A. McLuckey, J. Am. Soc. Mass Spectrom. 16 (2005) 1020.

# Chapter 3

## Development of a tandem magnetic sector mass spectrometer for probing high-energy ETD

### 3.1 Introduction

In this chapter, development of a tandem mass spectrometer for probing high-energy ETD is described. In order to investigate the dissociation efficiency of high-energy ETD and, demonstrate the usefulness in structural analysis of high-energy ETD, a tandem TOF mass spectrometer for performing high-energy ETD experiments needs to be newly developed. In the high-energy ETD experiments, multiply protonated peptides are accelerated at several kV and collided with alkali metal target. Therefore, multiply protonated peptides are necessary to be generated. However, singly protonated peptides are usually generated by MALDI. Hence ESI ion source is necessary for a TOF/TOF instrument to generate a multiple protonated molecule. Unfortunately, however, tandem TOF mass spectrometers with ESI ion source "ESI-TOF/TOF" have never been achieved. A number of reasons can be given for this lack of ESI-TOF/TOF. One of the main reasons is the fact that the mass resolution in fragment ions analysis of general TOF/TOF is insufficient to analyze multiply charged fragment ions. In ESI [1-3], the isotopomers are not spaced at 1 u distance as in singly charged MALDI spectrum [4-8], but spaces at fractional u, depending on the charge state of the analyte ions. Therefore the high mass resolution in fragment ions is required to determine the charge state and *m/z* of fragment ions. Although there are other reasons that ESI-TOF/TOF has never been developed, the reason is explained in detail in chapter 5.

High-energy collision can be also performed by tandem magnetic sector mass spectrometers. In this case, the tandem magnetic sector mass spectrometers with ESI ion source has been already commercialized. Consequently, a tandem sector mass spectrometer for performing high-energy ETD experiments was newly developed as a prototype instrument for the investigation of dissociation efficiency of high-energy ETD [9-12]. In addition, introduction of alkali metal target into the collision cell is required for high-energy ETD experiments. The technique for introduction of alkali metal targets gas into collision cell of tandem magnetic sector mass spectrometers has been already

established in Hayakawa laboratory of Department of Chemistry in Osaka Prefecture University [13-15]. The introduction technique of alkali metal targets is applied to the tandem sector mass spectrometer for high-energy ETD. We will demonstrate the usefulness (high dissociation efficiency and high sequence coverage) of high-energy ETD by using this tandem sector mass spectrometer in chapter 4. The details of the instrument will be described in this chapter.

## 3.2 Instrumentation

### 3.2.1 Overview of a sector type tandem mass spectrometer

A schematic view and photograph of the tandem sector mass spectrometer are shown in Fig. 3.1 and Fig. 3.2, respectively. This instrument has been developed jointly by Awazu laboratory of Division of Sustainable Energy and Environmental Engineering at Osaka University, Mass Spectrometry laboratory of Department of Physics at Osaka University, and Hayakawa lab, which is placed at Mass Spectrometry lab. This system consists of a double-focusing mass spectrometer (JMS-HX110, JEOL, Akishima, Japan), a collision cell for rare gas or alkali metal gas, a spherical electric sector (M80-B, Hitachi, Chiyoda, Japan), and a detector.

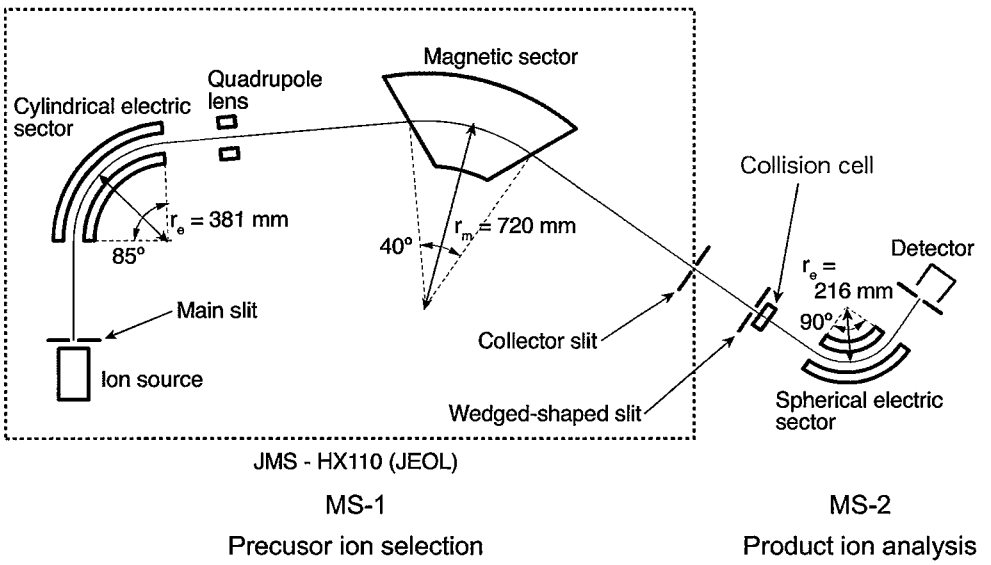


**Fig. 3.1.** Schematic view of the tandem sector mass spectrometer for probing high-energy ETD. Singly (or doubly) charged precursor ions are mass selected by MS-1. Rare gas targets (or alkali metal targets) are introduced into the collision cell. CID spectra of precursor ions are mass analyzed by using MS-2.

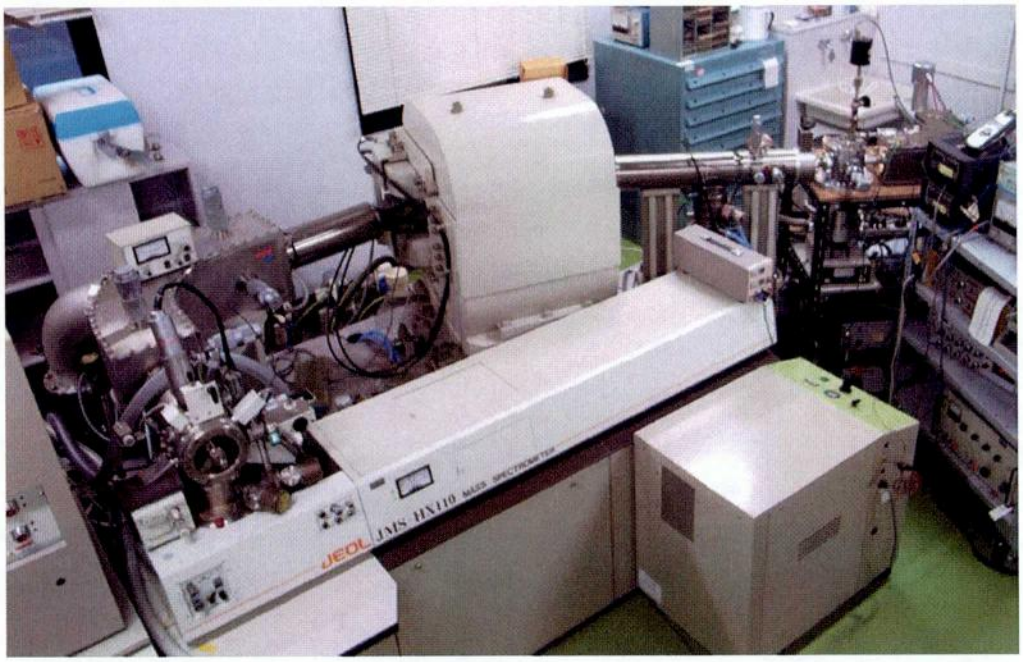


**Fig. 3.2.** Photograph of the tandem sector mass spectrometer for probing high-energy ETD.

### 3.2.2 Measurement of product ion spectra

In this instrument, various ionization methods such as EI, FAB, and ESI can be used for ionization of atoms and molecules. The analyte ions are accelerated by an accelerating voltage up to 10 kV. A JMS-HX110 double-focusing mass spectrometer is used for high-resolution precursor ion selection as MS-1. The central radius of the electric sector is 381 mm, and the magnetic field had a central radius of 720 mm. The resolution of precursor ion selection is set to 1,000, which was accomplished by adjusting the main (1000 unit) and collector slits (140 μm wide) of MS-1. The mass-selected precursor ions enter a 3.7 cm long collision cell located at the exit of MS-1. The distance between the exit of MS-1 and the entrance of the collision cell is 365 mm. Fragment ions are formed by the collision with the target gas. The fragment ions possess the same velocity as the precursor ion but a wide range of kinetic energies. The kinetic energy of a fragment ion can be expressed as equation (3-1),

$$E_f = E_p \frac{m_f}{M_p} \tag{3-1}$$

where $E_f$ is the kinetic energy of the fragment, $m_f$ is the mass of the fragment ion, $M_p$ is the mass of the precursor ion, and $E_p$ is the kinetic energy of the precursor in the

laboratory frame. The kinetic energy analysis of fragment ions provides the mass of fragment ions. The kinetic energy is measured by a spherical electrostatic analyzer (ESA) with central radius of 216 mm (MS-2), of the same type as that found in the M80-B instrument. The mass-analyzed ions are detected by a 9 kV post-acceleration secondary-electron multiplier. The mass resolution of MS-2 is less than 100.

### 3.2.3 Alkali metal gas transfer system

Schematic view and photograph of alkali metal gas transfer system is shown in Fig. 3.3. and Fig. 3.4 respectively. Alkali metal gas transfer system consists of a reservoir, a ball valve, a pass, and a collision cell. They are made of the copper from the point of view of heat transfer except for the ball valve. The ball valve is made of the brass. The collision cell is mounted in a vacuum chamber consisting of a perpendicular cylinder with an inner diameter of 112 mm and a height of 118 mm. The square flange and circular flange are made of the athermic stainless. A wedge-shaped slit 300 μm width and 4.3 mm high in front of the collision cell confines the ions that entered the collision cell. The entrance hole of the collision cell is 1 mm wide and 8 mm high and the exit hole is 2 mm wide and 10 mm high. The position of the collision cell, which can be moved in a direction perpendicular to the ion beam by using the pusher, is adjusted so that the incident ions do not collide with either the entrance hole or the exit hole.

The alkali metal target is introduced into the collision cell as a vapor from a reservoir through a ball valve. The alkali metal targets existed in the thermal equilibrium in the collision cell. Both the vacuum chamber and MS-2 are differentially evacuated by turbo molecular pumps (STP-300H/SEIKO SEIKI and TMH260/Balzers). The pressures measured by ionization vacuum gauges (GI-TL2RY/ULVAC) mounted on both the vacuum chamber and on MS-2 are less than $6 \times 10^{-5}$ Pa when the target gas is not supplied. The temperatures of the collision cell, the ball valve, and the reservoir are adjusted to control the density of alkali metal in the collision cell. The temperature of the collision cell (170℃) is set to be higher than those of both the ball valve (130℃) and the reservoir (115℃) so that the alkali metal vapor do not deposit in the collision cell. When the supply of alkali metal vapor from the reservoir is stopped by closing the ball valve, the pressure of the alkali metal vapor in the collision cell decreases toone-hundredth of its original value in 1 s.

By changing the collision cell, the rare gas target can be introduced in a collision cell of the same size as the alkali metal target. The density of the rare gas target is controlled by means of a variable-leak valve (Whitey SS-22RS2). The target pressure is directly measured by means of a capacitance manometer (MKS Baratron 127AA-00001B) attached by a pipe with a 26 mm inner diameter and a gas conductance of 11 $dm^3 \cdot s^{-1}$.

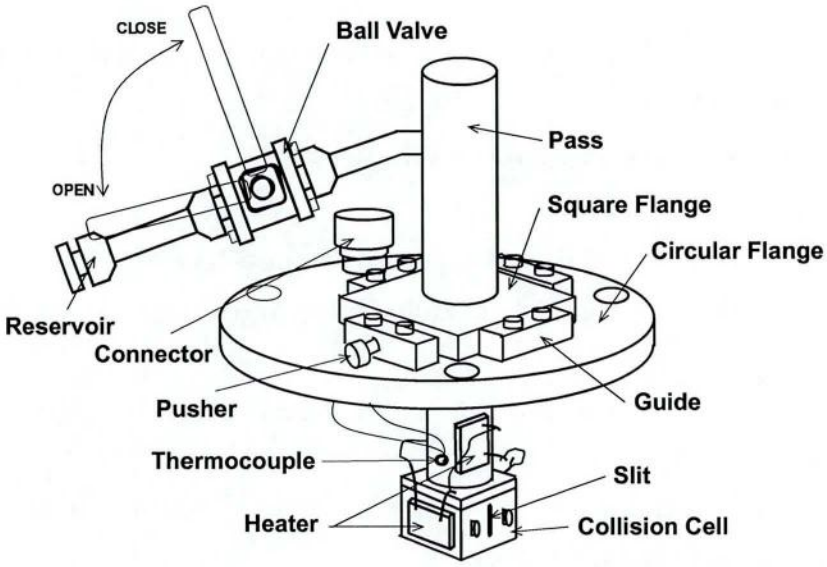


**Fig. 3.3.** Schematic view of alkali metal gas transfer system.

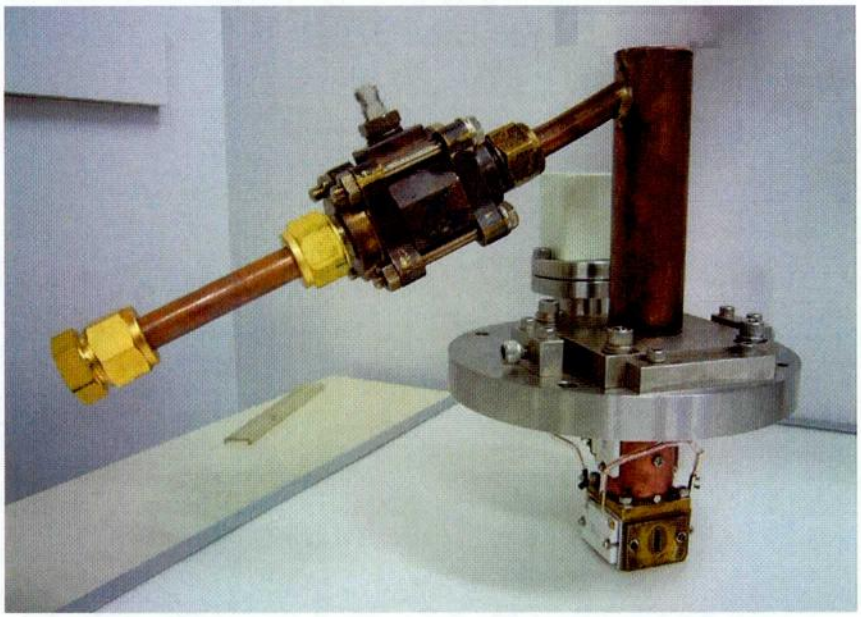

**Fig. 3.4.** Photograph of alkali metal gas transfer system.

## Reference


[1] J.B. Fenn, M. Mann, C.K. Meng, S.F. Wong, C.M. Whitehouse, Science 246 (1989) 64.

[2] J.B. Fenn, M. Mann, C.K. Meng, S.F. Wong, C.M. Whitehouse, Mass Spectrom. Rev. 9 (1990) 37.

[3] R.D. Smith, J.A. Loo, C.G. Edmonds, C.J. Barinaga, H.R. Udseth, Anal. Chem. 62 (1990) 882.

[4] M. Karas, D. Bachmann, U. Bahr, F. Hillenkamp, Int. J. Mass Spectrom. Ion Process. 78 (1987) 53.

[5] M. Karas, F. Hillenkamp, Anal. Chem. 60 (1988) 2299.

[6] M. Karas, J. Mass Spectrom. 32 (1997) 1.

[7] M. Karas, D. Bachmann, F. Hillenkamp, Anal. Chem. 57 (1985) 2935.

[8] M. Karas, U. Bahr, A. Ingendoh, F. Hillenkamp, Angewandte Chemie 101 (1989) 805.

[9] S. Hayakawa, A. Kitaguchi, S. Kameoka, M. Toyoda, T. Ichihara, J. Chem. Phys. 124 (2006) 224320.

[10] S. Hayakawa, K. Minami, K. Iwamoto, M. Toyoda, T. Ichihara, H. Nagao, Int. J. Mass Spectrom. 266 (2007) 122.

[11] S. Hayakawa, M. Hashimoto, H. Nagao, K. Awazu, M. Toyoda, T. Ichihara, Y. Shigeri, Rapid Commun. Mass Spectrom. 22 (2008) 567.

[12] H. Nagao, S. Hayakawa, M. Hashimoto, K. Iwamoto, M. Toyoda, Y. Shigeri, M. Jitosho, K. Awazu, J. Mass Spectrom. Soc. Jpn. 57 (2009) 123.

[13] S. Hayakawa, J. Mass Spectrom. 39 (2004) 111.

[14] S. Hayakawa, K. Harada, K. Arakawa, N. Morishita, J. Chem. Phys. 112 (2000) 8432.

[15] S. Hayakawa, K. Harada, N. Watanabe, K. Arakawa, N. Morishita, Int. J. Mass Spectrom. 202 (2000) A1.

# Chapter 4

## Investigation of dissociation induced by collision with rare gas and alkali metal targets

### 4.1 Introduction

In this chapter, the investigation of dissociation induced by collision with rare gas and alkali metal targets are described. It is important to understand the difference of dissociation behavior between rare gas targets and alkali metal targets, in advance, in order to ensure the success of high-energy ETD experiments. For this reason, dissociation induced by collision with rare gas targets and alkali metal targets are investigated. The dissociation of inorganic samples such as silver bromide and tungsten hexacarbonyl, which are simpler species than biological samples, are investigated in the beginning since the analysis of biological samples is difficult to interpret. In the section 4.2, unimolecular dissociation and high-energy CID of $Ag_xBr^+$ ($x$ = 2, 4, 6, 8, 10) clusters are investigated by using the rare gas target [1]. In the section 4.3, dissociation channels of silver bromide cluster $Ag_2Br$, silver cluster $Ag_3$ and their ions by using the alkali metal target are studied [2]. In the section 4.4, high-energy ETD of doubly charged tungsten hexacarbonyl $W(CO)_6^{2+}$ ions using alkali metal targets is investigated [3]. It is expected that fundamental data obtained by these investigation is useful in the high-energy ETD experiments of biomolecular ions. After these investigations, high-energy ETD spectra of polypeptides (Section 4.5) [4] and phosphopeptides (Section 4.6) [5] are obtained in order to investigate the dissociation efficiency of high-energy ETD, and to demonstrate the usefulness in the structural analysis of high-energy ETD.

## References

[1] H. Nagao, M. Toyoda, S. Hayakawa, K. Iwamoto, T. Ichihara, K. Kawamura, K. Awazu, Eur. J. Mass Spectrom. 15 (2009) 459.

[2] H. Nagao, K. Awazu, S. Hayakawa, K. Iwamoto, M. Toyoda, T. Ichihara, Eur. Phys. J. D 45 (2007) 279.

[3] S. Hayakawa, K. Minami, K. Iwamoto, M. Toyoda, T. Ichihara, H. Nagao, Int. J. Mass Spectrom. 266 (2007) 122.

[4] H. Nagao, S. Hayakawa, M. Hashimoto, K. Iwamoto, M. Toyoda, Y. Shigeri, M. Jitosho, K. Awazu, J. Mass Spectrom. Soc. Jpn. 57 (2009) 123.

[5] S. Hayakawa, M. Hashimoto, H. Nagao, K. Awazu, M. Toyoda, T. Ichihara, Y. Shigeri, Rapid Commun. Mass Spectrom. 22 (2008) 567.

## 4.2 Unimolecular and high-energy collision induced dissociation (CID) of singly-charged mono-bromide silver clusters $Ag_xBr^+$ ($x$ = 2, 4, 6, 8, 10) using the rare gas target

### 4.2.1 Introduction

In this section, dissociation of singly charged silver bromide clusters induced by collision with the rare gas target is described.

Halogenated coinage metals have attracted much interest recently, from both experimental and theoretical standpoints. Halogenated coinage metals are of interest not only for the practical applications such as the use of copper (II) halides as catalysts [1] and of $CuCl_2$ as possible as a chemical laser [2], but also due to a new interest in gold halides, some of which appear to have unique structures [3]. Among the halogenated coinage metals, silver bromide and chloride have been extensively studied at the bulk level due to their implications in the photographic process. They are commonly used as photographic materials. The photochemistry of silver bromide and chloride has been investigated for several years in order to understand the fundamental processes on photographic films, plates or papers [4,5]. Several mechanisms of the photographic process have been proposed by Mott and Gurney [6], Mitchell [7] and Hamilton [8].

Recently, the photophysics of silver bromide clusters [9] was examined by gas-phase spectroscopic techniques to obtain information on the unique properties of the compounds at the microscopic level. Metastable fragmentation channels for anionic and cationic silver bromide clusters were examined by L'Hermite et al [10,11]. and were compared with the results obtained by *ab initio* Density Functional Theory (DFT) [12,13]. Dissociation channels of small silver bromide clusters, $Ag_2Br$ and the $Ag_2Br^+$ ions were investigated by high-energy CID and charge inversion mass spectrometry using an alkali metal target [14]. Experimental studies were also performed to investigate the relative stability, possible structural formulas, unimolecular dissociation, and CID of mono-iodide silver clusters [15]. Recently, a number of theoretical studies were also performed to investigate the geometric structures and stabilities of silver halide clusters [12,13,16-18]. Molecular-ion reactions between mass selected silver or silver hydride cluster cations and organic molecules with synthesized silver halide clusters have been examined using multistage mass spectrometry ($MS^n$) [19-21].

The CID of mixed clusters has been investigated because CID of cluster ions is a well-established mass spectrometric tool for the study of the dissociation of size-selected cluster ions. There are two types of CID, a low-energy CID and a high-energy CID. Low-energy CID spectra were obtained at energies of tens of eV (laboratory frame) or less, whereas high-energy CID spectra were obtained at energies on the order of several keV (laboratory frame). Observation of a CID spectrum is made possible through collision of a mass-selected precursor ion with a target neutral species when the energy in the center-of-mass system becomes available for conversion from translational (or kinetic) energy to internal energy in the precursor ion.

The energy distribution of the excited ions activated by low-energy multiple collisions is very narrow and centers closely around the lowest dissociation energy limit [22-26]. The low internal energy available in the low-energy CID yields the fragment ions formed by cleavage of the relatively weak bond in the molecules. Likewise, the mechanism of unimolecular dissociation is well understood.

In contrast, high-energy CID has a maximum distribution at the low energy limit and shows a long tail extending to the higher energy beyond several electron volts. The broad and higher internal potential energy of excited ions examined in the high-energy CID allows many dissociation channels [22-26]. In general, high-energy activation can lead to different fragmentation pathways compared with low-energy activation.

Herein, I focus on the stabilities, structural formulas and dissociation channels of the mono-bromide silver clusters $Ag_xBr^+$. The mono-bromide silver clusters are of interest because by employing these clusters in type $Ag_xBr_y^+$ ($x \geq y$), the simplest system may facilitate further understanding of the influence of a bromine atom within the system. The relative intensities of generated $Ag_xBr^+$ ($x$ = 1 - 24) and the unimolecular dissociation and high-energy CID spectra of $Ag_xBr^+$ ($x$ = 2, 4, 6, 8, 10) were measured in order to investigate their stabilities, structural formulas and dissociation channels. Although several studies on low-energy dissociation pathways of silver bromide clusters have been conducted [10,11], there have been almost no investigations of high-energy dissociation pathways of silver bromide clusters. It is clear that unimolecular dissociation and high-energy CID methods are highly complementary, and utilizing these dissociation methods is structurally more informative. The unimolecular dissociation and high-energy CID provide information about the weakest bond in the mono-bromide silver clusters as well as what types of ion products are typically

generated. The difference in the dissociation channels between the unimolecular dissociation and CID was explained in terms of the internal energy distribution in the excited $Ag_xBr^{+*}$ cluster. The experimental results obtained in the current work were compared with the calculated thermochemical data and the spherical jellium model (SJM) [27,28]. SJM is known to account for the relative stabilities and structural properties observed for alkali- [29,30] and noble-metal [31-33] clusters and, to a certain extent, for other metallic clusters [34]. On the other hand, metal clusters (charged or neutral) with 2, 8, 18, 20, 34, and 40 delocalized valence electrons showed enhanced stability and thus strong peaks in the mass spectrum, whereas metal clusters possessing 3, 9, 19, 21, 35, 41, delocalized valence electrons were relatively unstable, as was confirmed by the mass spectral ion peak intensity distribution of the clusters. To our knowledge, there have been no reports in which high-energy dissociation channels of mono-bromide silver clusters were compared with both thermochemical data and SJM. These approaches provide new insight into the dissociation of mono-bromide silver clusters.

### 4.2.2 Experimental section

Only a pertinent point to the present work will be given here because the experimental setup was already described in detail in chapter 3 [35]. Bromide silver cluster ions were generated by FAB on a pressed pellet of silver bromide purchased from Wako Pure Chemical Industries, Ltd. (Osaka, Japan) [36]. The pellet was sputtered by xenon (Xe) atom bombardment, typically at 8 keV. A FAB gun was operated using Xe gas at an emission current of 20 mA. The mass spectrum of silver bromide cluster ions was measured in order to determine what types of ions were generated by FAB. In this measurement, only one part of the MS-1 was utilized.

Unimolecular dissociation and CID product ions of $Ag_xBr^+$ ($x$ = 2, 4, 6, 8, 10) were also measured in order to investigate the dissociation channels of these ions. In this work, argon (Ar) was used as the collision gas and introduced into the collision cell through a variable-leak valve. In order to achieve CID under single-collision conditions, the gas pressure was controlled in order to reduce the transmission of the precursor ions to about 70%. In the case of $Ag_xBr^+$ ($x$ = 2, 4, 6, 8, 10), the peak ratios of the product ions in the CID spectra observed using Ar gas were constant at the employed gas pressures by the transmission of 70%. The consistency of the peak ratios indicated that

the CID spectra measured at a transmission of ca. 70% did not differ from those expected based on the single-collision conditions. The CID spectra of $Ag_2Br^+$, $Ag_4Br^+$, $Ag_6Br^+$, $Ag_8Br^+$, and $Ag_{10}Br^+$ with the Ar target were measured at target pressures of 1.50 Pa, 1.37 Pa, 0.96 Pa, 0.73 Pa, and 0.72 Pa, respectively. The unimolecular dissociation spectra were obtained under the condition that the collision gas was excluded from the collision cell. The pressures in the vacuum chamber and the MS-II were measured using an ionization gauge mounted on each compartment and were less than $6 \times 10^{-5}$ Pa when the collision gas was not supplied. Hence, the collision with the background gas was considered negligible.

## 4.2.3. Results and Discussion

### 4.2.3.1 Mass spectrum of brominated silver clusters

Figure 4.2.1 shows the mass spectrum of the positively charged ions generated by FAB on the pressed silver bromide pellet. This spectrum reveals a wide range of brominated silver cluster $Ag_xBr_y^+$ ions, as well as "bare" silver cluster $Ag_x^+$ ions, where $x$ is the number of silver atoms, and $y$ is the number of bromine atoms, up to *m/z* 2500. A combination of numbers labeled above each peak refers to the combination of the number $x$ and $y$ for the cluster ion $Ag_xBr_y^+$. For example, $Ag_5Br_2^+$ is represented as 5,2. In this mass spectrum, a series of bromine-deficient cluster ions ($x > y$, in particular when $x–y$ = odd) such as $Ag_xBr_{x-1}^+$, $Ag_xBr_{x-3}^+$, and $Ag_xBr_{x-5}^+$ are dominant. On the other hand, cluster ions are rarely observed with $x$-$y$ = an even number, such as $Ag_xBr_{x-2}^+$, $Ag_xBr_{x-4}^+$, and $Ag_xBr_{x-6}^+$.

Figure 4.2.2(A) shows the correlation between the relative intensities of $Ag_x^+$ and its cluster size ($x$) obtained from the mass spectrum of Fig. 4.2.1. As observed in previous studies of noble metal cluster ions produced by sputtering [24], Fig. 4.2.2(A) shows an odd/even alternation in intensity against $x$ as along with the shell-closing effect at $x$ = 3, 9, (19), and 21 for $Ag_x^+$, which correspond to the number of delocalized valence electrons, $n$ = 2, 8, (18), and 20, respectively.

Figure 4.2.2(B) shows the correlation between the relative intensities of $Ag_xBr^+$ and the cluster size ($x$) of $Ag_xBr^+$ obtained from the mass spectrum of Fig. 4.2.1. In this work, the mono-bromide silver clusters was investigated in order to determine the influence of a bromine atom on the silver cluster. An oscillatory correlation and the shell-closing effect at $x$ = 4, 10, (20), and 22 were observed for the relative intensities of

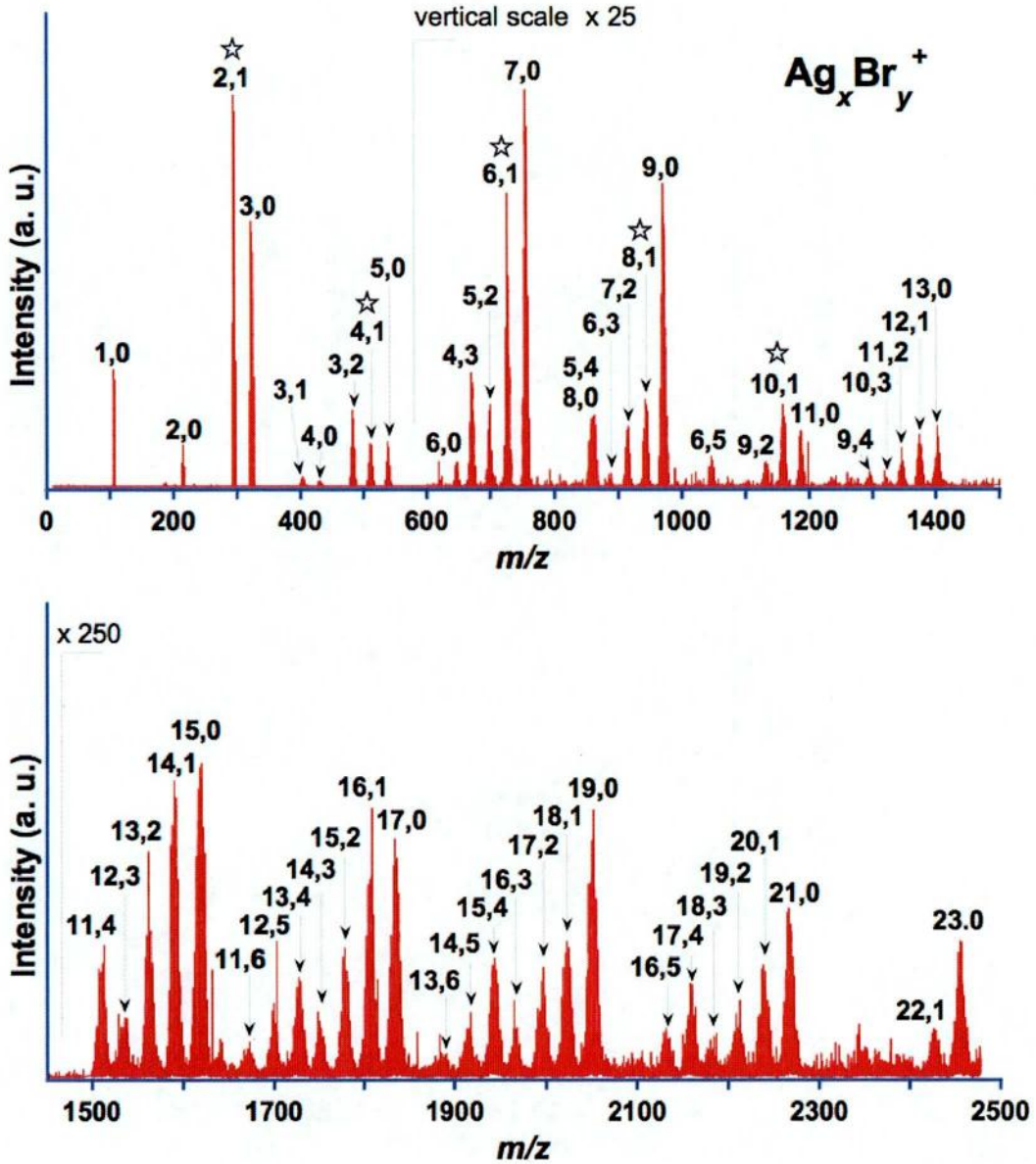


**Fig. 4.2.1.** Mass spectrum of the positively charged ions generated by FAB on the pressed silver bromide pellet. The numbers in the subscripts for *x,y* above some peaks refer to the numbers of silver (*x*) and bromine atoms (*y*) in the corresponding cluster.

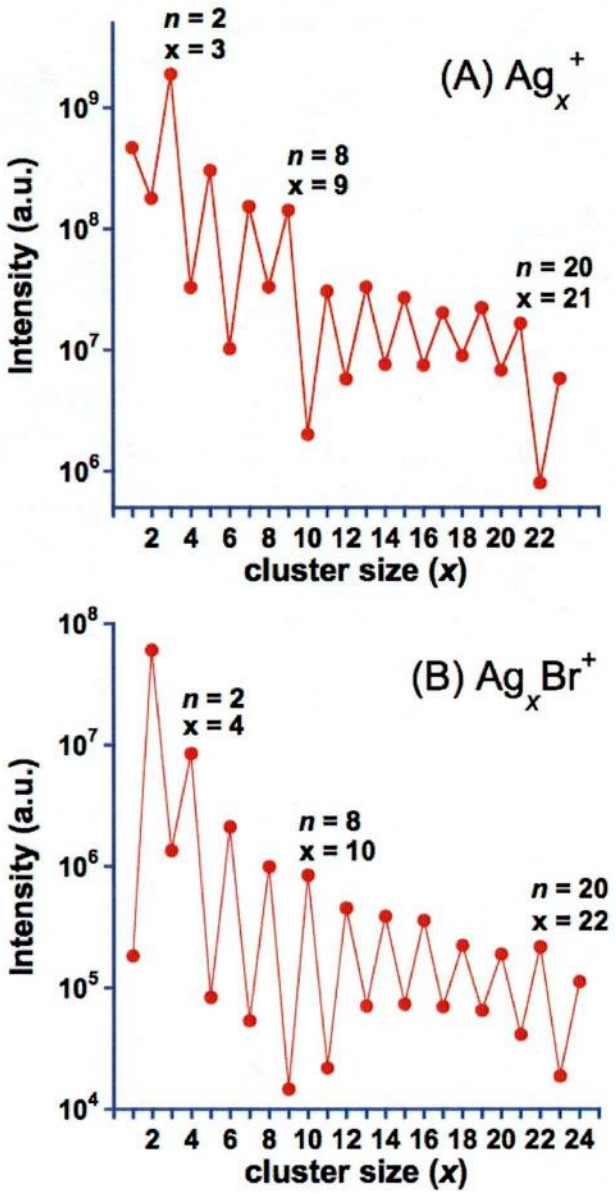


**Fig. 4.2.2.** (A) Correlation between the relative intensities of $Ag_x^+$ and its cluster size ($x$), where $x$ and $n = x - 1$ are the numbers of silver atoms and delocalized valence electrons in the cluster, respectively. (B) Correlation between the relative intensities of $Ag_xBr^+$ and the cluster size ($x$) of $Ag_xBr^+$. The number of delocalized valence electrons in the cluster is given by $n = x - 2$.

$Ag_xBr^+$ clusters. Compared with the ion intensities of $Ag_x^+$, the number of delocalized valence electrons of $Ag_xBr^+$ can be given by $n = x - 2$. The number of delocalized electrons thus obtained for $Ag_xBr^+$ suggests that addition of a bromine atom to a silver cluster ion $Ag_x^+$ gives rise to the formation of an AgBr unit, and therefore localizes a previously delocalized valence electron of $Ag_x^+$ onto the bromine atom. Namely, $Ag_xBr^+$ is thought to have a structural formula of the type $Ag_{x-1}^+(AgBr)$ and the relative stability can be determined by the intrinsic stability of the remaining metallic moiety ($Ag_{x-1}^+$) of the cluster $Ag_{x-1}^+(AgBr)$. Similar results were reported in the literature for silver iodide [37] and hydroxide [38], lithium oxide [39] and hydride [40]. C. K. Fagerquist et al. [37] determined the relative intensities of $Ag_xI^+$ clusters formed from sputtering of an isotopically enriched silver foil in the presence of $CH_3I$ vapor and proposed that the charged metal-rich iodinated silver clusters consisting of $Ag_xI^+$ have the structural formula $Ag_{x-1}^+(AgI)$. Therefore, the assumption that $Ag_xBr^+$ has the structural formula of the type $Ag_{x-1}^+(AgBr)$ in the current work is consistent with their proposal.

Although the method of generating $Ag_x^+$ and $Ag_xBr^+$ clusters as well as the cluster ions examined are different from those reported in previous works [31,37], I found that the odd/even alternation in intensity and the shell-closing effect was noticeable in the clusters generated by FAB on the pressed silver bromide pellet.

#### 4.2.3.2 Unimolecular dissociation and CID of mono-bromide silver clusters.

Unimolecular dissociation and CID spectra of $Ag_xBr^+$ clusters ($x = 2, 4, 6, 8, 10$), which are indicated with stars above the peaks in the mass spectrum (Fig. 4.2.1), were also measured to investigate the dissociation channels. In these measurements, the series $x = 2, 4, 6, 8, 10$ was selected, since the relative intensities of the series of $x \geq 12$ and $x =$ odd are too low to investigate the dissociation channels, as shown in Fig. 4.2.1.

Unimolecular dissociation spectra (A) and CID spectra (B) of $Ag_2Br^+$ (*m/z* 295), $Ag_4Br^+$ (*m/z* 511), $Ag_6Br^+$ (*m/z* 727), $Ag_8Br^+$ (*m/z* 943), and $Ag_{10}Br^+$ (*m/z* 1159) are shown in Figs. 4.2.3, 4.2.4, 4.2.5, 4.2.6, and 4.2.7, respectively. All spectra are normalized to the peak intensities of the product ions $Ag^+$, $Ag_3^+$, $Ag_5^+$, $Ag_7^+$, and $Ag_9^+$ in Figs. 4.2.3, 4.2.4, 4.2.5, 4.2.6, and 4.2.7, respectively. The actual intensities of the product ions were significantly weaker for unimolecular dissociation than for CID, where the CID spectrum was measured at a transmission of ca. 70%. Only the spectra

for $Ag_4Br^+$ (Fig. 4.2.4) and $Ag_6Br^+$ (Fig. 4.2.5) are explained in detail here, since all the unimolecular and CID spectra may be interpreted similarly.

In the unimolecular dissociation spectrum of $Ag_4Br^+$ in Fig. 4.2.4(A), the $Ag_4Br^+$ peak at *m/z* 511 that did not dissociate is by far the strongest and the intensity is significantly higher than the upper limit of the scale of the vertical axis. Such high intensity for the $Ag_4Br^+$ peak is consistently the case for a precursor ion that does not dissociate. The predominant peak at around *m/z* 323 is associated with $Ag_3^+$ formed by a loss of AgBr from $Ag_4Br^+$. The peaks assigned to $Ag_3Br^+$, $Ag_2Br^+$ and $Ag_2^+$ were observed at around *m/z* 404, 295, and 216, respectively.

In the CID spectrum of $Ag_4Br^+$ in Fig. 4.2.4(B), the peak for the undissociated precursor ion $Ag_4Br^+$ at *m/z* 511 is also by far the strongest, and exceeds the upper limit of the scale of the vertical axis. The peak located at around *m/z* 323 was the dominant peak observed, and is associated with $Ag_3^+$ accumulated from the loss of AgBr. There are also a number of minor dissociation channels, $Ag_2$ loss, $Ag_2Br$ loss, Br loss, $Ag_3Br$ loss, and $Ag_3$ loss. The peak located around *m/z* 79 associated with the $Br^+$ ion was very rarely observed.

In the unimolecular dissociation spectrum of $Ag_6Br^+$ in Fig. 4.2.5(A), the strongest peak at *m/z* 727 was attributed to the undissociated precursor ion $Ag_6Br^+$. The peak associated with $Ag_5^+$ was dominantly observed at around *m/z* 539 in Fig. 4.2.5(A). The $Ag_5^+$ ions formed from the loss of AgBr. The peaks associated with $Ag_3^+$, $Ag_4^+$, and $Ag_4Br^+$ ions were observed at around *m/z* 323, 432, and 511, respectively.

In the CID spectrum of $Ag_6Br^+$ in Fig. 4.2.5(B), the strongest peak at *m/z* 727 was attributed to the undissociated precursor ion that did not interact with the target. The peaks located at around *m/z* 539 and 511 are associated with $Ag_5^+$ and $Ag_4Br^+$ and are the dominant peaks in the CID spectrum of $Ag_6Br^+$. These product ions were thought to occur due to the loss of AgBr and $Ag_2$, respectively. Product peaks resulting from other various dissociation channels, such as Ag loss, $Ag_2Br$ loss, and $Ag_3$ loss, are weaker than those associated with AgBr and $Ag_2$ loss. Further, these may also be observed in the CID spectrum of $Ag_6Br^+$.

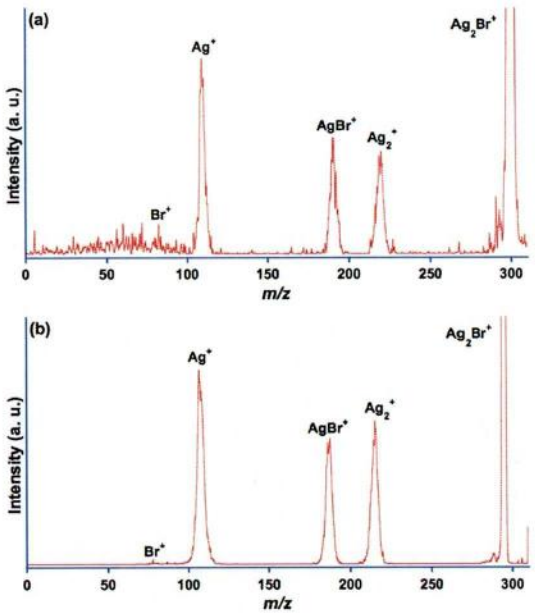


**Fig. 4.2.3.** (A) Unimolecular dissociation spectrum and (B) high-energy CID spectrum of $Ag_2Br^+$ (*m/z* 295) formed by FAB. In high-energy CID, the target gas was Ar and the collision energy was 5 keV.

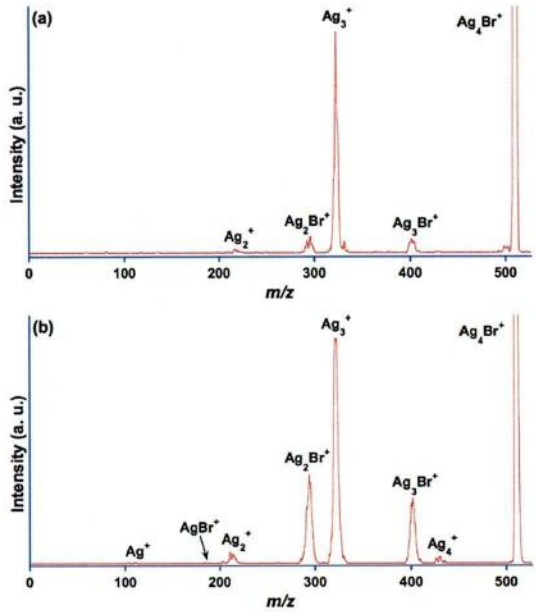


**Fig. 4.2.4.** (A) Unimolecular dissociaton spectrum and (B) high-energy CID spectrum of the $Ag_4Br^+$ (*m/z* 511) formed by FAB. In high-energy CID, the target gas was Ar and the collision energy was 5 keV.

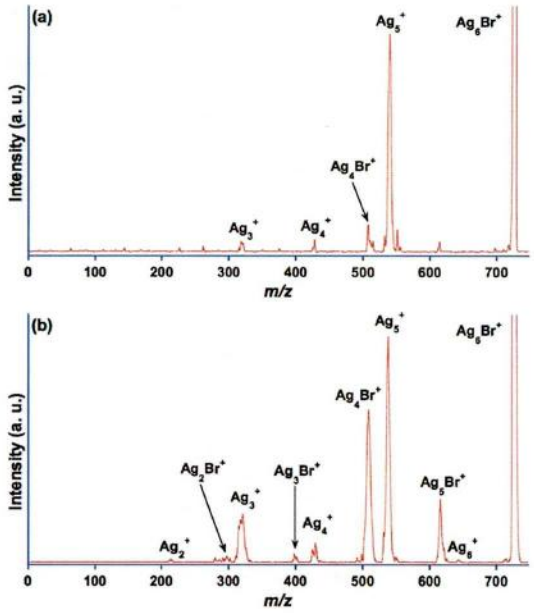


**Fig. 4.2.5.** (A) Unimolecular dissociation spectrum and (B) high-energy CID spectrum of the $Ag_6Br^+$ (*m/z* 727) formed by FAB. In high-energy CID, the target gas was Ar and the collision energy was 5 keV.

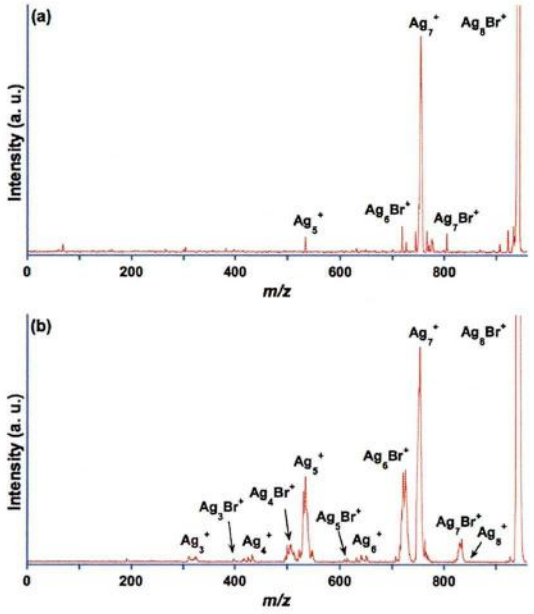


**Fig. 4.2.6.** (A) Unimolecular dissociation spectrum and (B) high-energy CID spectrum of the $Ag_8Br^+$ (*m/z* 943) formed by FAB. In high-energy CID, the target gas was Ar and the collision energy was 5 keV.

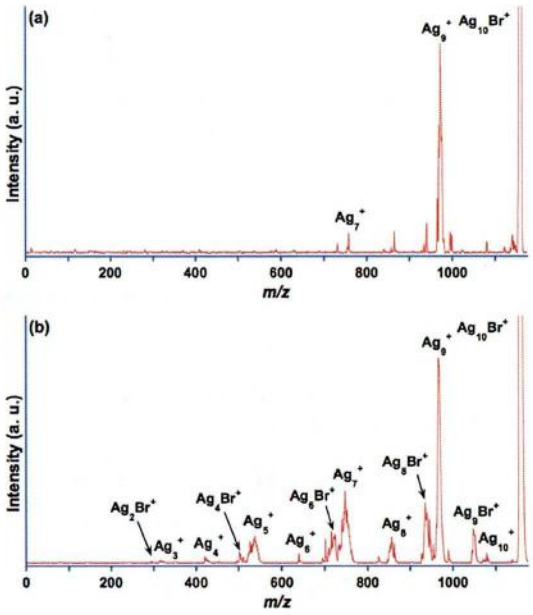


**Fig. 4.2.7.** (A) Unimolecular dissociation spectrum and (B) high-energy CID spectrum of the $Ag_{10}Br^+$ (*m/z* 1159) formed by FAB. In high-energy CID, the target gas was Ar and the collision energy was 5 keV.

As is shown in Figs. 4.2.3, 4.2.4, 4.2.5, 4.2.6, and 4.2.7, the most intense fragment peaks were always from the $Ag_{x-1}^+$ ion, accompanying the loss of AgBr from $Ag_xBr^+$ ($x$ = even). In this work, I have focused our attention on the relative intensities of the peaks resulting from AgBr loss. However, a clear difference is recognized in the relative intensity between the unimolecular dissociation spectra and CID spectra of $Ag_xBr^+$. Relative intensities of the $Ag_{x-1}^+$ peaks are much higher in the unimolecular dissociation spectra than those in the CID spectra for the respective precursor ions. This clear difference can be attributed to the difference in the internal energy distribution of the produced excited precursor ion $Ag_xBr^{+*}$ as described below.

Figure 4.2.8 illustrates the internal energy distribution and dissociation channels of $Ag_xBr^{+*}$ in the cases of the unimolecular dissociation and high-energy CID, which are suggested by several works using thermometer molecules [22-26]. In the case of the unimolecular dissociation, the internal energy distribution of the excited precursor ions $Ag_xBr^{+*}$, which are generated by FAB, and reach the 3rd FFR without dissociation, is very narrow in width. Furthermore, it centers closely around the lowest dissociation energy limit. Therefore, the dissociation channel of the lowest energy is the most

accessible for the clusters with such low internal energies. Thus, the high intensity of AgBr loss in the unimolecular dissociation spectra suggests that the weakest bond in the mono-bromide $Ag_xBr^+$ cluster is the $Ag_{x-1}^+$ - AgBr bond.

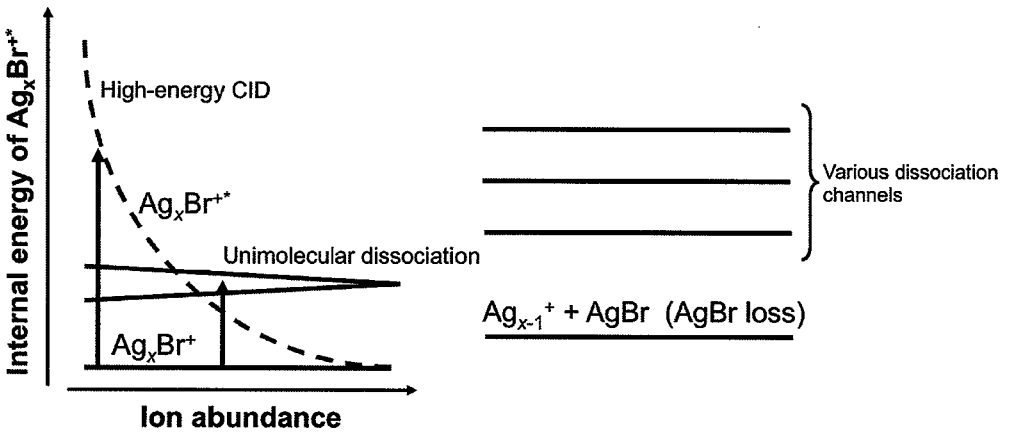


**Fig. 4.2.8.** Schematic representation of the internal energy distributions of $Ag_xBr^{+*}$ in the unimolecular dissociation and high-energy CID, which are indicated by the wedge-like solid and dotted lines, respectively.

Since our instrument is not capable of distinguishing sequential losses of Ag and Br atoms from the AgBr unit loss, it is certainly not clear whether the neutral fragment detached is a molecule of AgBr or a group of Ag + Br atoms. However, taking the bond energy of AgBr into account is of the magnitude of 2.61 - 2.71 eV [13], and thus, high energy is required to excite AgBr in the ionic ground state up to the dissociative covalent excited state at which the dissociation of AgBr occurs. The sequential losses of Ag and Br atoms therefore appear to be difficult with such low internal energies available in the unimolecular dissociation. Moreover, considering the stability of the neutral fragment; that is, while the neutral AgBr fragment has a closed-shell configuration, the neutral fragments (Ag + Br) formed by sequential losses of Ag and Br atoms have open-shell configurations. It therefore seems reasonable to conclude that the neutral fragment detached is AgBr.

In order to investigate the weakest bond in the mono-bromide $Ag_xBr^+$ cluster in further detail, I compared our experimental results with the calculated thermochemical data for $Ag_xBr^+$. The dissociation energies for $Ag_xBr^+$ ($x$ = 4, 6, 8, 10) are not found in literature, therefore in the current work, I am only concerned with $Ag_2Br^+$. The heats of

formation of $Ag_2Br^+$ along with those for the fragments formed via dissociation of $Ag_2Br^+$ are shown in Fig. 4.2.9. All the data are taken from Ref. [12].

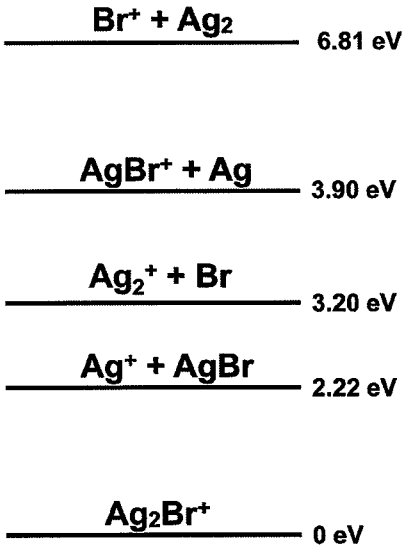


**Fig. 4.2.9.** Heats of formation for $Ag_2Br^+$ and those of the fragments formed via dissociation of $Ag_2Br^+$, relative to that of $Ag_2Br^+$ in the ground state. Thermochemical data were taken from reference [23].

The dissociation energies of $Ag_2Br^+$ into $Ag_2^+$ + Br, $AgBr^+$ + Ag, $Ag^+$ + AgBr, and $Br^+$ + $Ag_2$ are 3.20 eV, 3.90 eV, 2.22 eV, and 6.81 eV respectively. The dissociation energy of $Ag_2Br^+$ into $Ag^+$ + AgBr (at 2.22 eV) was determined to be the lowest among the $Ag_2Br^+$ for all the fragments. The finding that the dissociation energy necessary for breaking $Ag_2Br^+$ into $Ag^+$ + AgBr is the lowest among for of $Ag_2Br^+$ into all possible fragments. This may be why the highest intensities are for $Ag^+$ in the unimolecular dissociation spectrum of $Ag_2Br^+$. The results obtained in the current work for $Ag_2Br^+$ were in agreement with the calculated thermochemical data for $Ag_2Br^+$. Although I were concerned here only with $Ag_2Br^+$, the results for other silver bromide clusters $Ag_xBr^+$ ($x$ = 4, 6, 8, 10) will be discussed based on the success of the calculations for $Ag_xBr^+$.

The results of the relative intensities of $Ag_xBr^+$ ($x$ = 1 ~ 24) and the unimolecular dissociation of $Ag_xBr^+$ ($x$ = 2, 4, 6, 8, 10) lead us to the conclusion that a Ag-Br bond

exists in the $Ag_xBr^+$ ion cluster with the structural formula of the type $Ag_{x-1}^+(AgBr)$, and that the weakest bond in $Ag_{x-1}^+(AgBr)$ is the $Ag_{x-1}^+$ - AgBr bond.

In contrast to unimolecular dissociation, the broadly distributed and higher internal energies of the excited $Ag_xBr^{+*}$ precursor ion produced by collision with the target may provide many dissociation channels in addition to those involved with loss of AgBr. However, AgBr loss processes are primarily observed in CID and the high intensities of the product $Ag_{x-1}^+$ ions are reasonable. This is because in the high-energy CID, which has a maximum at the low energy limit and has a long tail to higher energy (beyond several electron volts), the lower-dissociation energy channel such as that for AgBr loss may remain dominant. It is also interesting that this trend is consistent, even compared with the new channels with the higher-dissociation energies, as shown in Fig. 4.2.8 [22-26].

In order to address the dissociation channels of CID of $Ag_xBr^+$ ($x$ = 2, 4, 6, 8, 10) in detail, the experimental results were compared with SJM electronic configurations. A summary of the results for the CID experiments is shown in Table 4.2.1. $Ag_xBr^+$ is thought to take a structural formula of the type $Ag_{x-1}^+(AgBr)$, even when it is a product ion. The SJM electronic configurations obtained for the precursor ions, product ions, and neutral fragments are also shown in Table 4.2.1. Here, in the case of Ag, $Ag^+$, Br, and $Br^+$, their inner electronic configurations are written as [Ar] and [Kr] in Table 4.2.1, which are the electronic configurations of Ar and Kr atoms, respectively. A SJM "closed"-shell configuration is denoted by CS, and indicates a cluster of high stability. The "ratio" in Table 4.2.1 indicates the ratio of the loss of a neutral fragment to that of AgBr. The intensities of other dissociation channels are normalized with the most intense peaks, which result from AgBr loss.

In the case of $Ag_3^+(AgBr)$, the product ions $Ag_3^+$ (ratio = 100) and $Ag^+(AgBr)$ (ratio = 42) are observed at a high ratio, as is listed in Table 4.2.1. These product ions are formed from the loss of AgBr and $Ag_2$, respectively. The neutral fragments have closed-shell configurations and, hence high stability. Therefore, the dissociation channels that yield these fragments are observed. The loss of AgBr is more frequently observed than that of $Ag_2$, because this dissociation channel generates the $Ag_3^+$ ion and the neutral fragment AgBr, both of which possess jellium shell closing (CS). On the other hand, the $Ag_2$ loss generates the product $Ag^+(AgBr)$ ion, which does not possess jellium shell closing.

**Table 4.2.1.** Summary of the results of the high-energy CID experiments. SJM electronic configurations are shown for the precursor ions, product ions, and neutral fragments. [Ar] and [Kr] represent the electronic configurations of Ar and Kr atoms, respectively. A SJM "closed"-shell configuration is denoted by CS, and indicates a cluster of high stability. The "ratio'' in the last column gives the values for the ratio of the loss of a neutral fragment compared to AgBr.

| Precursor ion | Product ion | Neutral loss | R (ratio) per AgBr loss |
|---|---|---|---|
| $Ag^+(AgBr)$ ($[Kr]4d^{10}$) | $Ag^+$; $[Kr]4d^{10}$ | AgBr; CS | 100 |
| | $Ag_2^+(AgBr)$; $1s^1$ | Br; $[Ar]3d^{10}, 4s^2, 4p^5$ | 67 |
| | $AgBr^+$; — | Ag; $[Kr]4d^{10}, 5s^1$ | 62 |
| | $Br^+$; $[Ar]3d^{10}, 4s^2, 4p^4$ | $Ag_2$; CS | <10 |
| $Ag_3^+(AgBr)$ (CS) | $Ag_3^+$; CS | AgBr; CS | 100 |
| | $Ag^+(AgBr)$; $[Kr]4d^{10}$ | $Ag_2$; CS | 42 |
| | $Ag_2^+(AgBr)$; $1s^1$ | Ag; $[Kr]4d^{10}, 5s^1$ | 30 |
| | $Ag_2^+$; $1s^1$ | Ag(AgBr); $[Kr]4d^{10}, 5s^1$ | <10 |
| | $Ag_4^+$; $1s^2, 1p^1$ | Br; $[Ar]3d^{10}, 4s^2, 4p^5$ | <10 |
| | $Ag^+$; $[Kr]4d^{10}$ | $Ag_2(AgBr)$; CS | <10 |
| | $AgBr^+$; — | $Ag_3$; $1s^2, 1p^1$ | <10 |
| $Ag_5^+(AgBr)$ ($1s^2, 1s^4$) | $Ag_5^+$; $1s^2, 1p^2$ | AgBr; CS | 100 |
| | $Ag_3^+(AgBr)$; CS | $Ag_2$; CS | 83 |
| | $Ag_3^+$; CS | $Ag_2(AgBr)$; CS | 34 |
| | $Ag_4^+(AgBr)$; $1s^2, 1p^1$ | Ag; $[Kr]4d^{10}, 5s^1$ | 24 |
| | $Ag_4^+$; $1s^2, 1p^1$ | Ag(AgBr); $[Kr]4d^{10}, 5s^1$ | <10 |
| | $Ag_2^+(AgBr)$; $1s^1$ | $Ag_3$; $1s^2, 1p^1$ | <10 |
| | $Ag^+(AgBr)$; $[Kr]4d^{10}$ | $Ag_4$; $1s^2, 1p^2$ | <10 |
| | $Ag_6^+$; $1s^2, 1p^3$ | Br; $[Ar]3d^{10}, 4s^2, 4p^5$ | <10 |
| | $Ag_2^+$; $1s^1$ | $Ag_3(AgBr)$; $1s^2, 1p^1$ | <10 |

| | | | |
|---|---|---|---|
| $Ag_7^+(AgBr)$ $(1s^2, 1p^4)$ | $Ag_7^+$; $1s^2, 1p^4$ | AgBr; CS | 100 |
| | $Ag_5^+(AgBr)$; $1s^2, 1p^2$ | $Ag_2$; CS | 61 |
| | $Ag_5^+$; $1s^2, 1p^2$ | $Ag_2(AgBr)$; CS | 50 |
| | $Ag_3^+(AgBr)$; CS | $Ag_4$; $1s^2, 1p^2$ | 12 |
| | $Ag_6^+(AgBr)$; $1s^2, 1p^3$ | Ag; $[Kr]4d^{10}, 5s^1$ | 11 |
| | $Ag_3^+$; CS | $Ag_4(AgBr)$; $1s^2, 1p^2$ | <10 |
| | $Ag_6^+$; $1s^2, 1p^3$ | Ag(AgBr); $1s^1$ | <10 |
| | $Ag_4^+$; $1s^2, 1p^1$ | $Ag_3(AgBr)$; $1s^2, 1p^1$ | <10 |
| | $Ag_2^+(AgBr)$; $1s^1$ | $Ag_5$; $1s^2, 1p^3$ | <10 |
| | $Ag_8^+$; $1s^2, 1p^5$ | Br; $[Ar]3d^{10}, 4s^2, 4p^5$ | <10 |
| | $Ag_4^+(AgBr)$; $1s^2, 1p^1$ | $Ag_3$; $1s^2, 1p^1$ | <10 |
| $Ag_9^+(AgBr)$ (CS) | $Ag_9^+$; CS | AgBr; CS | 100 |
| | $Ag_7^+$ ; $1s^2, 1s^4$ | $Ag_2(AgBr)$ ; CS | 58 |
| | $Ag_7^+(AgBr)$ ; $1s^2, 1p^4$ | $Ag_2$ ; CS | 36 |
| | $Ag_5^+(AgBr)$; $1s^2, 1p^2$ | $Ag_4$; $1s^2, 1p^2$ | 24 |
| | $Ag_5^+$ ; $1s^2, 1p^2$ | $Ag_4(AgBr)$ ; $1s^2, 1p^2$ | 22 |
| | $Ag_8^+$; $1s^2, 1p^5$ | Ag(AgBr); $1s^1$ | 13 |
| | $Ag_8^+(AgBr)$; $1s^2, 1p^5$ | Ag; $[Kr]4d^{10}, 5s^1$ | 14 |
| | $Ag_3^+(AgBr)$; CS | $Ag_6$; $1s^2, 1p^4$ | <10 |
| | $Ag_6^+$; $1s^2, 1p^3$ | $Ag_3(AgBr)$; $1s^2, 1p^1$ | <10 |
| | $Ag_3^+$; CS | $Ag_6(AgBr)$; $1s^2, 1p^4$ | <10 |
| | $Ag^+(AgBr)$ ; $[Kr]4d^{10}$ | $Ag_8$; CS | <10 |
| | $Ag_4^+$; $1s^2, 1p^1$ | $Ag_5(AgBr)$; $1s^2, 1p^3$ | <10 |
| | $Ag_{10}^+$; $1s^2, 1p^6, 1d^1$ | Br; $[Ar]3d^{10}, 4s^2, 4p^5$ | <10 |

In the case of $Ag_5^+(AgBr)$, the product ions $Ag_5^+$ (ratio = 100), $Ag_3^+(AgBr)$ (ratio = 83), and $Ag_3^+$ (ratio = 34) are primarily observed. These product ions are the result of losses of AgBr, $Ag_2$ and $Ag_2(AgBr)$, respectively. Since $Ag_2(AgBr)$ has a closed-shell configuration and high stability, the dissociation channels that yield these configurations are primarily observed. The losses of AgBr and $Ag_2$ are more frequently observed compared with that of $Ag_2(AgBr)$. Table 4.2.1 shows that the loss of AgBr is the dominant dissociation channel for these clusters, however, only $Ag_5^+(AgBr)$ is observed to have an additional dominant channel for the $Ag_2$ loss. The difference in the dissociation channels for $Ag_5^+(AgBr)$ and $Ag_x^+(AgBr)$ ($x$ = 3, 7, 9) may be explained by the SJM electronic configurations of the products formed from the $Ag_2$ loss. For $Ag_x^+(AgBr)$ ($x$ = 3, 7, 9), the loss of $Ag_2$ does not generate either the product ion or the neutral fragment, which possess the jellium shell closing. On the other hand, in the case of $Ag_5^+(AgBr)$ the loss of $Ag_2$ generates the ion $Ag_3^+(AgBr)$ and the neutral fragment $Ag_2$, both of which possess jellium shell closing. This may be why the $Ag_2$ loss attains such a high value for the ratio in the case of $Ag_5^+(AgBr)$.

Similarly, the main fragment peaks observed in the CID spectra of $Ag^+(AgBr)$, $Ag_7^+(AgBr)$ and $Ag_9^+(AgBr)$ may be explained in terms of stabilities of the generated product ions and neutral fragments. In summary, the dissociation channels in CID reflected the stabilities of the dissociation products. Namely, the dissociation channels, which generate both product ions and neutral fragments with even numbers of delocalized valence electrons, especially the closed-shell configurations, are primarily observed in the CID spectra; AgBr loss, $Ag_2$ loss, and $Ag_2(AgBr)$ loss. In contrast, the charged or uncharged clusters, with odd numbers of delocalized valence electrons, are not observed in the CID spectra as the primary fragmentation peaks (such as the Ag and Br loss). The present results indicate that based on SJM the relative intensities of the fragments observed in the CID spectra may be explained based on the stability of the dissociation products.

The relative intensities in the CID spectrum of $Ag_2Br^+$ are also discussed based on the thermochemical data, as in the case of unimolecular dissociation. The heats of formation for $Ag_2Br^+$ as well as those for the fragments formed via dissociation of $Ag_2Br^+$ in Fig. 4.2.9 were used. As described above, the internal energy distribution in high-energy CID decreases with increasing internal energy, whereas there is a finite probability of depositing more than several electron volts of energy [22-26]. The

dissociation energies of $Ag_2Br^+$ into $Ag_2^+$ + Br (at 3.20 eV), $AgBr^+$ + Ag (at 3.90 eV), and $Br^+$ + $Ag_2$ (at 6.81 eV) are higher than those of $Ag_2Br^+$ into $Ag^+$ + AgBr (at 2.22 eV). The dissociation energy of $Ag_2Br^+$ into $Ag^+$ + AgBr (at 2.22 eV) was determined to be the lowest among all the fragments for $Ag_2Br^+$. The finding that the dissociation energies of $Ag_2Br^+$ into $Ag^+$ + AgBr is the lowest for all fragments may explain why the highest intensity is for $Ag^+$ in all the high-energy CID spectra, regardless of the precursor ions. The relative intensities decrease in the order of $Ag^+ < Ag_2^+ < AgBr^+ < Br^+$. The dissociation energies for $Ag_2Br^+$ increase in the order of $Ag^+ + AgBr < Ag_2^+ + Br < AgBr^+ + Ag$. This indicates that the lower dissociation energies, the higher the relative intensities. The relative peak intensities of fragment ions may also be explained by the dissociation energies of $Ag_2Br^+$. These decay channels for $Ag_2Br^+$ are in good agreement with the calculated thermochemical data. The dissociation mechanisms for $Ag_xBr^+$ ($x > 4$), however, cannot be explained by the thermochemical data at this time because the calculation for $Ag_xBr^+$ ($x > 4$) cannot be found in the literature. When the dissociation energies for $Ag_xBr^+$ ($x > 4$) clusters are reported, the results found in the current work may be useful if compared with the results of the calculations and may provide new insight into the dissociation of mono-bromide silver clusters.

In this section, it was demonstrated that dissociation of singly charged silver bromide clusters induced by collision with the rare gas target could be investigated. In the next section, dissociation of singly charged silver bromide cluster and silver cluster induced by collision with an alkali metal target is investigated.

## References


[1] S.K. Kang, S.K. Yoon, Y.M. Kim, Org. Lett. 3 (2001) 2697.

[2] A. Ramirez-Solis, J.P. Daudey, J. Chem. Phys. 120 (2004) 3221.

[3] A. Schulz, M. Hargittai, Chem.-Eur. J. 7 (2001) 3657.

[4] P.D. Mitev, M. Saito, Y. Waseda, Mater. Trans. 42 (2001) 829.

[5] A.D. Cicco, M. Taglienti, M. Minicucci, A. Filipponi, Phys. Rev. B 62 (2000) 12001.

[6] N.F. Mott, R.W. Gurney, *Electronic processes in ionic crystals*, 2nd edn, Oxford Press, New York, 1950.

[7] J. W. Mitchell, Photogr. Sci. Eng, 25 (1981) 170.

[8] J. F. Hamilton, Adv. Phys. 37 (1988) 359.

[9] D.L. Hildenbrand, K.H. Lau, J. Phys. Chem. A 109 (2005) 11328.

[10] J.M. L'Hermite, F. Rabilloud, L. Marcou, P. Labastie, Eur. Phys. J. D 14, (2001) 323.

[11] J.M. L'Hermite, F. Rabilloud, P. Labastie, F. Spiegelman, Eur. Phys. J. D 16 (2001) 77.

[12] F. Rabilloud, F. Spiegelmann, J.L Heully, J. Chem. Phys. 111 (1999) 8925.

[13] F. Rabilloud, F. Spiegelman, J.M. L'Hermite, P. Labastie, J. Chem. Phys. 114 (2001) 289.

[14] H. Nagao, K. Awazu, S. Hayakawa, K. Iwamoto, M. Toyoda, T. Ichihara, Eur. Phys. J. D 45 (2007) 279.

[15] C.K. Fagerquist, D.K. Sensharma, M.A. El-Sayed, J. Phys. Chem. 95 (1991) 9176.

[16] H.-C.M. Rosing, A. Schulz, M. Hargittai, J. Am. Chem. Soc. 127 (2005) 8133.

[17] A. Ramırez-Solıs, J. Chem. Phys. 120 (2004) 2319.

[18] H. Zhang, Z.A. Schally, D.S. Marynick, J. Phys. Chem. A 104 (2000) 6287.

[19] G. N. Khairallah, R. A. O'Hair, Angew. Chem. Int. Ed. 44 (2005) 728.

[20] G. N. Khairallah, R. A. O'Hair, Dalton Trans. (2007) 3149.

[21] G. N. Khairallah, R. A. O'Hair, Dalton Trans. 2956 (2008).

[22] V.H. Wysocki, H.I. Kenttamaa, R.G. Cooks, Int. J. Mass Spectrom. Ion Process. 75 (1987) 181.

[23] K.L. Schey, H.I. Kenttamaa, V.H. Wysocki, R. Graham Cooks, Int. J. Mass Spectom. Ion Process. 90 (1989) 71.

[24] V.H. Wysocki, H.I. Kenttamaa, R.G. Cooks, J. Phys. Chem. 92 (1988) 6465.

[25] S.R. Horning, M. Vincenti, R.G. Cooks, J. Am. Chem. Soc. 112 (1990) 119.

[26] S. Hayakawa, K. Harada, K. Arakawa, N. Morishita, J. Chem. Phys. 112 (2000) 8432.

[27] J.L. Martins, R. Car, J. Buttet, J. Surf. Sci. 106 (1981) 265

[28] W. Ekardt, Phys. Rev. B 29 (1984) 1558.

[29] W.A. de Heer, W.D. Knight, M.Y. Chou, M.L. Cohen, Solid State Phys. 40 (1987) 93

[30] M.L Cohen, M.Y Chou, W.D. Knight, W.A. de Heer, J. Phys. Chem. 91 (1987) 3141.

[31] I. Katakuse, T. Ichihara, Y. Fujita, T. Matsuo, T. Sakurai, H. Matsuda, Int. J. Mass Spectrum. Ion Process. 67 (1985) 229.

[32] I. Katakuse, T. Ichihara, Y. Fujita, T. Matuso, T. Sakurai, H. Matsuda, Int. J. Mass Spectrom. Ion Process. 74 (1986) 33.

[33] I. Katakuse, T. Ichihara, Y. Fujita, T. Matuso, T. Sakurai, H. Matsuda, Int. J. Mass Spectrom. Ion Process. 69 (1986) 109.

[34] W. Begemann, K.H. Meiwes-Broer, H.O. Lutz, Phys. Rev. Lett. 56 (1986) 2248.

[35] S. Hayakawa, A. Kitaguchi, S. Kameoka, M. Toyoda, T. Ichihara, J. Chem. Phys. 124 (2006) 224320.

[36] P. Shrape, C.J. Cassady, Chem. Phys. Lett. 191 (1992) 111.

[37] C.K. Fagerquist, D.K. Sensharma, M.A. El-Sayed, J. Phys. Chem. 95 (1991) 9169.

[38] C. Brechignac, P. Cahuzac, J. Leygnier, I. Tigneres, Chem. Phys. Lett. 303 (1999) 304.

[39] C. Brechignac, P. Cahuzac, M. de Frutos, P. Garnier, Z. Phys. D. 42 (1997) 303.

[40] R. Antoine, P. Dugourd, D. Rayne, E. Benichou, M. Broyer, J. Chem. Phys. 107 (1997) 2664.

## 4.3 Dissociation channels of silver bromide cluster $Ag_2Br$, silver cluster $Ag_3$ and their ions studied by using the alkali metal target

### 4.3.1 Introduction

In this section, dissociation of silver bromide cluster, silver cluster, and their ions induced by collision with the alkali metal target is described.

Silver bromide has been studied for many years in the condensed phase due to its important implications in the photographic process. In order to clarify the reactions involved in the process, both of silver and silver bromide clusters have been widely investigated [1]. The silver clusters have also received particular attention because of a theoretical interest in the fact that a silver atom has electrons in the outer 4*d*-orbitals energetically overlapped by the partially filled 5*s*-orbital.

Silver trimers have been a main topic of a large number of earlier experimental [2-8] and theoretical [1, 9-18] studies. Among other experimental works on small silver clusters, Spasov *et al.* reported the fragmentation patterns, cross sections, and dissociation energies of anionic silver clusters $Ag_n^-$ by using the energy-resolved CID method [6]. The main reaction channels were found to be the eliminations of a Ag atom and a dimer $Ag_2$, with the dimer less favored for odd n values. Dissociation energies for the loss of a silver atom showed a strong odd-even-dependent alternation against n. Handschuh *et al.* studied photoelectron spectra of silver anion clusters by exciting at different photon energies in order to explore the electronic structures of various silver clusters [5]. The shaper spectral patterns of the silver clusters observed in their experiments as compared with those of the corresponding alkali metal clusters might be due to the stronger bonding in the silver clusters. This can be interpreted as the result of overlapping of the outer 4*d* and 5*s* orbitals, which gives rise to van der Waals type attractive force. Recently the symmetric and antisymmetric vibrational bands of neutral $Ag_3$ were assigned by using far-infrared spectroscopy by Fielicke *et al.* [8]. The energy levels of the silver clusters and their ions were theoretically evaluated [1, 9-18].

Regarding the dissociation methods, electronic mechanism (electronic excitation) and impulsive mechanism (momentum transfer) about initial steps of collision induced dissociations have been discussed using position sensitive detections [19-24]. Barat and coworkers differentiated between electronic and impulsive mechanism in the CID for the collisions of cluster ions with $H_2$ or rare gas targets by detecting both fragment ions

and fragment neutrals [20-24]. After the excitation by impulsive mechanism, the excited molecules dissociate through the internal collisions in the second step. For the experiment using metal targets, de Bruijn *et al.* [19] indicated that dissociative electron transfer initiated by the electron mechanism dominated molecular dissociation. One of the authors also confirmed the electron transfer mechanism by charge inversion mass spectrometry using alkali metal targets [25]. Femtosecond negative to neutral to positive (NeNePo) spectroscopy was used to study the structural dynamics of the neutral cluster $Ag_3$ [26-28]. The wave packet dynamics along the coordinate of the linear-to-triangular rearrangement on the ground state potential surface was investigated in detail by Boo *et al.* [27]. These authors commented on the splitting of the degeneracy of the neutral $Ag_3$ states due to a strong Jahn-Teller effect. Leisner *et al.* [28] indicated an apparent loss of vibrational coherence by the ultrafast intramolecular vibrational energy redistribution interpretable as an intermolecular collision process. These experimental results have been confirmed by the theoretical studies [29-33].

Mixed clusters have been also an object of recent researches. Metastable fragmentation channels for anionic and cationic silver bromide clusters were examined by L'Hermite *et al.* [34, 35] and were compared with *ab initio* DFT results [36, 37]. They indicated that the fast fragmentation induced by a UV laser made the cations lose a bromine atom more easily than a silver ion and that the negative ions mass spectra contained species with more silver atoms than required by stoichiometry. Contrary to the silver clusters, dissociation processes of the neutral silver bromide clusters are not known to our best knowledge.

In this study, the dissociation processes of the cations of both silver trimer ($Ag_3$) and silver bromide cluster ($Ag_2Br$) were investigated by high-energy CID spectra measured by using the Cs metal target. As has been confirmed from their internal energy distributions [38, 39], the dissociation processes in the high-energy CID spectra do not depend on which of alkali metal and rare gas targets is employed [39, 40]. Furthermore, the dissociation processes of their neutrals were investigated by charge inversion mass spectrometry with alkali metal targets, which has been developed in our laboratory [39, 41, 42]. Charge inversion mass spectrometry can provide us with direct information about the dissociation pathway of energy-selected neutral clusters formed by the near-resonant neutralization of the corresponding cation clusters [39, 41, 42]. The reaction process involved in this spectroscopy corresponds to a reverse process of

NeNePo [26-28]. Dissociation mechanisms of small clusters are particularly interesting from the viewpoint of chemical reactivity, because the small clusters often exhibit significantly different physical and chemical properties from those in the isolated molecular state or in the condensed phase. In the present work, the dissociation mechanisms of the excited silver trimer $Ag_3$ and silver bromide cluster $Ag_2Br$ were investigated by the charge inversion mass spectrometry. The obtained charge inversion mass spectra showed a significant difference between $Ag_3$ and $Ag_2Br$. The difference is discussed in terms of the energy levels of the respective excited neutral clusters and relevant fragments.

## 4.3.2 Experimental section

Mass-selected positive ions were made to collide with an alkali metal target, and the resulting negative ions formed upon two successive single-electron transfers were mass analyzed by using an MS/MS instrument. Silver bromide cluster ions and silver cluster ions were generated in the same way as in section 4.2. The alkali metal was introduced into the collision cell as a vapor from a reservoir through a ball valve. In this work, cesium (Cs) was used as a target vapor. The temperatures of the collision cell, the ball valve, and the reservoir were controlled to adjust the density of the Cs vapor in the collision cell. Neutralization, dissociation, and negative ion formation took place in the collision cell containing the Cs vapor. The negative ions were mass analyzed by a ESA). The mass-analyzed ions were detected by a 9 kV post-acceleration secondary electron multiplier, which could detect both positive and negative ions upon the application of an appropriate polarity. Charge inversion spectra were measured by mass-analyzing the negative ions exiting from the collision cell by scanning the ESA voltage. By changing the polarities of MS-II and multiplier, the CID spectra of the positive ions exiting from the collision cell were measured in the same way as for the negative ions.

## 4.3.3 Results and Discussion

### 4.3.3.1 Silver bromide cluster $Ag_2Br$

A CID spectrum and a charge inversion spectrum of the silver bromide cluster ion $^{107}Ag_2{}^{79}Br^+$ (*m/z* 293) measured with the Cs target are shown in Figs. 4.3.1(a) and (b), respectively. Mono-isotopic precursor ions were selected.

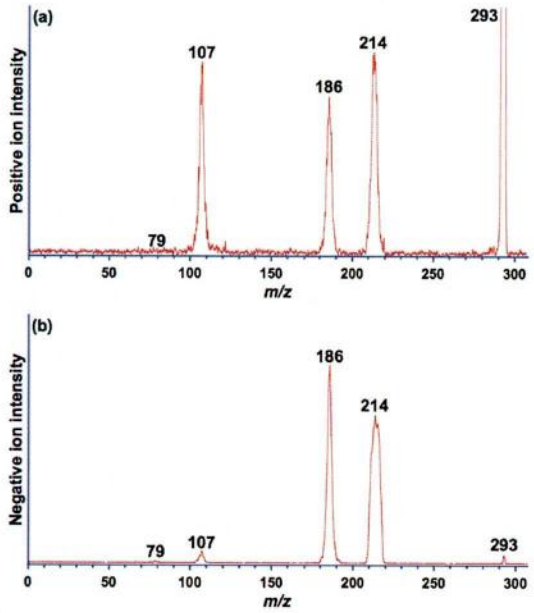


**Fig. 4.3.1.** High-energy CID spectrum (a) and charge inversion spectrum (b) of $Ag_2Br^+$ (*m/z* 293). The ion was formed by fast atom bombardment (FAB). The target element was Cs and the collision energy was 5 keV.

A clear difference is recognized between the CID spectrum and the charge inversion spectrum of $Ag_2Br^+$. In the CID spectrum [Fig. 4.31(a)], the peak for the undissociated ion $Ag_2Br^+$at *m/z* 293 is by far the strongest and well exceeds the upper limit of the scale on the vertical axis. The high intensity of this $Ag_2Br^+$ peak is attributed to the precursor ion that did not interact with the target. The peaks located at *m/z* 107, 186, and 214 are observed dominantly and are associated with $Ag^+$, $AgBr^+$, and $Ag_2^+$ ions resulting from the loss of AgBr, Ag, and Br from the precursor ion $Ag_2Br^+$, respectively. The peak located at *m/z* 79 and associated with $Br^+$ ion is scarcely observed.

The investigation by L'Hermite *et al.* [34] showed that only the peak associated with $Ag^+$ formed by the loss of AgBr was observed in the metastable fragmentation of $Ag_2Br^+$. The lowest dissociation channel of $Ag_2Br^+$ derived from *ab initio* DFT calculations is in a satisfactory agreement with their experimental results, and is able to account for the dissociation channel of $Ag_2Br^+$ which dissociates preferentially into $Ag^+$ + AgBr. In contrast to the metastable fragmentation, the peaks associated with $Ag^+$, $AgBr^+$, and $Ag_2^+$ were dominantly observed in the present high-energy CID spectrum of $Ag_2Br^+$. The difference in the dissociation channels between the high-energy CID and

the metastable fragmentation was explained by the internal energy distribution in $Ag_2Br^{+*}$. The energy distribution of the metastable ions produced thus is very narrow and centers closely around the lowest dissociation energy limit. The low internal energy available in the metastable fragmentation yields only the peak associated with $Ag^+$ formed from the loss of AgBr. On the contrary to this, high-energy CID has a maximum of distribution at the low energy limit and shows a long tail extending to the higher energy beyond several electron volts [38, 45-48]. The broad and higher internal potential energy of $Ag_2Br^{+*}$ examined in the present work allows many dissociation channels such as the loss of any one of Br, Ag, AgBr, and $Ag_2$.

The charge inversion spectrum of the silver cluster ion $Ag_2Br^+$ (*m/z* 214) with the Cs target is shown in [Fig. 4.3.1(b)]. The peaks located at *m/z* 186 and 214 are associated with $AgBr^-$ and $Ag_2^-$, respectively and are the dominant peaks in the charge inversion spectrum [Fig. 4.3.1(b)], whereas the peak at *m/z* 293 associated with the undissociated ion $Ag_2Br^-$ is hardly observed. The peaks associated with $Br^-$ and $Ag^-$ are also observed at *m/z* 79 and 107, but their intensities are much weaker than those for $Ag_2^-$ and $AgBr^-$. In order to elucidate the mechanism of dissociation of the excited cluster $Ag_2Br^*$, I compared our experimental results with the thermochemical data available. These thermochemical data for the $Ag_2Br$ system are illustrated in Fig. 4.3.2 together with the energy levels associated with the near-resonant neutralization using the Cs target. The heats of formation of $Ag_2Br^+$, $Ag_2Br$, and those of the fragments formed via dissociation of $Ag_2Br$, relative to that of the ground state of the $Ag_2Br$ neutral are given in Fig. 4.3.2. Since the ionization potential and dissociation energies of $Ag_2Br$ have not been reported experimentally, theoretically calculated values are used. Most of the data are taken from Refs. [36, 37]. The bond dissociation energies of the Ag-Br and Ag-Ag bonds are also taken from Ref. [37]. In our previous studies using thermometer molecules, such as $W(CO)_6$, which lose CO ligands consecutively when they have enough energy to dissociate [38, 39, 49], it was demonstrated that the neutralization step in the charge inversion process is via near-resonant electron transfer. Therefore, when this is the case, the energy level of the neutral species formed should be lower than the level of the corresponding precursor ion by an amount equal to the ionization energy of the target atom. The energy level associated with the resonance process with the Cs target is shown as a dashed line (at 2.72 eV) in Fig. 4.3.2. Dissociations into $Ag_2$ + Br and AgBr + Ag are energetically allowed when the

neutralization is a near-resonant process, because the energy level of $Ag_2$ + Br (at 1.84eV) and AgBr + Ag (at 0.75 eV) are lower than that of $Ag_2Br^*$ (at 2.72 eV) by 0.88 and 1.97 eV, respectively, as is shown in Fig. 4.3.2. The dissociation into 2Ag + Br (at 3.36 eV) is, however, energetically impossible, since it is 0.64 eV higher than that of $Ag_2Br^*$ as is also shown in Fig. 4.3.2. From a comparison with the thermochemical data, all the fragment ions observed in the charge inversion spectrum are supposed to be formed by the dissociation of $Ag_2Br^*$ into AgBr + Ag and $Ag_2$ + Br. The very weak intensity observed for the undissociated $Ag_2Br^-$ ion indicates that the excited neutral species $Ag_2Br^*$ has sufficient internal energy to dissociate before the second electron transfer occurs. Thus, the dissociation behavior of $Ag_2Br^*$ revealed in the charge inversion spectrum is explained by the calculated thermochemical data.

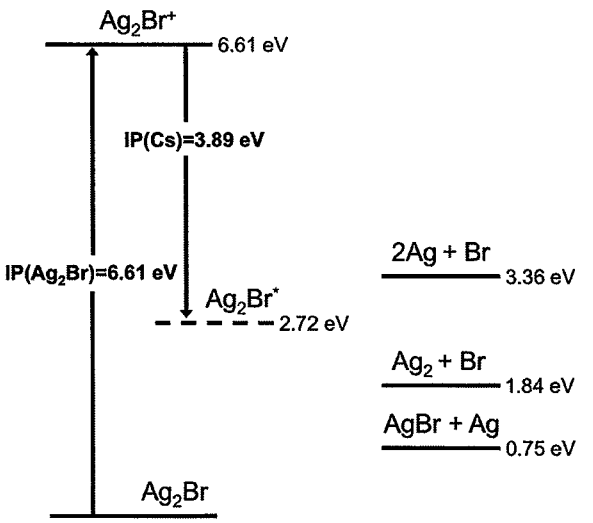


**Fig. 4.3.2.** Heats of formation of the neutral and cationic forms of $Ag_2Br$, relative to that of $Ag_2Br$ in the ground state. The thermochemical data are taken from Ref. [15, 16]. The dashed line shows the energy level predicted by the near-resonant neutralization with a Cs target.

### 4.3.3.2 Silver cluster $Ag_3$

The CID and charge inversion spectra of the silver cluster ion $^{107}Ag_3^+$ (*m/z* 321) recorded with the Cs target are shown in Fig. 4.3.3. The fragment peaks associated with $Ag^+$ (*m/z* 107) and $Ag_2^+$ (*m/z* 214) are observed in the CID spectrum [Fig. 4.3.3(a)], and the intensity of $Ag^+$ is much weaker than that of $Ag_2^+$. The strongest peak at *m/z* 321

was attributed to the undissociated precursor ion that did not interact with the target, as was done in analyzing the CID spectrum of $Ag_2Br^+$ shown in Fig. 4.3.2.

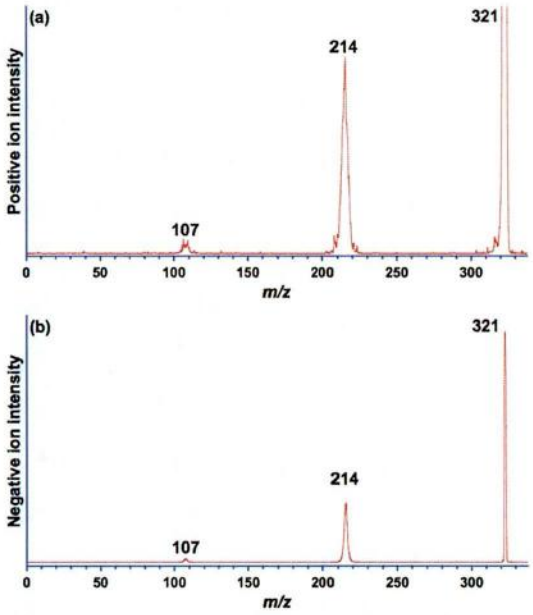


**Fig. 4.3.3.** High-energy CID spectrum (a) and charge inversion spectrum (b) of $Ag_3^+$ (*m/z* 321). The ion was formed by fast atom bombardment (FAB). The target element was Cs and the collision energy was 5 keV.

The low-energy dissociation channel of the silver cluster ion $Ag_3^+$ determined by CID using a Penning trap was reported by Kruckeberg *et al.* [7]. In their CID experiment, the cyclotron motion of the cluster ions was excited by a 1 ms resonant excitation pulse and an argon gas pulse was directed into the trap volume. A storage period of 100 ms there allowed the clusters to collide with argon atoms and to decay to smaller neutral or ion fragments. In their low-energy and multiple-collision CID experiment, the $Ag_3^+$ ions decayed predominantly into $Ag^+$ ions, which were presumably produced by the evaporation of silver dimer $Ag_2$. On the other hand, the dissociation energy of $Ag_3^+$ into $Ag_2^+ + Ag$ calculated theoretically by Huda *et al.* [17], is 2.374 eV and lower than that of 2.533 eV required for the dissociation into $Ag_2 + Ag^+$. In the high-energy CID spectrum of $Ag_3^+$ measured in the present work, I observed the ion $Ag_2^+$, which was formed by loss of a Ag atom, as a predominant fragment peak. The differences in the dissociation channels between the low-energy and high-energy CID can be again

understood by considering the internal energy distribution in $Ag_3^{+*}$. High-energy CID has a maximum of distribution at the low energy limit and shows a long tail extending to the higher energy beyond several electron volts [38, 45-48]. For low-energy CID, the energy distribution is controlled by changing the collision energy and the times of collisions, and both low-energy and high-energy tails are short [47]. Therefore, if the theoretical calculation of the dissociation energy of $Ag_3^+$ is relied on, then the higher preference of the lower-dissociation-energy channel of Ag elimination in the high-energy CID experiment is explained by the internal energy distribution localized mostly in the low energy region.

The charge inversion spectrum of the silver cluster ion $^{107}Ag_3^+$ (*m/z* 321) measured with the Cs target is shown in Fig. 4.3.3(b). Peaks associated with $Ag^-$, $Ag_2^-$, and $Ag_3^-$ are observed. The peak for the undissociated ion $Ag_3^-$ is predominantly observed at *m/z* 321, whereas the peak at *m/z* 293 associated with the undissociated ion $Ag_2Br^-$ was hardly observed in the charge inversion spectrum of $Ag_2Br^+$ ions [Fig. 4.3.1(b)]. The predominant peak of undissociated $Ag_3^-$, which makes a great contrast to the case described above for $Ag_2Br$, is unusual, since the electronically excited species formed from their corresponding positive ions are not usually observed in charge inversion spectra because of their rapid fragmentations driven by sufficient internal energies. In the previous studies using the charge inversion mass spectrometry, undissociated charge inverted ions were observed only for atomic [50], $C_2$ and $C_2H$ anions [51, 52] formed by double-electron transfer in a single collision. When an alkali metal is used as a target, the double-electron transfer in a single collision is much less probable than successive single-electron transfers in two collisions, as was discussed previously by one of the present authors [42, 50]. The successive electron transfers do not often yield stable anions, even if the intermediate neutral clusters or molecules have positive electron affinities, as has been known in the case of vinylidene [53, 54] or $CH_n$ [55]. Only one exception for the formation of negative ions by the successive single-electron transfers was observation of an undissociated anion of H- atom adduct Gly-Pro, in which the ring opening of the proline residue took place by N-Cα bond cleavage [56]. The small peaks at *m/z* 107 and 214 shown in [Fig. 4.3.3(b)] are associated with Ag and $Ag_2$, respectively, which are the fragments expected from the dissociation of $Ag_3$ into $Ag_2$ + Ag. The intensity difference between $Ag^-$ and $Ag_2^-$ results from a difference in the cross section for the negative ion formation as well as in

the detection efficiency of a post-acceleration secondary multiplier. Such difference in the peak intensity between the complementary fragments has been observed for isomeric dichlorobenzenes [42, 57, 58] and isomeric chlorophenols [59].

In order to clarify the mechanism of the process from the positive ion $Ag_3^+$ to the negative ion $Ag_3^-$ via successive single-electron transfers in two collisions, I compared the experimental results with the thermochemical data. The thermochemical data for the $Ag_3$ system were calculated by many researchers [1, 9-18]. Recently calculated values reported by Huda *et al.* [17] are illustrated in Fig. 4.3.4 (a).

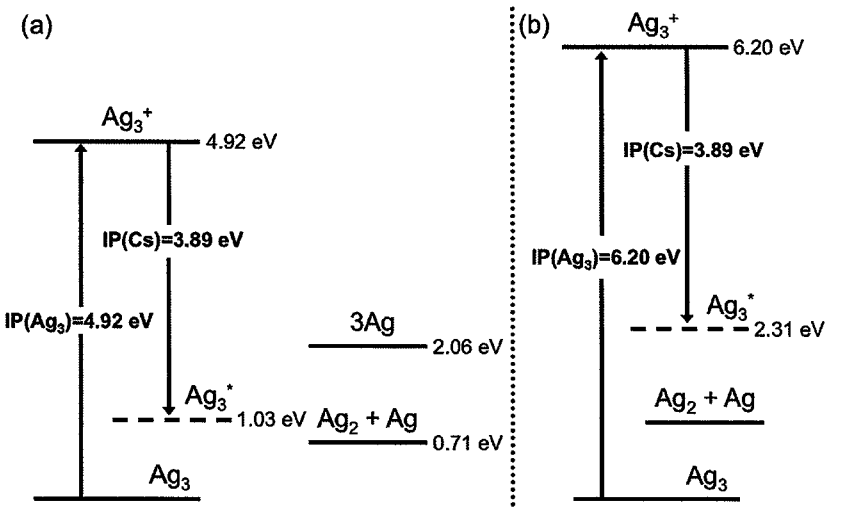


**Fig. 4.3.4.** Heats of formation of the neutral and cationic forms of $Ag_3$, and their fragments relative to that of $Ag_3$ in the ground state. Panels (a) and (b) show the theoretical and experimental values, respectively. The thermochemical data are taken from Ref. [40, 41, 19]. The dashed lines show the energy levels predicted by the near-resonant neutralization with a Cs target.

The energy level associated with the near-resonance neutralization with the Cs target is shown by a dashed line (at 1.03 eV) and is higher by 0.32 eV than that of $Ag_2$ + Ag (at 0.71 eV) but 1.03 eV lower than that of 3Ag (at 2.06 eV). The thermochemical data show that the dissociation of $Ag_3$ into three Ag atoms is energetically impossible but the dissociation of $Ag_3$ into $Ag_2$ + Ag is allowed. However, the predominant peak observed for $Ag_3$ in the charge inversion spectrum shown in Fig. 4.3.3 (a) indicates that the $Ag_2$-Ag bond cleavage in $Ag_3^*$ is unfavorable. The thermochemical data based on the

experimental work are also reported by Ho *et al.* [3] and Jackschath *et al.* [4] and these experimental values are given in Fig. 4.3.4(b). The vertical ionization energy of $Ag_3$ was obtained as 6.2 eV from an appearance energy by electron impact ionization [4], and the bond dissociation energy of $Ag_2$ - Ag was estimated as 0.97 ± 0.16 eV using photoelectron spectroscopy of $Ag_3^-$ [3]. Except these works, there are no experimental data available for both the ionization energy and bond dissociation energy of $Ag_3$. The differences in ionization energy and in the bond dissociation energy between the experimental and theoretical values are 1.3 eV and 0.3 eV, respectively, as is seen from Fig. 4.3.4. Although a part of this large difference in the ionization energy between the experimental and theoretical values may be rationalized by ascribing it to the difference between the vertical and adiabatic values, the difference of 1.3 eV is still too large. The ionization energy evaluated from the appearance energy by electron impact [4] is not so reliable. For example, the observation of $Ag_3^+$ by two photon ionization at 410 nm in the NeNePo experiments reported by Boo *et al.* [27] indicates that the ionization energy is lower than 6.05 eV which is 0.15 eV smaller than the ionization energy determined by the electron impact method. The energy level of 2.31 eV by the near-resonant neutralization shown as the dashed line in Fig. 4.3.5(b) is higher approximately by 1.30 eV than the experimental value for the dissociation into $Ag_2$ + Ag (at ca.1.0 eV). The thermochemical values evaluated from both theoretical and experimental values cannot explain the dominating presence of the undissociated ion $Ag_3^-$ in the charge inversion spectrum.

#### 4.3.3.3 Dissociation energies and mechanisms for the formation of undissociated $Ag_3^-$

By using the thermometer molecules, it has been demonstrated that the formation process of the negative ions in the charge inversion mass spectrometry proceeds via near-resonant neutralization with an alkali metal target, followed by spontaneous dissociation of the neutrals and the endothermic negative ion formation upon a second collision with the alkali metal target, as shown in the following reaction scheme (4-3-1) [38, 39, 42, 49].

**Scheme (4-3-1)**

$$AB^+ + T \rightarrow AB^* + T^+,$$
$$AB^* \rightarrow A + B,$$

$$A \text{ (or B)} + T \rightarrow A^- \text{ (or } B^-) + T^+,$$

where AB and T indicate a projectile and a target, respectively. The charge reversal reactions in the femtosecond negative to neutral to positive (NeNePo) spectroscopy in which an electron is photo-detached from a negative ion, followed by two-photon ionization to a positive ion [26-28], as shown in the following reaction scheme (4-3-2), correspond to the reverse processes to our charge inversion processes.

**Scheme (4-3-2)**

$$AB^-(\text{linear}) + h\nu \rightarrow AB(\text{linear}) + e^-,$$

$$AB(\text{linear}) \rightarrow AB(\text{bent}),$$

$$AB(\text{bent}) + 2\ h\nu \rightarrow AB^+ + e^-.$$

A large number of theoretical calculations [1, 9-18] have been performed to determine the structures and energies of silver trimers ($Ag_3^-$, $Ag_3$, and $Ag_3^+$) and it has been confirmed that $Ag_3$ and $Ag_3^+$ assume triangular forms at their global potential minima but $Ag_3^-$ takes a linear form. The investigation using the femtosecond NeNePo spectroscopy suggested that the linear cluster $Ag_3$ produced by the photodetachment of the linear ion $Ag_3^-$ rearranged into a triangular form on a 1 ps timescale due to a very low isomerization barrier as compared with that for the decomposition [26-28]. This very fast rearrangement was confirmed by a few theoretical works [29-33]. In the NeNePo experiment, $Ag_3^+$ ions were produced by the two-photon ionization of $Ag_3$ neutral clusters. The constant signal intensity of $Ag_3^+$ after 2 ps from the ionization preceded by the electron detachment of $Ag_3^-$ indicated that an equilibrium between the linear and triangular forms of $Ag_3$ was achieved within a few ps [27, 28].

The excited states of the linear and triangular forms of $Ag_3$ were also reported [1, 10, 14, 15]. Fig. 4.3.5 shows the calculated electronic energy levels of $Ag_3^-$, $Ag_3$, and $Ag_3^+$ along the bending coordinate taken from Ref. [27]. Typical collision interaction times for the neutralization in which the precursor ions are accelerated by 5.0 kV is in the range of $10^{-14}$ s. Since this time is significantly shorter than the time required for a conventional vibration ($\approx 10^{-13}$ s), the neutralization is expected to be a Franck-Condon process. Consequently, the geometry of the electronically excited cluster $Ag_3^*$ is presumed to remain the same as that of the precursor ion $Ag_3^+$. As shown in Fig. 4.3.5, the energy levels of 2E' (at 4.6 eV) and $2A_1$' states (at 4.7 eV) of the triangular cluster $Ag_3^*$ match the excitation energy (at 4.4 eV) required for the near-resonant neutralization with the Cs target, which is lower than the energy level of the precursor

ion (at 8.3 eV) by an amount equal to the ionization energy of the Cs target (3.89 eV). Since the energy level is much higher than the isomerization barrier between the linear and triangular forms, the intramolecular rearrangement by ultra fast vibrational energy redistribution can occur on a ps time scale as reported in the NeNePo experiments [26-28].

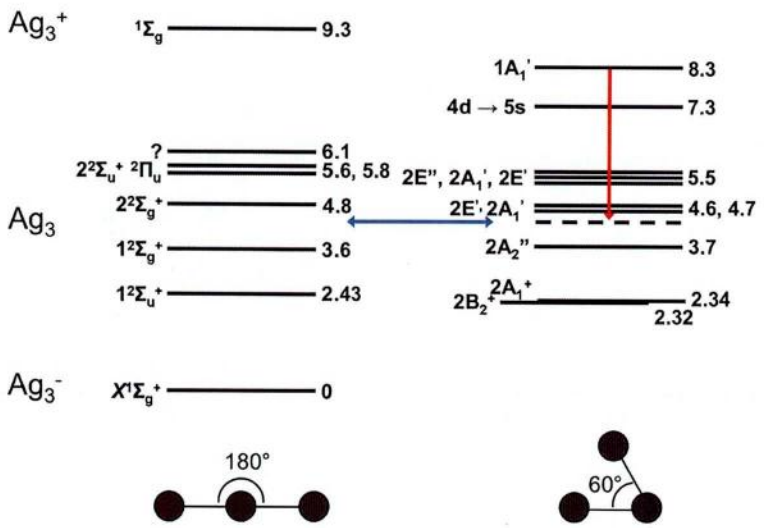


**Fig. 4.3.5.** Calculated transition energies of $Ag_3^-$, $Ag_3$, and $Ag_3^+$ along the bending coordinate. The thermochemical data are taken from Ref. [7].

As the average free time between the neutralization and anionization in the collision cell is 0.35 μs, the equilibrium between the linear and triangular forms is expected to be fully achieved provided that the dissociation does not take place because of the high dissociation barrier. On the basis of above discussion, I assumes that the linear cluster $Ag_3$ which has the higher electron affinity than that of the bent cluster captures another electron from the Cs target and, hence, the linear cluster ion $Ag_3^-$ is observed in the charge inversion spectrum of $Ag_3^+$. From a comparison with the NeNePo experiments of $Ag_3^-$, it is presumed that $Ag_3^*$ formed from $Ag_3^+$ by the near-resonant neutralization with the Cs target does not dissociate due to the energy barrier too high for the dissociation into $Ag_2$ + Ag and, instead, $Ag_3$ does intramolecular rearrangement to the linear neutral cluster $Ag_3$, followed by negative ion formation on another collision with the target, as is expressed in the following reaction scheme (4-3-3).

**Scheme (4-3-3)**

$$AB^{+}(bent) + T \rightarrow AB^{*}(bent) + T^{+},$$

$$AB^{*}(bent) \rightarrow AB^{*}\ (linear),$$

$$AB^{*}\ (linear) + T \rightarrow AB^{-}\ (linear) + T^{+}.$$

From the existence of the predominant peak for the undissociated cluster ion $Ag_3^-$ in the charge inversion spectrum, I inferred that the energy barrier for the dissociation into $Ag_2$ + Ag is higher than the energy level of $Ag_3^*$ formed via near-neutralization with the Cs target, though the energy barrier theoretically calculated has not been reported so far.

### 4.3.3.4 Dissociation mechanism and structure of $Ag_2Br^+$

To see the peak shape more clearly, the charge inversion spectra of $^{107}Ag_2{}^{79}Br^+$ and $^{107}Ag_3^+$ expanded in the *m/z* 170-230 range are shown in Figs. 4.3.6(a) and (b), respectively.

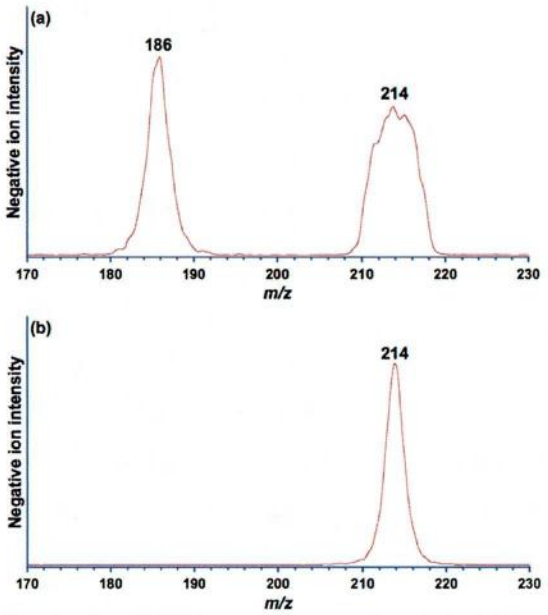


**Fig. 4.3.6.** Charge inversion spectra of the $Ag_2Br^+$ (*m/z* 293, Fig. 4.3.1) (a) and $Ag_3^+$ (*m/z* 321, Fig. 4.3.3) (b) enlarged in the range m/z 170-230.

While in the case of $Ag_3^+$, the peak associated with $Ag_2^-$ at *m/z* 214 in Fig. 4.3.6 (b) is sharp and its peak shape resembles a triangle, the peak at *m/z* 214 derived from $Ag_2Br^+$ shown in Fig. 4.3.6 (a) is broad and its band shape resembles a trapezoid. The width and profile of the fragment peaks of $Ag_2^-$ show a clear dependence on precursor ion. In

addition to this difference, the peak associated with $AgBr^-$ ions at m/z 186 is also sharp and has a triangular profile, as shown in Fig. 4.3.6 (a). Such triangular profile is typical of the fragment peaks observed in CID of the ions and reflects the dissociation from the excited species with a wide range of internal energy. The trapezoidal profile, on the other hand, is characteristic of the dissociation process from the state with a specific internal energy as is the case for the dissociation of the neutralized methanol, in which the excited methanol dissociates along a purely repulsive potential curve [39, 49].

From the width at half maximum and the correction for the main beam width, I evaluated the kinetic energy release (KER) values for the ions $AgBr^-$ and $Ag_2^-$ derived from $Ag_2Br^+$ as 0.12 and 0.73 eV, respectively. The KER value for $Ag_2^-$ derived from $Ag_3^+$ is evaluated as 0.07 eV. These KER values correspond to the total kinetic energy released in the center of mass frame in the dissociation process of the excited cluster $Ag_2Br^*$. Using the thermochemical data shown in Figs. 4.3.2 and 4.3.4, the energies available for the dissociation of Br or Ag from $Ag_2Br^*$ are 1.4 and 2.49 eV, respectively and that of Ag from $Ag_3^*$ is 0.41 eV. It is interesting to know that the KER value for the elimination of Br is much larger than that of Ag, though the corresponding available energy of Br loss is smaller than that of Ag loss.

The fraction of the KER values to the corresponding available energies for the elimination of Ag and Br from $Ag_2Br^*$ are 5 and 52%, respectively. Efficiency for the internal to kinetic energy conversion is usually less than 15% for the elimination of atoms or small molecules [60]. While the fraction for Ag loss from $Ag_2Br^*$ is in the right range of efficiency, that for Br loss is much larger than the efficiency expected. In the case of Ag loss from $Ag_3^*$ a theoretical value for the fraction is 22% and experimental one is 5%. The fraction obtained using the theoretical value is larger than the fraction often found experimentally. The large available energy due to the low dissociation energy barrier presumed can explains this larger fraction for the dissociation of $Ag_3^*$ into $Ag_2$ + Ag. Regarding the large fraction of 52% for the elimination of Br from $Ag_2Br$, the structure of $Ag_2Br^+$ is discussed below. The structures of $Ag_2Br^*$ and $Ag_3^*$ formed by the near resonant neutralization are considered to remain the same as those of the respective positive ions, since the neutralization is a Franck-Condon process. The structure of $Ag_2Br^+$ in the ground state is reported by Rabillioud to be an isosceles triangle ($AgBrAg^+$) whose apex angle is 111 degrees [36, 37]. Since the loss of Ag from the isosceles triangular cluster $AgBrAg^*$ is expected to

provide significant vibrational and rotational excitation in the $Ag_2$ fragment due to the large structural difference in the $AgBrAg^+$ ion and the ground state $Ag_2$. A value of 5% obtained for the KER fraction is reasonable. However, the large fraction of 52% in the elimination of Br cannot be explained from the isosceles triangular cluster $AgBrAg^*$ due to the larger structure difference than that of the Ag elimination. The available energies evaluated from the thermochemical data shown in Fig. 4.3.2 are based on the formation of $Ag_2$ molecule and Br atom in their ground states. When the $Ag_2$ molecule is in an excited state, the available energy for the dissociation will decrease. The distance of Ag-Ag in the triangular ion $AgBrAg^+$, reported by Rabilloud *et al.* [36, 37] is evaluated to be $3.86 \times 10^{-10}$ m from the Ag-Br bond length of $2.54 \times 10^{-10}$ m and the apex angle of 111 degrees. When I employ a Morse potential with $D_e = 1.67$ eV and $r_e = 2.48 \times 10^{-10}$ m [61], the bond length of $3.86 \times 10^{-10}$ m of the $Ag_2$ molecule corresponds to a potential energy higher than the vibrational ground state of $Ag_2$ by 1.28 eV. If this excitation energy of the fragment $Ag_2$ molecule is used to estimate the available energy, it becomes almost zero and, hence, the observed large KER value of 0.73 eV for the elimination of Br is too large to be explained by a reaction mechanism via precursor ion $AgBrAg^+$ in the lowest state. From the large KER value for the loss of Br, therefore, it is suggested that the precursor ion $Ag_2Br^+$ does not assume an isosceles triangular form but a scalene one of the type of $AgAgBr^+$, though the latter structure has not been confirmed by theoretical calculations. The excited neutral cluster $AgAgBr^*$ thus formed retains the same structure as that of $AgAgBr^+$ and is expected to provide a large KER value due to a single bond cleavage of AgAg-Br leading to the production of $Ag_2$ and Br.

In this section, it was demonstrated that dissociation of singly charged silver bromide cluster and silver cluster induced by collision with the alkali metal target could be investigated. In the next section, dissociation of doubly charged tungsten hexacarbonyl induced by collision with an alkali metal target is investigated.

## References


[1] J. Yoon, K.S. Kim, K.K. Baeck, J. Chem. Phys. 112 (2000) 9335, and references therein.

[2] S.W. Buckner, J.R. Gord, B.S. Freiser, J. Chem. Phys. 88 (1988) 3678.

[3] J. Ho, K.M. Ervin, W.C. Lineberger, J. Chem. Phys. 93 (1990) 6987.

[4] C. Jackschath, I. Rabin, W. Schulze, Z. Phys. D 22 (1992) 517.

[5] H. Handschuh, C.-Y. Cha, P.S. Bechthold, G. Gantefor, W. Eberhardt, J. Chem. Phys. 102 (1995) 6406.

[6] V.A. Spasov, T.H. Lee, J.P. Maberry, K.M. Ervin, J. Chem. Phys. 110 (1999) 5208.

[7] S. Krückeberg, G. Dietrich, K. Lützenkirchen, L. Schweikhard, C. Walther, J. Ziegler, Int. J. Mass Spectom. Ion Process. 155 (1996) 141.

[8] A. Fielicke, I. Rabin, G. Meijer, J. Phys. Chem. A 110 (2006) 8060.

[9] S.P. Walch, C.W. Bauschlicher, S.R. Langhoff, J. Chem. Phys. 85 (1986) 5900.

[10] S.P. Walch, J. Chem. Phys. 87 (1987) 6776.

[11] C.W. Bauschlicher, S.R. Langhoff, H. Partridge, J. Chem. Phys. 91 (1989) 2412.

[12] K. Balasubramanian, P.Y. Feng, Chem. Phys. Lett. 159 (1989) 452.

[13] H. Partridge, C.W. Bauschlicher, S.R. Langhoff, Chem. Phys. Lett. 175 (1990) 531.

[14] V. Bonacic-Koutecky, L. Cespiva, P. Fantucci, J. Koutecky, J. Chem. Phys. 98 (1993) 7981.

[15] V. Bonacic-Koutecky, L. Cespiva, P. Fantucci, J. Pittner, J. Koutecky, J. Chem. Phys. 100 (1994) 490.

[16] R. Santamaria, I.G. Kaplan, O. Novaro, Chem. Phys. Lett. 218 (1994) 395.

[17] M.N. Huda, A.K. Ray, Eur. Phys. J. D 22 (2003) 217.

[18] Y. Wang, X.G. Gong, Eur. Phys. J. D 34 (2005) 19.

[19] a) D.P. de Bruijn, J. Neuteboom, V. Sidis, J. Los, Chem. Phys. 85 (1984) 215, b) D.P. de Bruijn, J. Neuteboom, J. Los, Chem. Phys. 85 (1984) 233.

[20] J.C. Brenot, H. Dunet, J.A. Fayeton, M. Barat, M. Winter, Phys. Rev. Lett. 77 (1996) 1246.

[21] M. Barat, J.C. Brenot, H. Dunet, J.A. Fayeton, Y.J. Picard, Eur. Phys. J. D 1 (1998) 271.

[22] J.A. Fayeton, M. Barat, J.C. Brenot, H. Dunet, Y.J. Picard, U. Saalmann, R. Schmidt, Phys. Rev. A 57 (1998) 1058.

[23] M. Barat, J.C. Brenot, H. Dunet, J.A. Fayeton, Y.J. Picard, J. Chem. Phys. 110 (1999) 10758.

[24] M. Barat, J.C. Brenot, H. Dunet, J.A. Fayeton, Y.J. Picard, D. Babikov, M. Sizun, Chem. Phys. Lett. 306 (1999) 233.

[25] S. Hayakawa, Int. J. Mass Spectrom. Ion Process. 90 (1989) 251.

[26] S. Wolf, G. Sommerer, S. Rutz, E. Schreiber, T. Leisner, L. Woste, R.S. Berry, Phys. Rev. Lett. 74 (1995) 4177.

[27] D.W. Boo, Y. Ozaki, L.H. Andersen, W.C. Lineberger, J. Phys. Chem. A 101 (1997) 6688.

[28] T. Leisner, S. Vajda, S. Wolf, L. Woste, R.S. Berry, J. Chem. Phys. 111 (1999) 1017.

[29] H.O. Jeschke, M.E. Garcia, K.H. Bennemann, J. Phys. B. Atom. Molec. Opt. Phys. 29 (1996) 545.

[30] H.O. Jeschke, M.E. Garcia, K.H. Bennemann, Phys. Rev. A 54 (1996) 4601.

[31] M. Hartmann, J. Pittner, V. Bonacic-Koutecky, A. Heidenreich, J. Jortner, J. Chem. Phys. 108 (1998) 3096.

[32] M. Hartmann, A. Heidenreich, J. Pittner, V. Bonacic-Koutecky, J. Jortner, J. Phys. Chem. A 102 (1998) 4069.

[33] I. Andrianov, V. Bonacic-Koutecky, M. Hartmann, J. Manz, J. Pittner, K. Sundermann, Chem. Phys. Lett. 318 (2000) 256.

[34] J.M. L'Hermite, F. Rabilloud, L. Marcou, P. Labastie, Eur. Phys. J. D 14 (2001) 323.

[35] J.M. L'Hermite, F. Rabilloud, P. Labastie, F. Spiegelman, Eur. Phys. J. D 16 (2001) 77.

[36] F. Rabilloud, F. Spiegelmann, J.L. Heully, J. Chem. Phys. 111 (1999) 8925.

[37] F. Rabilloud, F. Spiegelman, J.M. L'Hermite, P. Labastie, J. Chem. Phys. 114 (2001) 289.

[38] S. Hayakawa, K. Harada, K. Arakawa, N. Morishita, J. Chem. Phys. 112 (2000) 8432.

[39] S. Hayakawa, Int. J. Mass Spectrom. 212 (2001) 229..

[40] R.G. Cooks, in *Collision Spectroscopy*, Chapt.7, edited by R.G. Cooks, Prenum, New York, 1978.

[41] S. Hayakawa, H. Endoh, K. Arakawa, N. Morishita, T. Sugiura, Int. J. Mass

Spectrom. Ion Process. 151 (1995) 89.

[42] S. Hayakawa, J. Mass Spectrom. 39 (2004) 111.

[43] S. Hayakawa, A. Kitaguchi, S. Kameoka, M. Toyoda, T. Ichihara, J. Chem. Phys. 124 (2006) 224320.

[44] P. Sharpe, C.J. Cassady, Chem. Phys. Lett. 191 (1992) 111.

[45] V.H. Wysocki, H.I. Kenttamaa, R.G. Cooks, Int. J. Mass Spectrom. Ion Process. 75 (1987) 181.

[46] K.L. Schey, H.I. Kenttämaa, V.H. Wysocki, R. Graham Cooks, Int. J. Mass Spectom. Ion Process. 90 (1989) 71.

[47] V.H. Wysocki, H.I. Kenttamaa, R.G. Cooks, J. Phys. Chem. 92 (1988) 6465.

[48] S.R. Horning, M. Vincenti, R.G. Cooks, J. Am. Chem. Soc. 112 (1990) 119.

[49] S. Hayakawa, K. Harada, N. Watanabe, K. Arakawa, N. Morishita, Int. J. Mass Spectrom. 202 (2000) A1.

[50] S. Hayakawa, K. Kadomura, M. Kimura, C.M. Dutta, Phys. Rev. A 70 (2004) 022708.

[51] S. Hayakawa, N. Terazawa, T. Sugiura, J. Phys. B 23 (1990) 4539.

[52] S. Hayakawa, N. Terazawa, T. Sugiura, J. Mass Spectrom. Soc. Jpn. 41 (1993) 225.

[53] S. Hayakawa, M. Takahashi, K. Arakawa, N. Morishita, J. Chem. Phys. 110 (1999) 2745.

[54] S. Hayakawa, K. Tomozawa, T. Takeuchi, K. Arakawa, N. Morishita, Phys. Chem. Chem. Phys. 5 (2003) 2386.

[55] S. Hayakawa, N. Kabuki, Eur. Phys. J. D 38 (2006) 163.

[56] S. Hayakawa, M. Hashimoto, H. Matsubara, F. Turecek, J. Am. Chem. Soc. 129, (2007) 7936.

[57] S. Hayakawa, K. Taguchi, R. Kotani, K. Arakawa, N. Morishita, J. Mass Spectrom. Soc. Jpn. 49, 219 (2001).

[58] S. Hayakawa, H. Matsubara, Y. Kawamura, K. Iwamoto, Int. J. Mass Spectrom. 262, (2007) 220.

[59] S. Hayakawa, Y. Kawamura, Y. Takahashi, Int. J. Mass Spectrom. 246 (2005) 56.

[60] R.G. Cooks, J.H. Beynon, R.M. Caprioli, G.R. Lester, *Metastable Ions*, Elsevier, Amsterdam, 1973.

[61] K.P. Huber, G. Herzberg, *Molecular Spectra and Molecular Structure IV.*

*Constants of Diatomic Molecules*, Van Nostrand Reinhold, New York, 1979.

## 4.4 High-energy ETD of doubly charged tungsten hexacarbonyl $W(CO)_6^{2+}$ ions using alkali metal targets

### 4.4.1 Introduction

In this section, dissociation of doubly charged tungsten hexacarbonyl induced by collision with alkali metal targets is investigated.

Since the development of ESI [1], there has been a growing interest in electron capture and electron transfer processes of multiply charged ions formed from large biomolecules as ECD [2-5] or ETD [6, 7]. These processes have been studied to obtain information about the dissociation of molecular projectile ions, particularly amino acid sequences in peptides and proteins. The usefulness of the electron capture and electron transfer process is associated with N-Cα bond cleavages to form *c*- and *z*-type ions [8, 9] without the loss of labile posttranslational modification groups. [2-7] The mechanism of N-Cα bond cleavage reactions has been studied by Turecek and coworkers [10-13]. N-Cα bond cleavages induced by electron transfer processes of multiply charge peptides on collision with neutral targets, such as alkali metals [14, 15], or metastable rare gases [16] have also been reported. Because the dissociation behavior of isolated molecules is controlled by the internal energy distribution $P(e)$ of the molecular population, it is of fundamental importance to be able to characterize this distribution for charged ions whose charge is reduced by electron transfer. The current interest in ECD and ETD of multiply charged ions of large biomolecules also makes it important to develop methods for characterizing their internal energy distributions. Theoretical calculations to estimate the internal energy and the cross section are virtually impossible for electron transfer processes involving multiply charged ions of large biomolecules, because of the multitude of ion structures and dissociation pathways involved.

Beynon and coworkers [17-19] reported an approximate thermometer method in which branching ratios were used to characterize energy deposition associated with photodissociation. Wysocki *et al.* [20] have reported the use of so-called thermometer molecules to measure internal energy distributions $P(e)$ of gas-phase ions. By using the same method, Cooks and coworkers determined the internal energy distributions, $P(e)$, in doubly charged ions following electron transfer in high-energy collisions by using a sector-type mass spectrometer and in low-energy collisions by using a triple quadrupole mass spectrometer with various atomic and molecular targets [21-23]. One of the

authors have previously measured the internal energy distribution of neutral species formed through neutralization in charge inversion mass spectrometry with alkali metal targets by using the thermometer molecule $W(CO)_6$ [24]. The internal energy distributions in the charge-inversion mass spectrometry indicated that dissociation occurs in the energy-selected neutral species formed by way of near-resonant neutralization [24-26]. I recently reported differences between the internal energy depositions induced by collisional activation and by electron transfer of $W(CO)_6^{2+}$ ions on collision with Ar and K targets [27]. The internal energy deposition in CID evaluated with the Ar target was broad and decreased with increasing internal energy. On the contrary to this, internal energy deposition evaluated with the K target was very narrow and centered at a particular energy, 7.8 eV below the energy level of the $W(CO)_6^{2+}$ ion. This narrow internal energy distribution was explained in terms of electron transfer by Landau-Zener [28-30] potential crossing at a separation of $5.9 \times 10^{-8}$ cm between a $W(CO)_6^{2+}$ ion and a K atom, and the coulombic repulsion between singly charged ions in the exit channel. These results were compared with a classical overbarrier model [31, 32], that successfully explained processes involving electron capture by multiply charged atomic ions in collision with atoms or simple molecules. From these experimental results, I proposed that the terms "CID" and "CAD", which were similarly defined [33], should not be used interchangeably, on the basis that there are differences in the observed ions and in their intensities with Ar and K targets.

In the present work, I measured the CID spectra of doubly charged $W(CO)_6^{2+}$ ions following collision with either an K target or a Cs target. While the internal energy distributions obtained with both the K and Cs targets were very narrow, the average internal energy with a K target was lower than that with a Cs target. From the similarities and differences between the K and Cs target, I concluded that electron transfer from the alkali metal proceeds through a potential crossing at a large internuclear distance and that polarizability of the target is an important factor determining the position of the potential crossing.

### 4.4.2 Experimental section

Mass-selected doubly charged ions were made to collide with alkali metal targets, and the resulting singly and doubly charged ions that formed upon electron transfer and collisional activation were mass analyzed by using an MS/MS instrument [27]. Doubly

charged $W(CO)_6^{2+}$ ions were formed by 70 eV electron ionization and accelerated to a kinetic energy of 10 keV by an accelerating voltage of 5 kV. Tungsten hexacarbonyl [W(CO)6; 99%, Aldrich, USA]] was used as received. CID spectra were measured by mass-analyzing the singly and doubly charged positive ions leaving the collision cell by scanning the electric field in MS-2 from 0 to twice the electric field that causes the primary doubly charged ions to pass through the MS-2.

### 4.4.3 Results and Discussion

The CID spectra of the doubly charged tungsten hexacarbonyl cation $W(CO)_6^{2+}$ with K and Cs as the targets are shown in Fig. 4.4.1(a) and 1(b).

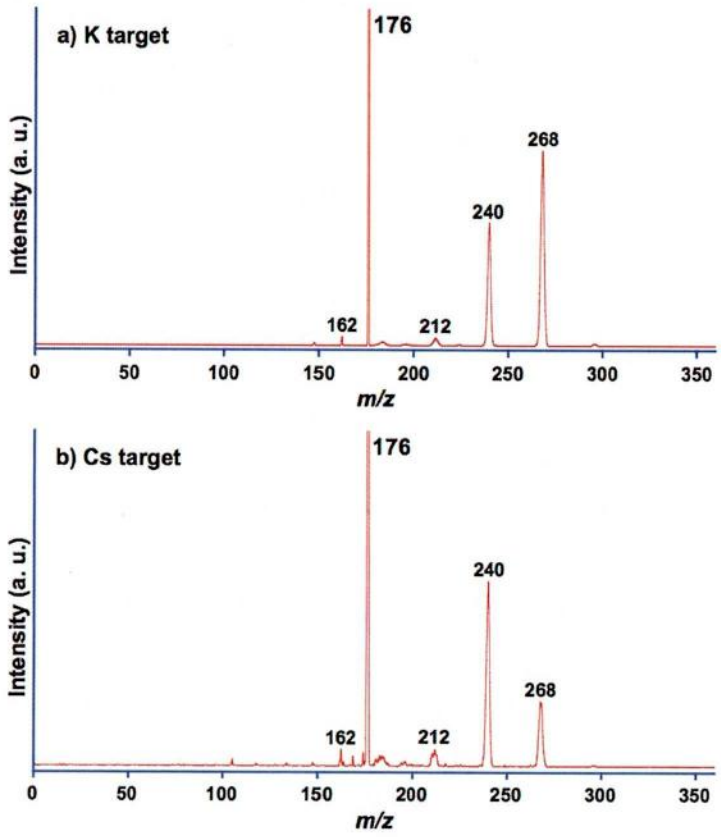


**Fig. 4.4.1.** Collision-induced dissociation (CID) spectra of the doubly charged tungsten hexacarbonyl cation [$W(CO)_6^{2+}$] with K and Cs as targets. The target gas is K for (a) and Cs for (b). The scales on the vertical axes of the spectra in (a) and (b) are normalized at the intensities of the strongest fragment peaks in the respective spectra, which are associated with the $W(CO)_3^+$ ions and $W(CO)_2^+$ ions, respectively.

Singly charged fragment ions were formed by electron transfer followed by dissociation, and doubly charged fragment ions were formed by collisional activation (CA), as shown in the reference [27]. In the both CID spectra, the non-dissociated $W(CO)_6^{2+}$ peak at *m/z* = 176 is by far the strongest, with a height higher than the upper limit of the scale of the vertical axis. The high intensity of this $W(CO)_6^{2+}$ peak was attributed to a precursor ion that did not interact with the target. In the CID spectrum with both K [Fig. 4.4.1(a)] and Cs [Fig. 4.4.1(b)] targets, the predominant peaks at *m/z* = 240 and 268 are associated with singly charged $W(CO)_2^+$ and $W(CO)_3^+$ ions, respectively. The singly charged fragment $W(CO)_2^+$ and $W(CO)_3^+$ ions result from electron transfer followed by a loss of four and three CO ligands, respectively. The relative abundances of these two peaks are much different between the K and Cs targets. The relative abundance of the peak associated with $W(CO)_2^+$ ions compared with that for $W(CO)_3^+$ ions is 1.0:1.66 with K target in Fig. 4.4.1(a) and 1.0:0.49 with the Cs target in Fig. 4.4.1(b). The relative abundances associated with $W(CO)^+$ (*m/z* = 212) and $W(CO)_2^+$ (*m/z* = 240) ions in the Cs target [Fig. 4.4.1 (b)] are higher than those in the K target [Fig. 4.4.1(a)]. The higher intensity of the lower mass ions with the Cs target than that with the K target indicates that the internal energy of the charge-reduced $W(CO)_6^{+*}$ ions obtained on collisions with the Cs target was higher than that with the K target. The very weak peaks associated with doubly charged $W(CO)_m^{2+}$ ($m$ = 4,5) ions resulting from cleavage of the W—CO bonds are observed at *m/z* = 148 and 162 in both spectra of Fig. 4.4.1. The relative abundances of $W(CO)_n^{2+}$ ($n$ = 4,5) and $W(CO)_n^+$ ($n$ = 1–6) obtained from the CID spectra following collisions with K and Cs targets are shown in Table 4.4.1; the relative abundances are evaluated from the average of several CID spectra measured atdifferent target pressures under the single-collision conditions. The peak intensities of the doubly charged fragment ions are much lower than those associated with singly charged $W(CO)_m^+$ ($m$ = 2, 3) ions. The excessive intensity difference between the singly charged ions and doubly charged ions indicated that the electron transfer process was much effective than CA in the case of collisions with alkali metal targets. This result is explained by the fact that the difference in the cross section of the electron transfer of doubly charged ions on collision with the alkali metal targets, which is of the order of $10^{-14}$ $cm^2$ is much larger than that of CA, which is of the order of $10^{-16}$ $cm^2$ [27].

The method to evaluate the internal energy distribution *P(e)* was reported by Wysocki *et al.* [20] by using the peak abundances in the spectra and the thermochemical

**Table 4.4.1.** The relative abundances of $W(CO)_n^{2+}$ ($n$ = 1–5) and $W(CO)_m^{+}$ ($m$ = 1–6) obtained from the CID spectra. The abundances are normalized to that of the largest fragment peak associated with the $W(CO)_3^{+}$ and $W(CO)_2^{+}$ ions with K and Cs targets, respectively. The relative abundances are evaluated from the average of the several mass spectra measured in different target pressures under the single-collision conditions. Intensities lower than 1% are shown as "—"

| Singly charged ions | | | Doubly charged ions | | |
|---|---|---|---|---|---|
| | *Target* | | | *Target* | |
| Ion | *K* | *Cs* | Ion | *K* | *Cs* |
| $W(CO)_6^{+}$ | — | — | $W(CO)_6^{2+}$ | | |
| $W(CO)_5^{+}$ | — | — | $W(CO)_5^{2+}$ | 3 | 4 |
| $W(CO)_4^{+}$ | 2 | — | $W(CO)_4^{2+}$ | 1 | — |
| $W(CO)_3^{+}$ | 100 | 36 | $W(CO)_3^{2+}$ | — | — |
| $W(CO)_2^{+}$ | 63 | 100 | $W(CO)_2^{2+}$ | — | — |

**Table 4.4.2.** Thermochemical data for $W(CO)_6^{+}$, $W(CO)_6^{2+}$, and their fragment ions. *IE/AE* are the ionization energies or appearance energies and *BE* are the bond energies. D*E* are energy differences from the energy level of the charge reduced $W(CO)_6^{+}$ ion. All values are in eV. *IE/AE* values for singly charged ions are taken from Wysocki *et al.* [20] *IE/AE* values for doubly charged ions are taken from Cooks *et al.* [21]

| Singly charged ions | | | | Doubly charged ions | | | |
|---|---|---|---|---|---|---|---|
| Ion | *IE/AE* | *BE* | *ΔE* | Ion | *IE/AE* | *BE* | *ΔE* |
| $W(CO)_6^{+}$ | 8. 5 | | 0.0 | $W(CO)_6^{2+}$ | 23. 5 | | 15.0 |
| $W(CO)_5^{+}$ | 9. 7 | 1. 2 | 1.2 | $W(CO)_5^{2+}$ | 24. 5 | 1. 0 | 16.0 |
| $W(CO)_4^{+}$ | 11. 9 | 2. 2 | 3.4 | $W(CO)_4^{2+}$ | 27. 3 | 2. 8 | 18.8 |
| $W(CO)_3^{+}$ | 13. 7 | 1. 8 | 5.2 | $W(CO)_3^{2+}$ | 29. 7 | 2. 4 | 21.2 |
| $W(CO)_2^{+}$ | 16. 0 | 2. 3 | 7.5 | $W(CO)_2^{2+}$ | 32. 0 | 2. 3 | 23.5 |
| $W(CO)^{+}$ | 18. 6 | 2. 6 | 10.1 | $W(CO)^{2+}$ | 35. 7 | 3. 7 | 27.2 |
| $W^{+}$ | 21. 5 | 2. 9 | 13.0 | $W^{2+}$ | 38. 6 | 2. 9 | 30.1 |

data. The thermochemical data for $W(CO)_6^+$, $W(CO)_6^{2+}$, and their fragment ions are listed in Table 4.4.2. The thermochemical data of *IE/AE* values for singly charged ions and for doubly charged ions are reported by Wysocki *et al.* and Cooks *et* al., which were obtained from the measured ionization energy of the $W(CO)_6^+$ ion and the appearance energies of the fragment ions [20, 21]. This method assumed that all the ions that have enough internal energy to dissociate do so and that they undergo the most endothermic reaction open to them. All the charge reduced $W(CO)_6^{+*}$ ions with energies between the activation energies for formation of $W(CO)_m^+$ ions and $W(CO)_{m-1}^+$ ions [DE($m$) and DE($m$–1), respectively] are assumed to fragment to yield $W(CO)_m^+$ ions. The relative abundance of each fragment $W(CO)_m^+$ ion is taken as a measure of the number of charge reduced $W(CO)_6^{+*}$ ions with internal energies between DE($m$) and DE($m$–1). The abundances of fragment $W(CO)_m^+$ ions divided by the energy range DE($m$–1) – DE($m$) gives the data height in *P(e)* between DE($m$) and DE($m$–1), which allow a comparison to be made between the relative abundances in *P(e)* and those in the CID spectra. To apply the method in the present work, some other additional assumptions are necessary, including the following: (1) a low initial energy of the parent $W(CO)_6^{2+}$ ions; (2) a low translational energy in the center of mass system of fragments after dissociation; (3) a low internal energy in fragment CO molecules; and (4) the short dissociation lifetimes of $W(CO)_m^+$ ions. These assumptions (1)–(4) were rationalized in the previous report [27].

Figures 4.4.2(a) and 4.4.2(b) show the internal energy distributions, *P(e)*, obtained from the relative abundances tabulated in Table 4.4.1 evaluated from the CID spectra with the K and Cs targets and by using the thermochemical data tabulated in Table 4.4.2, by using the same method as that reported by Wysocki *et al.* [20]. The internal energies are scaled from the energy level of the charge reduced $W(CO)_6^+$ ion. In Fig. 4.4.2 (a) and (b), the *P(e)* values between 5.2 and 7.5 eV correspond to the abundances of the peaks associated with the $W(CO)_3^+$ ion in Fig. 4.4.1 (a) and (b), whereas those between 7.5 and 10.1 eV correspond to those associated with the $W(CO)_2^+$ ion. The peak associated with the precursor $W(CO)_6^{2+}$ ion contains the contributions that did not interact with the target, and the relative intensity of this peak relative to those of the fragment ions depends on the target density. Therefore, the value between 15.0 and 16.0 eV that corresponds to the intensity of the precursor $W(CO)_6^{2+}$ ion is not plotted. The values that correspond to the intensities of the atomic singly

charged $W^+$ ions are not plotted, because the upper limits of the internal energies are not determined for atomic ions.

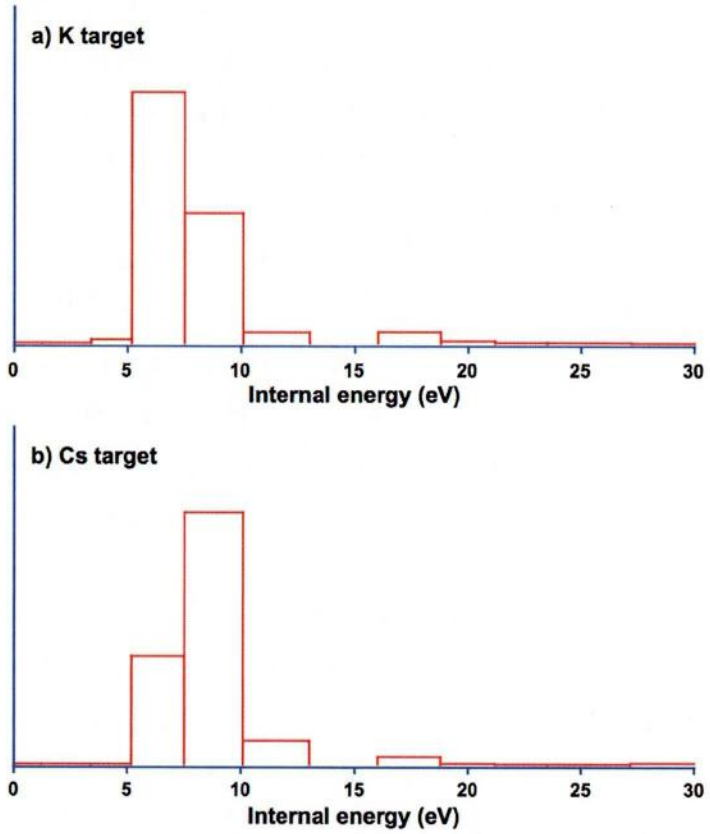


**Fig. 4.4.2.** Internal energy distributions, $P(\varepsilon)$, obtained from the relative abundances listed in Table 4.4.1 and evaluated from the CID spectra with the K (a) and Cs (b) targets and calculated by using the thermochemical data reported by Wysocki *et al.* [3] and from Cooks *et al.* [4]. The scales on the vertical axes of $P(\varepsilon)$ distributions for the K (a) and Cs targets (b) are normalized at the height of the strongest fragments in the respective spectra, which are associated with $W(CO)_3^+$ ions and $W(CO)_2^+$ ions, respectively.

As Fig. 4.4.2 show the relative abundances, the plots for the K target in Fig. 4.4.2(a) and for the Cs target in Fig. 4.4.2 (b) are normalized at the largest $P(e)$ value between 5.2 and 7.5 eV and to that between 7.5 and 10.1 eV, respectively. The intensity of the singly charged ions formed by electron transfer is much larger than that in the positive region of the doubly charged fragment ions formed from collisional activation for both K and Cs target. This intensity difference indicates that the relative

cross section for electron transfer is much larger than that for collisional activation with alkali metal targets. The presence of the narrow maximum peak in the internal energy distribution for the singly charged ions formed by electron transfer from the K and Cs targets shows that a specific excitation for the singly charged $W(CO)_6^{+*}$ formed by the electron transfer predominates in the case of alkali metal targets, as is the case in charge-inversion mass spectrometry [24-26].

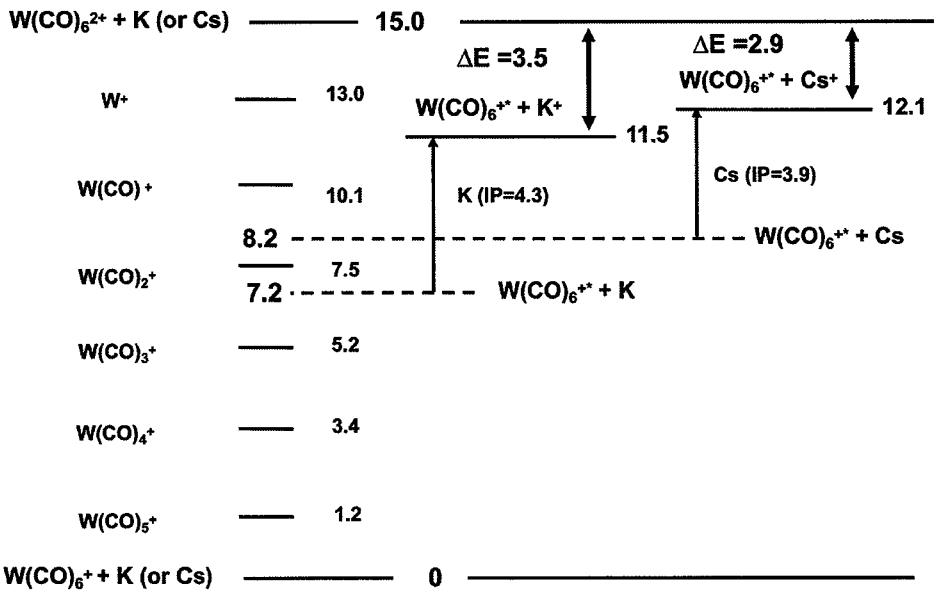


**Fig. 4.4.3.** Energy levels of $W(CO)_6^+$, $W(CO)_6^{2+}$, and their fragment ions in electron volts. The thermochemical data are from Wysocki *et al.* [3] and from Cooks *et al.* [4]. The average values of the internal energy of $W(CO)_6^{+*}$ were evaluated from the data shown in Fig. 4.4.2. For the sake of clarity, + K and + Cs ions are omitted from the energy levels of the fragments.

The internal energy distribution for the Cs target is higher than that for the K target, as shown in Fig. 4.4.2. The average internal energy for the K target, evaluated from the relative abundances of the $W(CO)_2^+$ ion and the $W(CO)_3^+$ ion, is 7.2 eV. As the fragment ions with the maximum intensity were $W(CO)_2^+$ ions in the case of the Cs target, the average value of the internal energy for the Cs target was evaluated to be 8.2 eV from the abundances of $W(CO)^+$ to $W(CO)_3^+$ ions. The lower values of the average internal energy for both targets than the energy level of 15 eV for the precursor

$W(CO)_6^{2+}$ ion indicated that the electron transfer on collision with alkali metal targets provided the charge reduced $W(CO)_6^{+*}$ whose energy was lower than the precursor $W(CO)_6^{2+}$ ion. The internal energy distributions for the K target, in which the energies were scaled from the energy level of the precursor $W(CO)_6^{2+}$ ion, was already shown in the previous report [27]. The average internal energy of 7.2 eV scaled from the energy level of the charge reduced $W(CO)_6^{+}$ ion is identical to that of -7.8 eV scaled from the energy level of the precursor $W(CO)_6^{2+}$ ion.

Energy levels of $W(CO)_6^{+}$, $W(CO)_6^{2+}$, and their fragment ions are shown in Fig. 4.4.3. The energy values of the fragments are scaled from the ground state of the charge reduced $W(CO)_6^{+}$ and a neutral alkali metal, whose energy is 15 eV lower than the entrance channel of the collision. The average energy level of $W(CO)_6^{+*}$ ions for K and Cs targets estimated from the internal energy distribution for the electron transfer process in Fig. 4.4.2 are 7.2 and 8.2 eV, respectively. The energy level of 7.2 (or 8.2) eV corresponds to an energy level of the $W(CO)_6^{+*}$ + K (or Cs) reaction. The energy level of the exit channel of $W(CO)_6^{+*}$ + $K^+$ (or $Cs^+$) in the reaction of the present work is higher than that of $W(CO)_6^{+*}$ + K (or Cs) by an amount equal to the ionization energy of the respective target. Since the ionization energies of K and Cs are 4.34 and 3.89 eV, respectively, the energy differences of 3.5 and 2.9 eV are evaluated to be those between the entrance channel of $W(CO)_6^{2+}$ + K (or Cs) and the exit channel of $W(CO)_6^{+*}$ + $K^+$ (or $Cs^+$). While the electron transfer process between singly charged ions and an alkali metal target was near-resonant as demonstrated by our group [24-26], the energy differences of 3.5 and 2.9 eV indicated that the electron transfer between the doubly charged ions and the alkali metal targets were not near-resonant process. These differences have been explained in terms of an ion induced dipole in the entrance channel and a coulomic repulsion in the exit channel as discussed in the previous study. [27] The process most likely to be responsible for electron transfer is Landau-Zener curve crossing [28-30], which is represented schematically in Fig. 4.4.4. In this model, the doubly charged ion and the target gas approach each other along an ion-induced dipole curve; at some critical distance ($R_c$), electron transfer takes place and the two singly charged positive ions exit on a coulombic repulsion curve. The energy difference (DE) of this process between the entrance and the exit channels is calculated by using equation (4-4-1),

$$\Delta E = \frac{e^2}{4\pi\varepsilon_0 R_c} + \frac{\alpha(2e)^2}{32\pi^2\varepsilon_0^2 R_c^4} \qquad (4\text{-}4\text{-}1)$$

where e is the electric charge, $e_o$ is the permittivity of a vacuum, and a represents the polarizability of the target. The Landau-Zener curve crossing near the critical distance of the electron transfer is represented schematically in Fig. 4.4.4. The energy levels of the entrance channel decrease with decreasing the internuclear distance, because of the large polarizabilities for the K and Cs targets, whose values are $43.4 \times 10^{-30}$ and $59.6 \times 10^{-30}$ $m^3$, [34, 35] respectively.

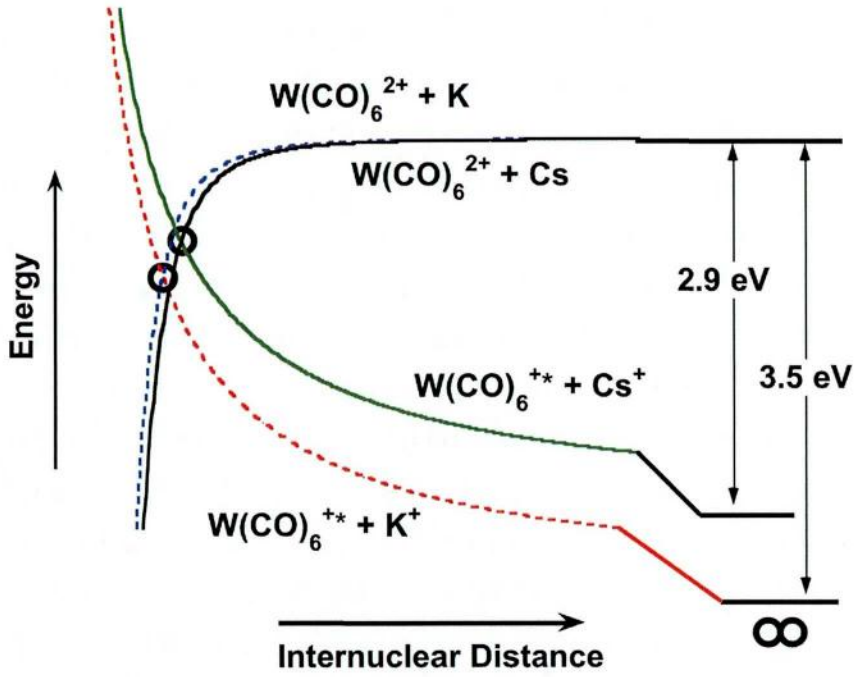


**Fig. 4.4.4.** Schematic of the potential energy curves near the critical distance of Landau-Zener [8-10] potential crossing. The ○ symbols indicate positions of potential crossing of the respective targets.

Based on the energy difference between the entrance and exit channels evaluated from the maximum in the internal-energy distribution, an critical distances of the electron transfer of $W(CO)_6^{2+}$ and K and Cs targets are evaluated to be $5.88 \times 10^{-8}$ and $6.83 \times 10^{-8}$ cm, respectively. This potential crossing at this large internuclear distance meets the criterion for electron transfer by the Landau-Zener curve crossing. The decrease in the energy as a result of the ion-induced dipole in the entrance channel at the critical

points from the infinite internuclear distance are 1.05 eV for the K target and 0.79 eV for the Cs target. The ratio between the decreases in the energy and the energy differences between the entrance and the exit channel for the K and the Cs targets are 30 and 27%, respectively. If these decreases are neglected, the critical distances for the K and Cs targets become $4.11 \times 10^{-8}$ and $4.96 \times 10^{-8}$ cm, respectively. The decrease of more than 27% in the energy and the difference in the critical distances indicate that the decrease in the energy as a result of the ion-induced dipole cannot be neglected in evaluating the critical distance of electron transfer in case using alkali metal targets. The critical distances estimated in this work are longer than the internuclear distances of the alkali metal molecules $K_2$ and $Cs_2$ reported to be $3.91 \times 10^{-8}$ and $4.47\times 10^{-8}$ cm, respectively [36]. Electronic structures of the alkali metal molecules were well represented by two valence s electrons with well-separated inner cores [37]. Whereas the ratio of the estimated critical distances between K and Cs is 0.86, the ratio of the internuclear distances of the diatomic molecules is 0.87. The larger values of the critical distance compared with the internuclear distances of the molecules and the similarity of their ratios suggests that electron transfer between doubly charged ions and an alkali metal target takes place from the outmost s orbital.

While the cross section estimated on the basis of an internuclear distance of $5.88 \times 10^{-8}$ cm for K target is $1.09 \times 10^{-14}$ $cm^2$, that of $6.83 \times 10^{-8}$ cm for Cs target is $1.47 \times 10^{-14}$ $cm^2$. The cross section of the order of $10^{-14}$ $cm^2$ estimated in the present work is much larger than that for collisional activation, which has been estimated to be in order of $10^{-16}$ $cm^2$ [27, 38]. I believe that the electron transfer processes of multiply charged ions of large biomolecules that follow collision with alkali metal targets will provide information about the dissociation of molecular projectile ions, particularly about amino-acid sequences in peptides and proteins, in the same manner as do the isomeric differentiations in charge-inversion mass spectrometry [27, 38-41].

In this section, it was demonstrated that dissociation of doubly charged tungsten hexacarbonyl induced by collision with an alkali metal target could be investigated. In the next section, dissociation of multiply protonated peptides induced by electron transfer from an alkali metal target is investigated.

## References


[1] J.B. Fenn, M. Mann, C.K. Meng, S.F. Wong, C.M. Whitehouse, Science 246 (1989) 64.

[2] R.A. Zubarev, N.L. Kelleher, F.W. McLafferty, J. Am. Chem. Soc. 120 (1998) 3265.

[3] R.A. Zubarev, N.A. Kruger, E.K. Fridriksson, M.A. Lewis, D.M. Horn, B.K. Carpenter, F.W. McLafferty, J. Am. Chem. Soc. 121 (1999) 2857.

[4] R.A. Zubarev, K.F. Haselmann, B. Budnik, F. Kjeldsen, F. Jensen, Eur. J. Mass Spectrom. 8 (2002) 337.

[5] R.A. Zubarev, Mass Spectrom. Rev. 22 (2003) 57.

[6] J.E.P. Syka, J.J. Coon, M.J. Schroeder, J. Shabanowitz, D.F. Hunt, Proc. Natl. Acad. Sci. U. S. A. 101 (2004) 9528.

[7] J.J. Coon, J.E.P. Syka, J.C. Schwartz, J. Shabanowitz, D.F. Hunt, Int. J. Mass Spectrom. 236 (2004) 33.

[8] P. Roepstorff, J. Fohlman, Biomed. Mass Spectrom. 11 (1984) 601.

[9] K. Biemann, Biomed. Environ. Mass Spectrom. 16 (1988) 99.

[10] F. Turecek, J. Am. Chem. Soc. 125 (2003) 5954.

[11] F. Turecek, E.A. Syrstad, J. Am. Chem. Soc. 125 (2003) 3353.

[12] E.A. Syrstad, F. Turecek, J. Am. Soc. Mass Spectrom. 16 (2005) 208.

[13] X.H. Chen, F. Turecek, J. Am. Chem. Soc. 128 (2006) 12520.

[14] P. Hvelplund, B. Liu, S.B. Nielsen, S. Tomita, Int. J. Mass Spectrom. 225 (2003) 83.

[15] T. Chakraborty, A.I.S. Holm, P. Hvelplund, S.B. Nielsen, J.C. Poully, E.S. Worm, E.R. Williams, J. Am. Soc. Mass Spectrom. 17 (2006) 1675.

[16] V.D. Berkout, Anal. Chem. 78 (2006) 3055.

[17] E.S. Mukhtar, Griffiths I.W., F.M. Harris, J.H. Beynon, Int. J. Mass Spectom. Ion Phys. 37 (1981) 159.

[18] I.W. Griffiths, E.S. Mukhtar, R.E. March, F.M. Harris, J.H. Beynon, Int. J. Mass Spectom. Ion Phys. 39 (1981) 125.

[19] I.W. Griffiths, E.S. Mukhtar, F.M. Harris, J.H. Beynon, Int. J. Mass Spectom. Ion Phys. 43 (1982) 283.

[20] V.H. Wysocki, H.I. Kenttamaa, R.G. Cooks, Int. J. Mass Spectom. Ion Process. 75 (1987) 181.

[21] R.G. Cooks, T. Ast, B. Kralj, V. Kramer, D. Zigon, J. Am. Soc. Mass Spectrom. 1 (1990) 16.

[22] L.E. Dejarme, R.G. Cooks, T. Ast, Org. Mass Spectrom. 27 (1992) 667.

[23] R. Susic, L. Lu, D.E. Riederer, D. Zigon, R.G. Cooks, T. Ast, Org. Mass Spectrom. 27 (1992) 769.

[24] S. Hayakawa, K. Harada, K. Arakawa, N. Morishita, J. Chem. Phys. 112 (2000) 8432.

[25] S. Hayakawa, K. Harada, N. Watanabe, K. Arakawa, N. Morishita, Int. J. Mass Spectrom. 202 (2000) A1.

[26] S. Hayakawa, Int. J. Mass Spectrom. 212 (2001) 229.

[27] S. Hayakawa, A. Kitaguchi, S. Kameoka, M. Toyoda, T. Ichihara, J. Chem. Phys. 124 (2006) 224320.

[28] L. Landau, Z. Phys. Sowiet 2 (1932) 46.

[29] E.C.G. Stuecklberg, Helv. Phys. Acta 5 (1932) 370.

[30] C. Zener, Proc. Roy. Soc. A 137 (1932) 696.

[31] H. Ryufuku, K. Sasaki, T. Watanabe, Phys. Rev. A 21 (1981) 745.

[32] A. Barany, G. Astner, H. Cederquist, H. Danared, S. Huldt, P. Hvelplund, A. Johnson, H. Knudsen, L. Liljeby, K.G. Rensfelt, Nucl. Instrum. Methods Phys. Res. B 9 (1985) 397.

[33] J.F.J. Todd, Int. J. Mass Spectom. Ion Process. 142 (1995) 209.

[34] T.M. Miller, B. Bederson, Adv. At. Mol. Phys. 13 (1977) 1.

[35] T.M. Miller, B. Bederson, Adv. At. Mol. Phys. 25 (1988) 37.

[36] K.P. Huber, G. Herzberg, *In Molecular Spectra and Molecular Structure IV. Constants of Diatomic Molecules*, Vol. IV, Van Nostrand Reinhold, New York, 1979.

[37] W. Muller, W. Meyer, J. Chem. Phys. 80 (1984) 3311.

[38] S. Hayakawa, J. Mass Spectrom. 39 (2004) 111.

[39] S. Hayakawa, Y. Kawamura, Y. Takahashi, Int. J. Mass Spectrom. 246 (2005) 56.

[40] S. Hayakawa, A. Kitaguchi, J. Mass Spectrom. 41 (2006) 1226.

[41] S. Hayakawa, N. Kabuki, Eur. Phys. J. D 38 (2006) 163.

## 4.5 High-energy ETD of doubly protonated peptides using the alkali metal target

### 4.5.1 Introduction

In section 4.4, it was demonstrated that the tandem sector mass spectrometer has a potential to obtain high-energy ETD spectra of the inorganic ions [1-3]. In this section, high-energy ETD is applied to multiply protonated peptides. However, the instrument has two problems for obtaining the high-energy ETD spectra of biological samples. The sensitivity of the instrument is insufficient to measure the biological samples since biological samples are valuable due to their micro amounts. This instrument requires extremely large amount of samples (10-100 nmol) for measurements. In addition, post-acceleration type detection system of this instrument, which consists of a conversion dynode and secondary electron multiplier, has a problem that fragment ions of low *m/z* were not detected. It is a serious problem to determine the amino acid sequence of peptides completely. Therefore it is necessary to improve the sensitivity and mass range of the instrument in order to measure the biological samples. In this section, the improvement of the ion transmission efficiency and mass range of this instrument, and high-energy ETD of biological samples are described [4]. After the improvement, high-energy ETD spectra of the polypeptides such as substance P, angiotensin II and bradykinin are obtained in order to investigate the dissociation efficiency, and demonstrate the usefulness in the structural analysis of high-energy ETD.

### 4.5.2 Experimental section

Doubly protonated peptides were formed by ESI and accelerated to a kinetic energy of 10 keV by an accelerating voltage of 5 kV. The precursor ions were mass-selected and collided with a Cs target. It is reported that the fragment pattern of the protonated peptides do not depend on the type of alkali metal targets [5]. However, the peak intensity of fragment ions is dependent on electron transfer efficiency of alkali metal targets. Therefore, the alkali metal target, which has higher electron transfer efficiency, gives the higher peak intensity of fragment ions. For this reason, Cs was used as alkali metal target in the experiments [3].

### 4.5.3 Results and Discussion

**Connection of MS-1 with MS-2 using electrostatic quadrupole lens doublet**

The reason for the poor sensitivity of the instrument is discussed in the beginning. In a JMS-HX110 double-focusing mass spectrometer (Fig. 3.1), the deviation of energy and direction of the accelerated ions are double-focused at the collector slit. That is, the deviation of energy and direction of the ions are not double-focused at the collision cell. Therefore, the ion transmission efficiency of the collision cell decreases. In order to improve the ion transmission efficiency, quadrupole doublet lens was equipped between a JMS-HX110 double-focusing mass spectrometer and the collision cell. A schematic diagram and photograph of the new experimental setup equipped with quadrupole doublet lens are shown in Fig. 4.5.1 and Fig. 4.5.2, respectively.

The position and applied voltage of the quadrupole doublet lens was simulated and optimized by using the ion trajectory program "TRIO2.0" [6]. Fig. 4.5.3 shows ion trajectories between the ion source and the collision cell simulated by TRIO 2.0, (a) with a Q lens doublet and (b) without the Q lens doublet. "E" and "M" in Fig. 4.5.3 indicates the electric field and magnetic field, respectively. Ion trajectories having different initial conditions are expressed by individual colors (green for position, blue for angle, red for energy). While these ion trajectories diverge at the collision cell with a Q lens doublet, the deviation of energy and direction of the ions were double-focused at the collision cell again without the Q lens doublet. As a result, the ion intensity in the case of (b) became about 10 times higher than that in the case of (a), when the experimental conditions were same (data not shown).

Fig. 4.5.4 show high-energy ETD spectra of a doubly protonated substance P, (a) without a Q lens doublet and (b) with a Q lens doublet. Both spectra were measured under the same condition, such as density of targets gas and condition of detector. The fragment ion peaks in Fig. 4.5.4(a) is over 5 times higher than that in Fig. 4.5.4(b). These results showed that the equipment of quadrupole doublet lens enables the increase of ion transmission efficiency [4].

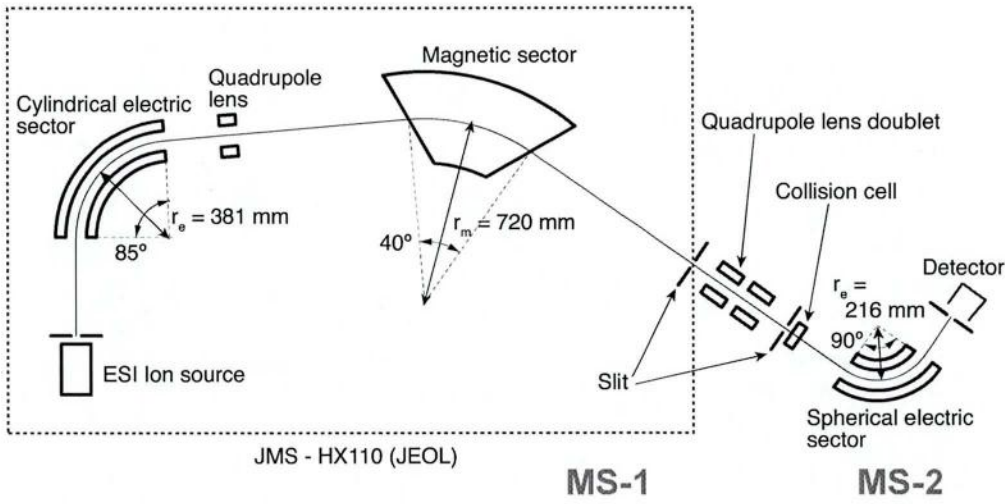


**Fig. 4.5.1.** Schematic diagram of the tandem sector mass spectrometer equipped with quadrupole doublet lens.

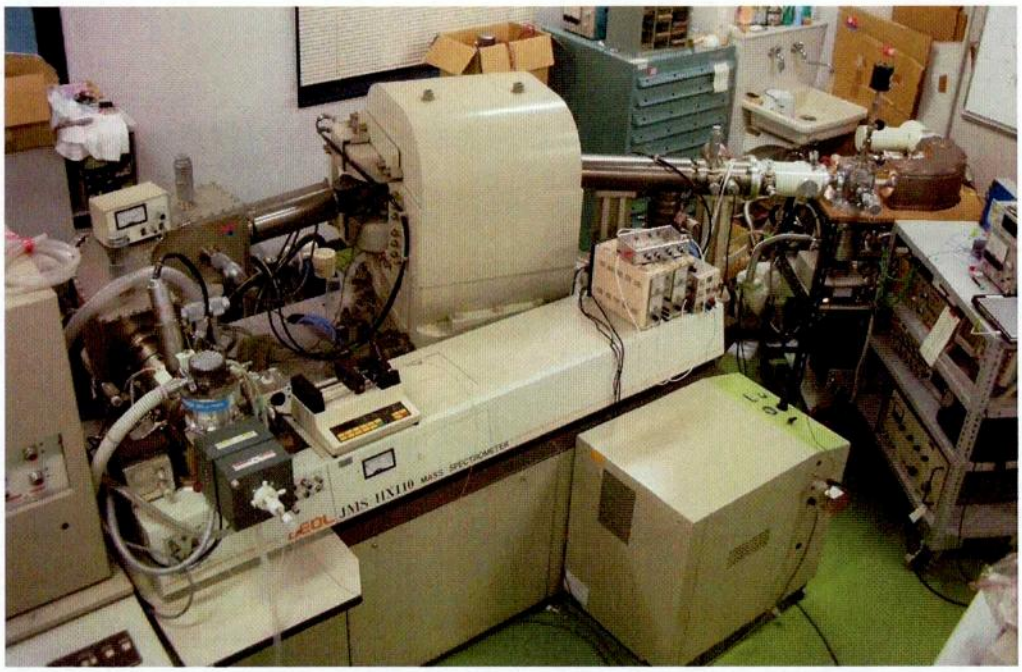

**Fig. 4.5.2.** Photograph of the MS/MS instrument equipped with quadrupole doublet lens.

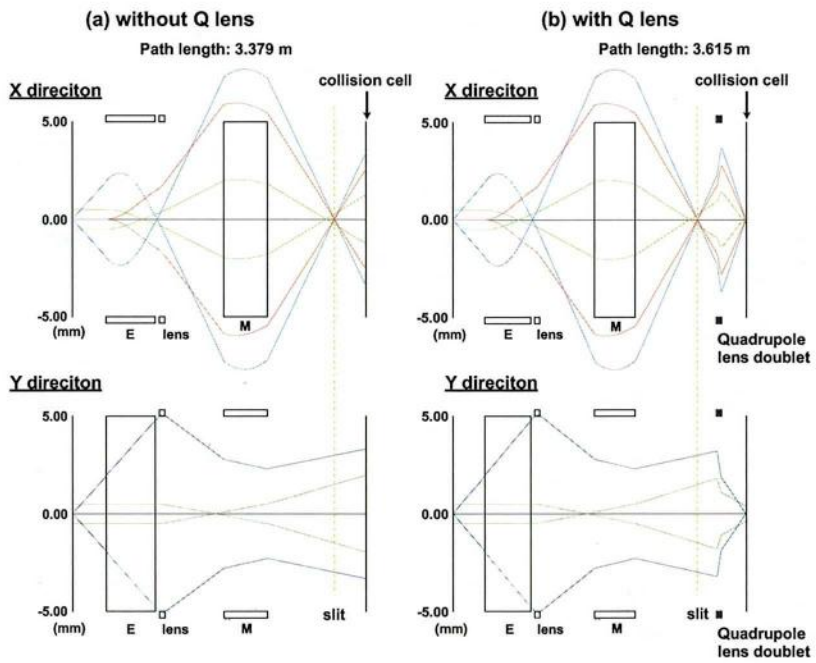


**Fig. 4.5.3.** Ion trajectories in the MS/MS instrument simulated by TRIO 2.0, (a) with a Q lens doublet and (b) without the Q lens doublet between MS-1 and MS-2.

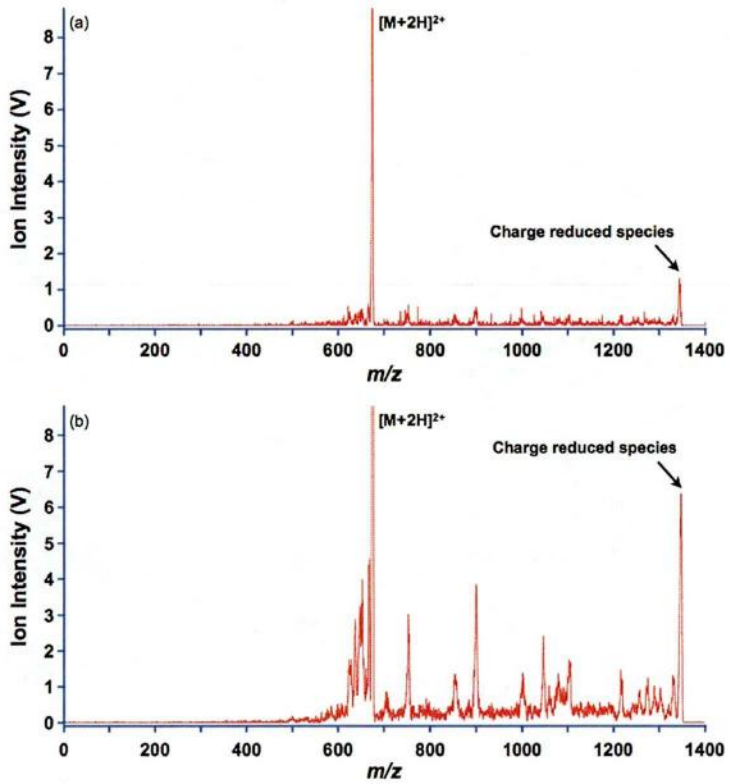


**Fig. 4.5.4.** High-energy ETD spectra of a doubly protonated substance P, (a) without a Q lens doublet and (b) with a Q lens doublet.

**Improvement of detection system**

The post-acceleration type detection system consists of a conversion dynode and secondary electron multiplier. Fig. 4.5.5 shows difference in ion trajectories obtained with (a) flat-shaped and (b) curved-shaped conversion dynodes. The "flat-shaped" and "curved-shaped" indicate the shape of the surface of the conversion dynodes.

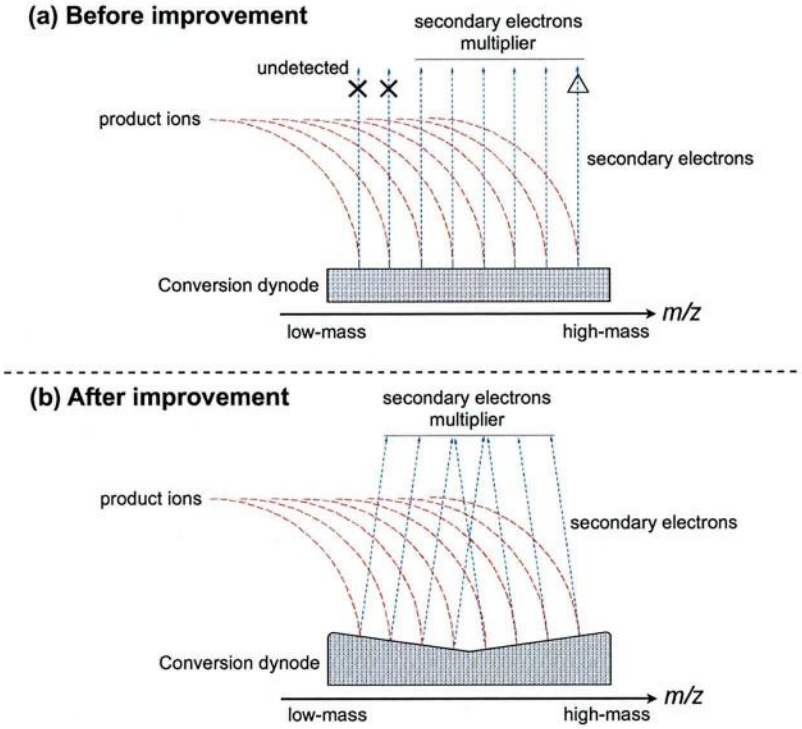


**Fig. 4.5.5.** Difference in ion trajectories obtained with (a) flat-shaped and (b) curved-shaped conversion dynodes.

In early research, a flat-shaped conversion was used, as shown in Fig. 4.5.5. In the case of (a), fragment ions of low *m/z* and high *m/z* could not be detected since secondary electrons escaping from the forwards and backwards of the conversion dynode could not reach the secondary electron multiplier, as shown in Fig. 4.5.5(a). In order to improve the mass range, the flat-shaped conversion dynode was changed to curved-shaped one. By using the curved-shaped conversion dynode, all the secondary electrons escaping from the conversion dynode were accelerated to the direction of the entrance of secondary electron multiplier, and all the fragment ions could be detected, as shown in Fig. 4.5.5(b). Fig. 4.5.6 shows difference in the high-energy ETD spectra of

the doubly protonated substance P with Cs as target, obtained by (a) flat-shaped and (b) curved-shaped conversion dynodes. While only the fragment ions of *m/z* 600 to 1400 are observed in Fig. 4.5.6(a), the fragment ions of *m/z* 0 to 1400 are observed in Fig. 4.5.6(b). As a result, immonium ions (P, R, K, Q), *a*-type ions (*a*2, *a*3, *a*4) and *c*4 ions are properly observed [4].

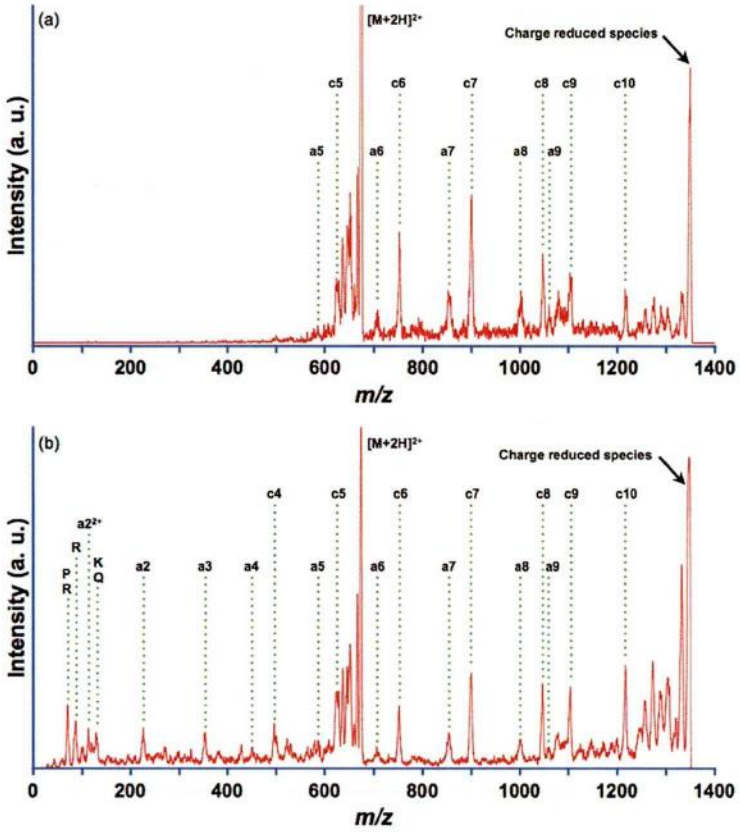


**Fig. 4.5.6.** Difference in the high-energy ETD spectra of the doubly protonated substance P with Cs as target, obtained with (a) flat-shaped and (b) curved-shaped conversion dynodes. The fragment ion intensities in lower and higher mass regions of spectrum (b) were much improved from those in spectrum (a).

**Investigation of high-energy CID and ETD of angiotensin II**

The sensitivity and mass range of this instrument were improved [4], then high-energy CID and ETD spectra of angiotensin II were obtained. The high-energy CID and ETD spectra of the doubly protonated angiotensin II [Angiotensin II+2H]$^{2+}$ ($\equiv$ [M+2H]$^{2+}$) with the Xe and Cs targets are shown in Fig. 4.5.7(a) and 4.5.7(b), respectively.

In the both spectra, the peaks of the precursor doubly protonated peptides at 523.7 are out of scale on the vertical axes. Their intensities were estimated from the gain of the secondary electron multiplier to be a few hundred times higher than that of the most intense fragment ions.

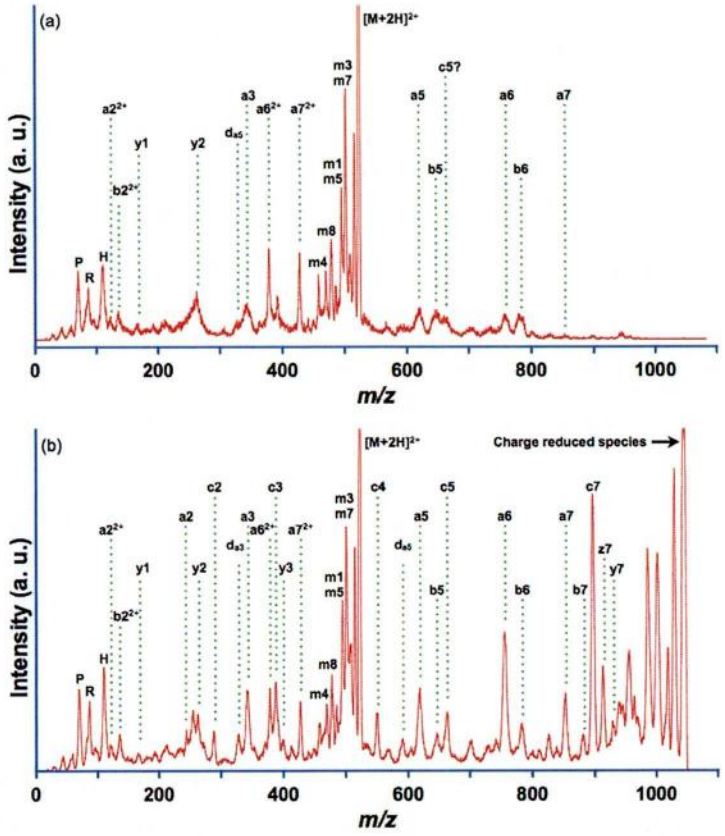


**Fig. 4.5.7** High-energy CID and ETD spectra of a doubly protonated angiotensin II with (a) Xe and (b) Cs targets.

In Fig. 4.5.7(a), the high intensity peaks at *m/z* 469.8, 478.2, 494.9, and 501.5 associated with *m*4, *m*8, *m*1 or *m*5, and *m*3 or *m*7 ions resulting from the loss of side chain from $[M+2H]^{2+}$ ions were dominantly observed. In addition, several singly and doubly charged *a*-, *b*-, and *y*-type ions were also observed. In case of Xe targets, the electron transfer from Xe target to protonated polypeptides hardly occur because of high ionization potential of Xe atom, then fragment ions formed by ETD were not observed. Therefore these fragment ions observed in Fig. 4.5.7(a) were formed by the high-energy CID process [7-11], as shown in scheme (4-5-1) and scheme (4-5-2),

**Scheme (4-5-1)**

$$AB^{2+} + T \rightarrow AB^{2+*} + T,$$
$$AB^{2+*} \rightarrow A^{2+} + B \text{ (or } A + B^{2+}).$$

**Scheme (4-5-2)**

$$AB^{2+} + T \rightarrow AB^{2+*} + T,$$
$$AB^{2+*} \rightarrow A^{+} + B^{+},$$

where, $AB^{2+}$ is $[M+2H]^{2+}$ ion and T is a Xe atom. The excited species ($AB^{2+*}$) are produced from their corresponding positive ions ($AB^{2+}$) by collision with a Xe target. The fragment ions ($A^{2+}$ or $B^{2+}$, $A^{+} + B^{+}$) produced from the dissociation of the excited ions ($AB^{2+*}$) were mass-analyzed and detected. While doubly-charged precursor ions produced doubly-charged fragment ions in the case of scheme (4-5-1), singly charged fragment ions are formed by charge separation reaction of precursor ions.

In Fig. 4.5.7(b), same *a*-, *b*-, *y*-, and *m*- type ions, which were observed in Fig. 4.5.7(a), were also observed in high-energy ETD spectrum with Cs targets. Therefore these fragment ions observed in Fig. 4.5.7(b) are formed by the high-energy CID process, as shown in scheme (4-5-1) and scheme (4-5-2), since the mass of the two target atoms is quite similar and provides the identical center of mass energies. The product ion peaks associated with $M^{+}$ or $[M+H]^{+}$, or $[M+2H]^{2+}$, which were not observed in CID spectrum with the Xe targets, are dominantly observed in Fig. 4.5.7(b). Unfortunately, these ion peaks could not be identified because of the low resolution of MS-2, although there is no doubt that these ions are formed by electron transfer from a Cs atom to $[M+2H]^{2+}$. Additionally, it is also clearly seen that there is a strong enhancement of peaks corresponding to *c*-type ions (*c*2-*c*4, *c*5, c7). The *c*-type ions are characteristic of ECD and ETD, then a series of *c*- ion peaks are observed only in ECD and ETD spectra [12-18]. Therefore, it is concluded that these *c*-type ions are formed by the ETD process, as shown in scheme (4-5-3),

**Scheme (4-5-3)**

$$AB^{2+} + T \rightarrow AB^{+*} + T^{+},$$
$$AB^{+*} \rightarrow A^{+} + B \text{ or } (A + B^{+}),$$

where T is a Cs atom. The excited species ($AB^{+*}$) are produced from their corresponding positive ions ($AB^{2+}$) by electron transfer from the alkali metal target. The

fragment ions ($A^+$ or $B^+$) obtained from the dissociation of the excited ions ($AB^{+*}$) were mass-analyzed and detected, as shown in the following reaction scheme (4-5-3).

The spacing between the peaks of *c*- ions are corresponding to the mass of the amino acid. From the spacing of *c*-type ions, the part of the amino acid sequence could be determined, as shown in Fig. 4.5.7(b). However, the peaks corresponding to *c*6 are missing. It is noted that ECD and ETD is unable to break the amine backbone bonds on the N-terminal side of proline [12]. The predominance of N-terminal *c*-type ions can be understood from the amino acid sequence of angiotensin II. The N-terminal amino acid is arginine that is likely to carry the charge since it is the most basic amino acid. As C-terminal *z*-fragment ions, only the *z7* ion was observed. This is because the C-terminal *z*-fragment ions including arginine is only *z7* ions, then complementary z-fragments except for *z7* ions are hence neutral and can not be detected in this experiment [5].

In order to evaluate the high-energy ETD efficiency, high-energy ETD efficiency was compared with high-energy CID efficiency. Both high-energy ETD efficiency and high-energy CID efficiency were defined as the abundance of fragment ions ($F_{out}$) divided by the abundance of the precursor ions ($P_{in}$) entering the collision cell. This result indicated that high-energy ETD efficiency was about 6 times larger than high-energy CID efficiency.

**Investigation of high-energy ETD of bradykinin.**

The high-energy ETD spectra of the doubly protonated bradykinin ions $[M+2H]^{2+}$ spectrum was shown in Fig. 4.5.8. Not dissociated $[M + 2H]^{2+}$ is at *m/z* 530.8. As in the case of angiotensin II, the peak of $M^+$ formed by electron transfer is the dominating peak. Additionally, in contrast to the case of angiotensin II, both *c*- ions (*c*3-*c*5, *c*7, *c*8) and their complementary *z*- ions (*z*1, *z*2, *z*4-*z*6) are clearly observed. This phenomenon can be explained by the presence of two arginine amino acids (N-terminal and C-terminal) in the bradykinin [5]. These *c*- and *z*-type ions provided the information of amino acid sequence of bradykinin.

The results on high-energy ETD experiments indicated that (1) *c*- and *z*-type ions were mainly formed in the high-energy ETD process, as expected, (2) high-energy ETD efficiency was about 6 times higher than that of high-enegy CID, (3) high-energy ETD was useful in determining the amino acid sequence of doubly protonated polypeptides.

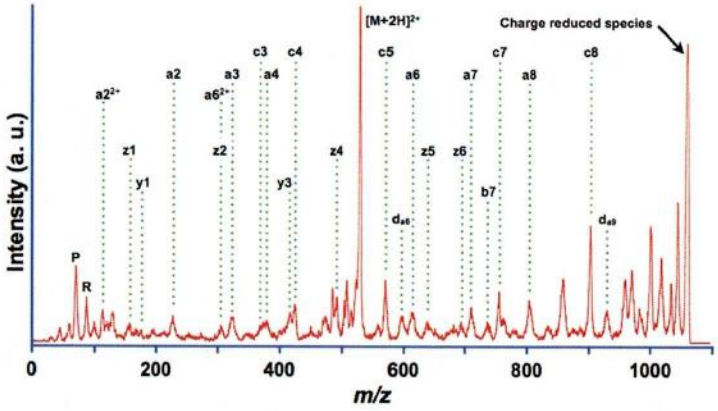


**Fig. 4.5.8** High-energy ETD spectrum of a doubly protonated angiotensin II using Cs targets.

In the next section, high-energy ETD of multiply protonated peptides with posttranslational modifications (PTMs) are investigated in order to confirm that high-energy ETD is useful in the structural analysis of the peptides with PTMs.

## References


[1] H. Nagao, M. Toyoda, S. Hayakawa, K. Iwamoto, T. Ichihara, K. Kawamura, K. Awazu, Eur. J. Mass Spectrom. 15 (2009) 459.

[2] S. Hayakawa, K. Minami, K. Iwamoto, M. Toyoda, T. Ichihara, H. Nagao, Int. J. Mass Spectrom. 266 (2007) 122

[3] S. Hayakawa, K. Minami, K. Iwamoto, M. Toyoda, T. Ichihara, H. Nagao, Int. J. Mass Spectrom. 266 (2007) 122.

[4] H. Nagao, S. Hayakawa, M. Hashimoto, K. Iwamoto, T. Toyoda, Y. Shigeri, M. Jitosho, K. Awazu, J. Mass Spectrom. Soc. Jpn. 57 (2009) 123-132.

[5] P. Hvelplund, B. Liu, S.B. Nielsen, S. Tomita, Int. J. Mass Spectrom. 225 (2003) 83.

[6] M. Nishiguchi, M. Toyoda, Physics Procedia. 1 (2008) 323.

[7] K. Biemann, S.A. Martin, Mass Spectrom. Rev. 6 (1987) 1.

[8] R.S. Johnson, S.A. Martin, K. Biemann, Int. J. Mass Spectom. Ion Process. 86 (1988) 137.

[9] R.A.J. O'Hair, M.L. Styles, G.E. Reid, J. Am. Soc. Mass Spectrom. 9 (1998) 1275.

[10] I.A. Papayannopoulos, Mass Spectrom. Rev. 14 (1995) 49.

[11] J.T. Stults, J. Lai, S. McCune, R. Wetzel, Anal. Chem. 65 (1993) 1703.

[12] R.A. Zubarev, N.L. Kelleher, F.W. McLafferty, J. Am. Chem. Soc. 120 (1998) 3265.

[13] R.A. Zubarev, N.A. Kruger, E.K. Fridriksson, M.A. Lewis, D.M. Horn, B.K. Carpenter, F.W. McLafferty, J. Am. Chem. Soc. 121 (1999) 2857.

[14] R.A. Zubarev, D.M. Horn, E.K. Fridriksson, N.L. Kelleher, N.A. Kruger, M.A. Lewis, B.K. Carpenter, F.W. McLafferty, Anal. Chem. 72 (2000) 563.

[15] R.A. Zubarev, Mass Spectrom. Rev. 22 (2003) 57.

[16] J.E.P. Syka, J.J. Coon, M.J. Schroeder, J. Shabanowitz, D.F. Hunt, Proc. Natl. Acad. Sci. U. S. A. 101 (2004) 9528.

[17] J.J. Coon, J.E.P. Syka, J.C. Schwartz, J. Shabanowitz, D.F. Hunt, Int. J. Mass Spectrom. 236 (2004) 33.

[18] P.A. Chrisman, S.J. Pitteri, J.M. Hogan, S.A. McLuckey, J. Am. Soc. Mass Spectrom. 16 (2005) 1020.

## 4.6 High-energy ETD of doubly protonated phosphopeptides using the alkali metal target

### 4.6.1 Introduction

In section 4.5, it was demonstrated that the dissociation efficiency of high-energy ETD is about 6 times higher than that of high-energy CID, and high-energy ETD is useful in determining the structural analysis of doubly protonated polypeptides. In this section, high-energy ETD is applied to the protonated peptides with posttranslational modification (PTMs) in order to confirm that the high-energy ETD enables the structural analysis of protonated peptides with PTMs as in the case of ETD. The usefulness of ETD is associated with N–Cα backbone cleavage to form *c*- and *z*-type ions [1, 2] with no loss of PTMs groups [3–8] such as phosphate and sulfate groups [9,10]. PTMs of proteins are of great importance in the activation, localization, and regulation of protein functions in vivo. Especially, reversible protein phosphorylation, principally localized on serine, threonine or tyrosine residues, is one of the most important and well-studied PTMs. Phosphorylations play crucial roles in the regulation of cellular processes such as cell cycle, growth, apoptosis and signal transduction [11,12]. Therefore high-energy ETD of phosphopeptides is investigated [13].

In this section, five synthetic peptides (YGGMHRQET(p)VDC, YGGMHRQEY(p)VDC, YGGMHRQES(p)VDC, TGFLT(p)EY(p)VATR, TGFLS(p)EY(p)VATR) are utilized as a representative of phosphopeptides in order to demonstrate that the amino acid sequence of a phosphopeptide and the position of phosphorylation are determined by high-energy ETD. In addition, ETD and high-energy ETD spectra of the three phosphopeptide (YGGMHRQET(p)VDC, YGGMHRQEY(p)VDC, TGFLT(p)EY(p)VATR) are compared in order to show the advantage of high-energy ETD.

### 4.6.2 Experimental section

**High-energy ETD experiment**

Five phosphopeptides (YGGMHRQET(p)VDC, YGGMHRQEY(p)VDC, YGGMHRQES(p)VDC, TGFLT(p)EY(p)VATR, TGFLS(p)EY(p)VATR) were synthesized by use of a Shimadzu PSSM-8 automated peptide synthesizer according to

the method of Wakamiya et al. [14] and the obtained peptide was purified by reversed-phase HPLC [15]. The peptides were electrosprayed from a solution of 1:1 water:methanol containing 2% acetic acid. Doubly-protonated peptides were generated. A sample solution was infused into an electrospray emitter at a flow rate of 30 μL/min. About 4 keV was applied between the electrospray emitter and the desolvating plate. Electrosprayed ions were delivered into the mass spectrometer.

**ETD experiment by using the commercial apparatus**

Three phosphopeptides (YGGMHRQET(p)VDC, YGGMHRQEY(p)VDC, TGFLT(p)EY(p)VATR) were measured on Finnigan LTQ XL (Thermo Fisher Scientific K.K.). Doubly-protonated peptide ion was generated by an nano-ESI. Mono-isotopic ions were mass-selected and reacted with fluoranthene anions with normalized energy of 35% and a length of 200 ms/per single scan. 200 single scan spectra were integrated.

## 4.6.3 Results and Discussion

The high-energy ETD spectra of the doubly protonated phosphopeptide $[(YGGMHRQEX(p)VDC)+2H]^{2+}$ ($\equiv[M+2H]^{2+}$) (X= S, T, Y) with the Cs target were shown in Figs. 4.6.1(a) - (c), respectively. In all spectra, the peaks of the precursor doubly-protonated ions were out of scale on the vertical axes. Their intensities were estimated from the gain of the secondary electron multiplier to be a few hundred times higher than that of the most intense fragment ions. Although the phosphorylated amino acids of three phosphopeptides are different, three spectra have similar appearance. In fact, five *a*-type ions (*a*5-*a*7, *a*10-*a*11), *b*3 ions, five *c*-type ions (*c*7-*c*11), four *y*-type ions (*y*7-*y*11), and four *z*-type ions (*z*7-*z*11) are observed in all spectra, in common. Especially, *c*- and *z*-type ions with no loss of phosphate group could be clearly observed. As a result, the position of phosphate groups and amino acid sequence of phosphopeptides could be determined by these fragment ions. The fragment pattern associated with *c*- and *z*-type ions were organized in Fig. 4.6.2 in order to interpret the fragment pattern. The peaks corresponding to *c*1-*c*4 and *z*1-*z*6 were missing. The absence of *c*1-*c*4 and *z*1-*z*6 ions could be understood from the amino acid sequence of these phosphopeptides. The sixth amino acid from N-terminal in phosphopeptide (YGGMHRQEX(p)VDC) is arginine that is likely to carry the charge since it is the

most basic amino acid. The $c1$-$c4$ and $z1$-$z6$ fragments were hence neutral and could not be detected in the present experiment. The phosphorylation site and amino acid sequence of three phosphopeptides, which have one phosphorylated site, could be determined by high-energy ETD.

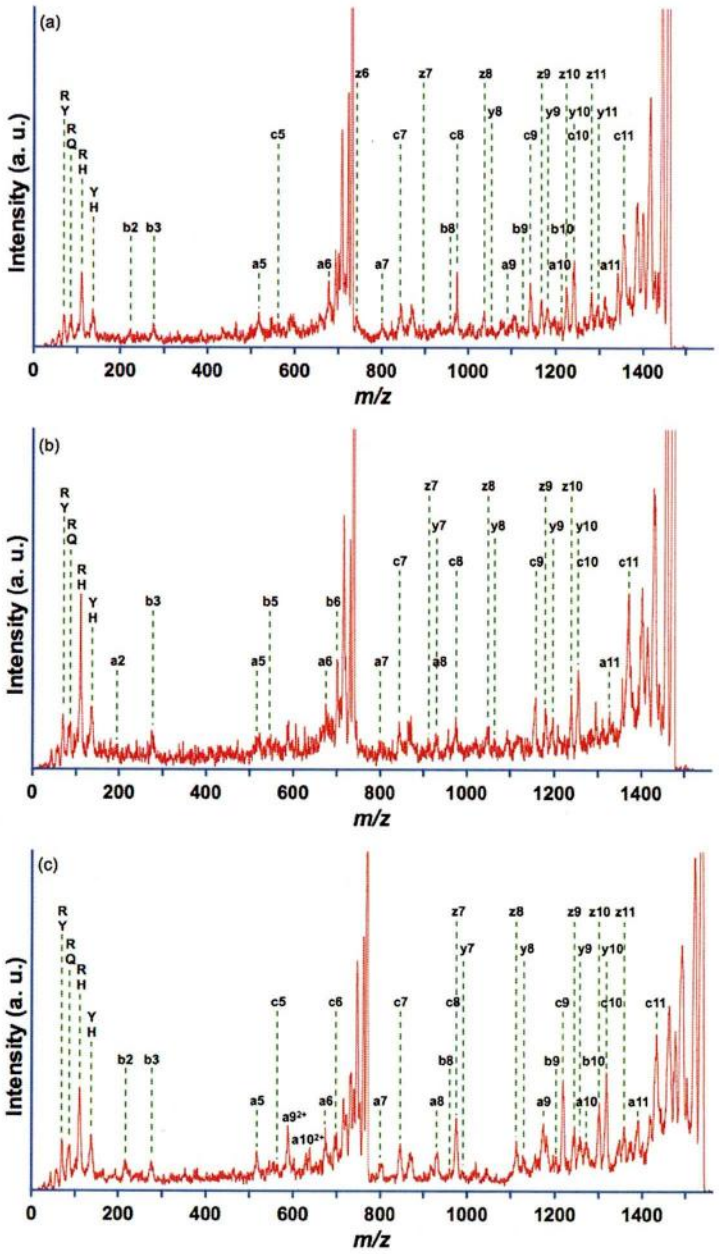


**Fig. 4.6.1.** High-energy ETD spectra of the doubly-protonated phosphorylated peptide $[(YGGMHRQEX(p)VDC)+2H]^{2+}$ ($\equiv[M+2H]^{2+}$) (X=(a)S, (b)T, (c)Y) with a Cs target.

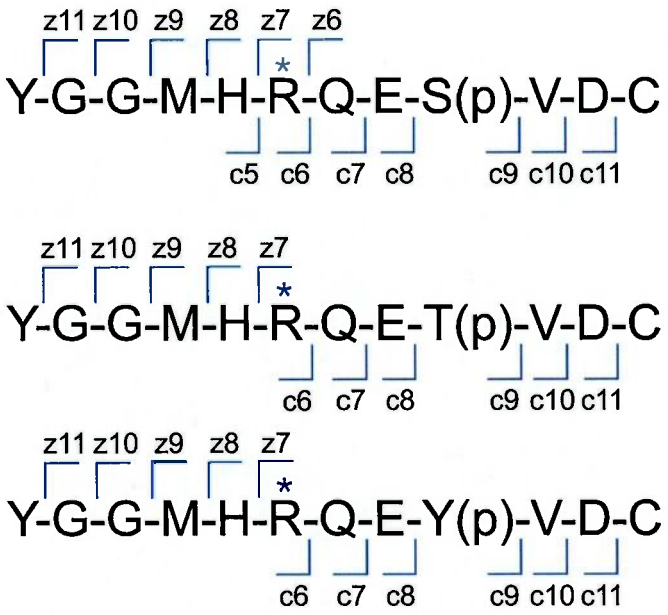


**Fig. 4.6.2.** Fragment patterns of phosphopeptide (YGGMHRQEX(p)VDC). X =S, T, Y. Only *c*- and *z*-type ions are assigned here.

Next, two phosphopeptides, which have two phosphorylated site, were measured by high-energy ETD in order to confirm that the amino acid sequence and modification site of the phosphopeptides are determined by high-energy ETD. High-energy ETD spectra of the doubly protonated phosphopeptide $[(TGFLX(p)EY(p)VATR)+2H]^{2+}$ ($\equiv [M+2H]^{2+}$) (X= S, T) with the Cs target are shown in Figs. 4.6.3(a) and (b), respectively. In these spectra, the peaks of the precursor doubly-protonated ions $[M+2H]^{2+}$ are out of scale on the vertical axes. As the same of phosphopeptides (YGGMHRQEX(p)VDC), these two spectra in Fig. 4.6.3 are very similar. In the case of phosphopeptides (TGFLX(p)EY(p)VATR), complete *y*- and *z*-type ions with no loss of phosphate groups are clearly observed. Therefore the position of phosphate groups and amino acid sequence of phosphopeptides could be determined by these fragment ions. The fragment pattern associated with *c*- and *z*-type ions were organized in Fig. 4.6.4 in order to interpret the fragment pattern. The absence of *c*-type ions was same reason in the case of phosphopeptides (YGGMHRQEX(p)VDC) and it can be understood from the amino acid sequence.

These results indicated that that (1) *c*- and *z*-type ions with no loss of phosphate groups are formed in the high-energy ETD process, (2) the types of phosphorylated

amino acid less depend on the fragment patterns in high-energy ETD experiments, (3) as a result, high-energy ETD with the alkali metal target allowed determination of the position of phosphorylation and the amino acid sequence of post-translational peptides.

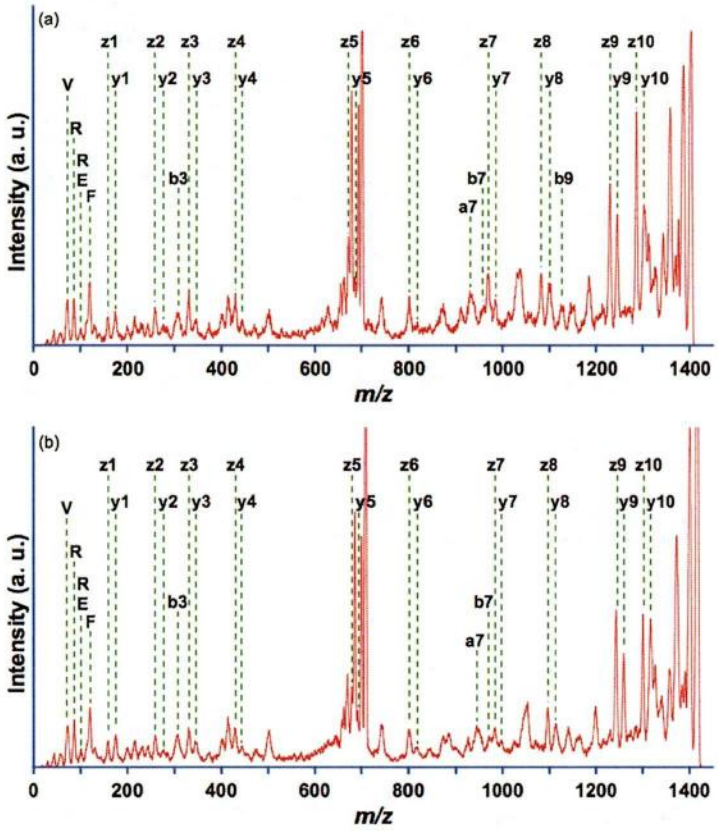


**Fig. 4.6.3.** High-energy ETD spectra of the doubly-protonated phosphorylated peptide $[(TGFLX(p)EY(p)VATR)+2H]^{2+}$ ($\equiv[M+2H]^{2+}$) (X=(a)S, (b)T) with a Cs target.

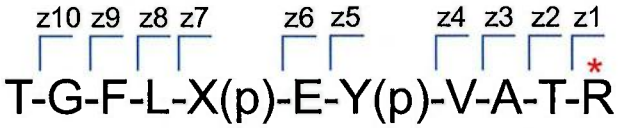


**Fig. 4.6.4.** Fragment patterns of phosphopeptide (TGFLX(p)EY(p)VATR). X = S, T. Only *c*- and *z*-type ions are assigned here.

Subsequently, the ETD and high-energy ETD spectra of the doubly protonated phosphopeptide $[(YGGMHRQET(p)VDC)+2H]^{2+}$ ($\equiv[M+2H]^{2+}$) are shown in Figs. 4.6.5(a) and (b), respectively. Although various fragment ions are observed in these spectra, only the *c*- and *z*-type ions are assigned in Figs. 4.6.5(a) and (b). Same *c*-

(*c*5-*c*11) and *z*- (*z*7-*z*11) type ions are observed in both spectra. The position of phosphate group and amino acid sequence of the phosphopeptides could be determined in both high-energy ETD and ETD spectra.

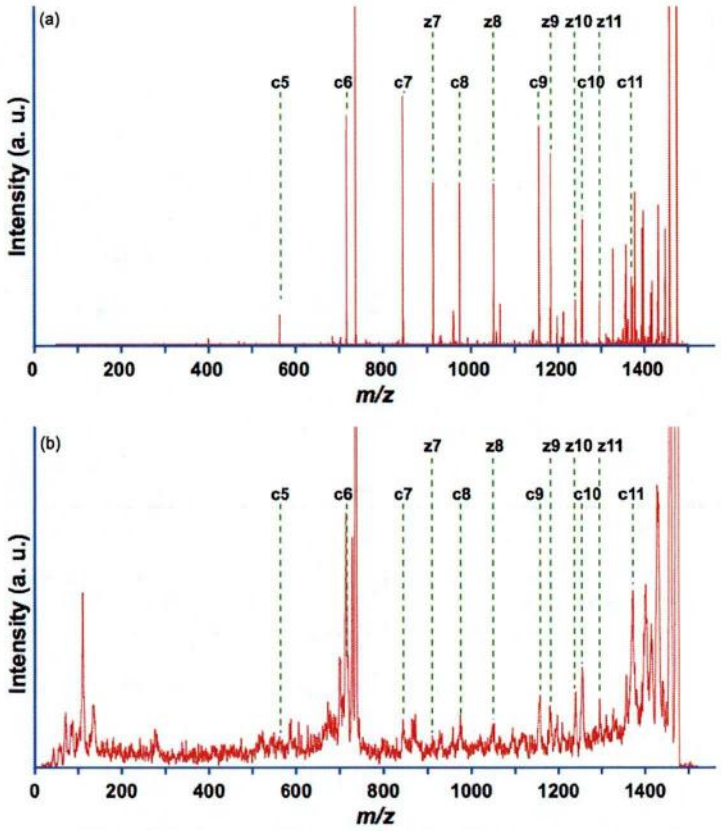


**Fig. 4.6.5.** ETD (a) and high-energy ETD (b) spectra of the doubly-protonated phosphorylated peptide [(YGGMHRQET(p)VDC)+2H]2+ (≡[M+2H]2+)

The ETD and high-energy ETD spectra of the doubly protonated phosphopeptide $[(YGGMHRQEY(p)VDC)+2H]^{2+}$ ($\equiv[M+2H]^{2+}$) are shown in Figs. 4.6.6(a) and (b), respectively. Only the *c*- and *z*-type ions were focused on and assigned in Figs. 4.6.6(a) and (b). Two *c*-type ions (*c*7, *c*8) and *z*7 ion, which are observed in Fig. 4.6.6(b), are not observed in Fig.4.6.6(b). It is not possible to determine the position of phosphate group and amino acid sequence of the phosphopeptide in Fig. 4.6.6(b) due to the lack of *c*7, *c*8, and *z*7 ions.

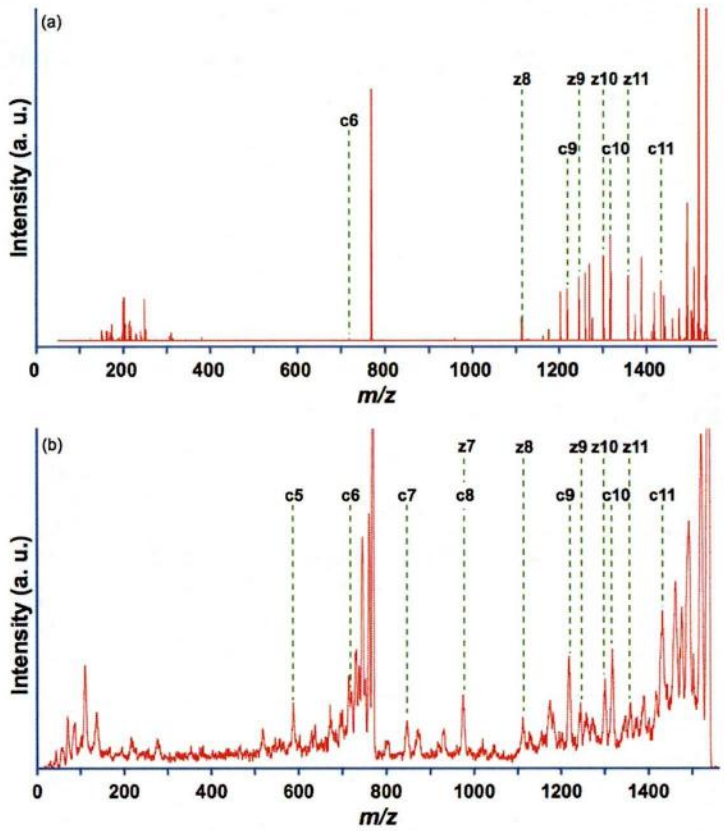


**Fig. 4.6.6.** ETD (a) and high-energy ETD (b) spectra of the doubly-protonated phosphorylated peptide $[(YGGMHRQEY(p)VDC)+2H]^{2+}$ ($\equiv[M+2H]^{2+}$)

As shown in Figs. 4.6.5(b) and 4.6.6(b), there is no difference except for the type of phosphorylated amino acid in these two spectra. There are some possible reasons of the lack of *c*7, *c*8, and *z*7 ions. In ETD experiments, both positive ions and negative ions are necessary to be trapped in a linear trap in a same time and reacted in a few hundred milliseconds in order to increase the fragmentation efficiency. However, as a result, using linear ion trap to improve the fragmentation efficiency has some weak points. First, most conventional ion traps operate with a compromise low mass cut-off of about 1/3 the mass of the precursor ion [16, 17]. Hence, some of the fragment ions formed by ETD are not observed in the ETD spectrum. It is a serious problem to determine the amino acid sequence of peptides completely. Secondly, the reaction between positive ions and negative ions is performed in multiple collision condition because of long reaction time (~300 ms). Therefore, singly charged fragment ions formed by ETD of doubly charged ions are easy to neutralize by electron transfer from another negative

ions. For this reason, even if the reaction time increases, the amounts of fragment ions do not necessarily increase. The lack of $c7$, $c8$, and $z7$ ions was related to one of the some weak point of ETD.

The ETD and high-energy ETD spectra of the doubly protonated phosphopeptide $[(TGFLT(p)EY(p)VATR)+2H]^{2+}$ ($\equiv[M+2H]^{2+}$) are shown in Figs. 4.6.7(a) and (b), respectively.

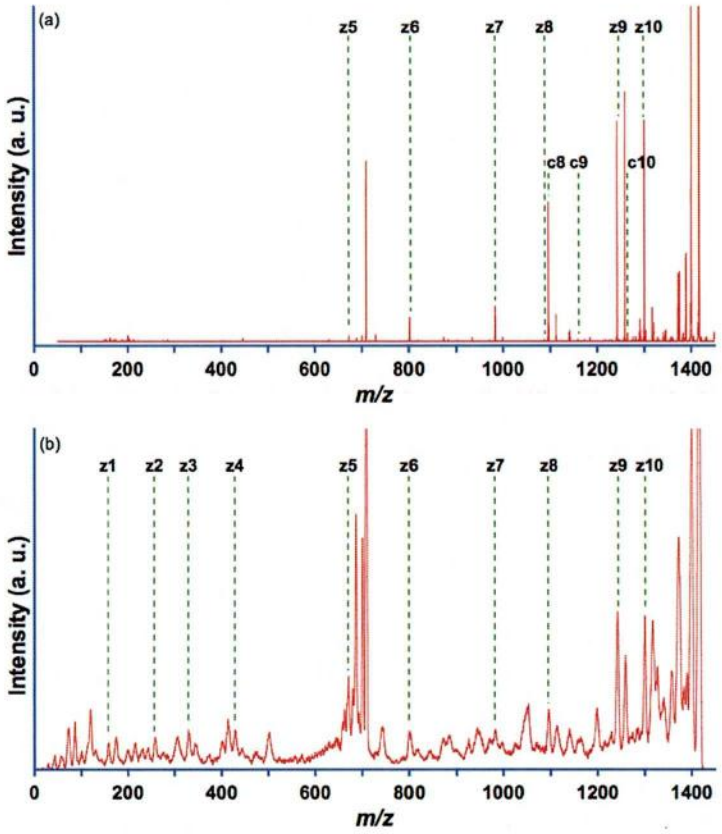


**Fig. 4.6.7.** ETD (a) and high-energy ETD (b) spectra of the doubly-protonated phosphorylated peptide $[(TGFLT(p)EY(p)VATR)+2H]^{2+}$ ($\equiv[M+2H]^{2+}$)

Although various fragment ions are observed in these spectra, only the c- and $z$-type ions are assigned. Although all $z$-ions ($z1$-$z10$) are clearly observed in Figs. 4.6.7(a), $z1$-$z4$ ions are missing in Figs. 4.6.7(b), because of the low mass cut-off [16, 17] of an ion trap. In case of Figs. 4.6.7(b), it is obviously impossible to determine the position of phosphate groups and amino acid sequence of phosphopeptide.

These results of three phosphopeptides demonstrated that high-energy ETD is expected to be more useful than ETD in phosphopeptide analysis since (1) the

high-energy ETD less depends on amino acid component, (2) fragment ions of low *m/z* value could be observed due to the absence of low mass cut off, and (3) neutralization of fragment ions did not occur due to single collision reaction between the alkali metal target and protonated peptides.

## References


[1] P. Roepstorff, J. Fohlman, Biomed. Mass Spectrom. 11 (1984) 601.

[2] K. Biemann, Biomed. Environ. Mass Spectrom. 16 (1988) 99.

[3] R.A. Zubarev, N.L. Kelleher, F.W. McLafferty, J. Am. Chem. Soc. 120 (1998) 3265.

[4] R.A. Zubarev, N.A. Kruger, E.K. Fridriksson, M.A. Lewis, D.M. Horn, B.K. Carpenter, F.W. McLafferty, J. Am. Chem. Soc. 121 (1999) 2857.

[5] R.A. Zubarev, K.F. Haselmann, B. Budnik, F. Kjeldsen, F. Jensen, Eur. J. Mass Spectrom. 8 (2002) 337.

[6] R.A. Zubarev, Mass Spectrom. Rev. 22 (2003) 57.

[7] J.E.P. Syka, J.J. Coon, M.J. Schroeder, J. Shabanowitz, D.F. Hunt, Proc. Natl. Acad. Sci. USA 101 (2004) 9528.

[8] J.J. Coon, J.E.P. Syka, J.C. Schwartz, J. Shabanowitz, D.F. Hunt, Int. J. Mass Spectrom. 236 (2004) 33.

[9] A. Stensballe, O.N. Jensen, I.V. Olsen, K.F. Haselmann, R.A. Zubarev, Rapid Commun. Mass Spectrom. 14 (2000) 1793.

[10] S.D.H. Shi, M.E. Hemling, S.A. Carr, D.M. Horn, I. Lindh, F.W. McLafferty, 209. Anal. Chem. 73 (2001) 19.

[11] G. Manning, G.D. Plowman, T. Hunter, S. Sudarsanam, Trends Biochem. Sci. 27 (2002) 514.

[12] A. Ishida, I. Kameshita, N. Sueyoshi, T. Taniguchi, Y.J. Shigeri, Pharmacol. Sci. 103 (2007) 5.

[13] S. Hayakawa, M. Hashimoto, H. Nagao, K. Awazu, M. Toyoda, T. Ichihara, Y. Shigeri, Rapid Commun. Mass Spectrom. **22** (2008) 567.

[14] T. Wakamiya, R. Togashi, T. Nishida, K. Saruta, J. Yasuoka, S. Kusumoto, S. Aimoto, K.Y. Kumagaye, K. Nakajima, K. Nagata, Bioorg. Med. Chem. 5 (1997) 135.

[15] A. Ishida, Y. Shigeri, Y. Tatsu, Y. Endo, I. Kameshita, S. Okuno, T. Kitani, M. Takeuchi, N. Yumoto, H. Fujisawa, J. Biochem. 129 (2001) 745.

[16] Y.H. Yang, K. Lee, K.S. Jang, Y.G. Kim, S.H. Park, C.S. Lee, B.G. Kim, Anal. Biochem. 387 (2009) 133.

[17] M.Y. Zhang, N. Pace, E.H. Kerns, T. Kleintop, N. Kagan, T. Sakuma, J. Mass Spectrom. 40 (2005) 1017.

# Chapter 5

## Development of a tandem time of flight mass spectrometer with ESI ion source "ESI-TOF/TOF"

### 5.1 Introduction

In section 4.5-4.6, it was demonstrated that high-energy ETD was useful in determining the structural analysis of polypeptides and phosphopeptides. However, the tandem sector mass spectrometer requires large amount of sample. In addition, mass resolution of fragment ions is very low because fragment ions are mass-separated by only an electric field without magnetic field. Therefore, the sensitivity and mass resolution of the instrument is not enough to measure the biological samples. If high-energy ETD spectra can be obtained in TOF/TOF, it is expected that the drawbacks of the tandem sector mass spectrometer are improved. However, a tandem TOF mass spectrometer has not yet been combined with an ESI ion source, although the MALDI-TOF/TOF have been widely used for analyzing biological samples.

There are two primary reasons why an ESI-TOF/TOF has not been assembled until now. The first is that the mass resolution of fragment ions analysis in TOF/TOF is generally insufficient to analyze multiply charged fragment ions. Since multiply charged ions are often generated in ESI, their isotopomers are spaced at fractional u, depending on the charge state of the ions. For this reason, high mass resolution is required to determine the charge state and *m/z* of fragment ions. The second reason is related to the technical challenges of designing such an instrument. In order to achieve high-energy collisions between the analyte ions and target gas, either the ESI ion source or the tandem TOF mass spectrometer (linear TOF mass spectrometer, collision cell, ion mirror, and detector) needs to be operated at elevated voltage, which is not easy. In order to operate the instrument at elevated voltage, its rotary pumps should also be operated at elevated voltage. Therefore, it would be best if the ESI ion source and the tandem TOF mass spectrometer were operated at ground potential. However, there has never yet been a technique to enable high-energy collisions when both the ESI ion source and the tandem TOF mass spectrometer are operating at ground potential. Other

reasons include the low resolving power in precursor ion selection and the low duty cycle.

In this chapter, development of a tandem TOF mass spectrometer with an ESI ion source "ESI-TOF/TOF" is described. The ESI-TOF/TOF was newly developed in order to obtain high-energy ETD spectra of multiply protonated peptides ionized by ESI. The details of the ESI-TOF/TOF and experimental results are shown below.

## 5.2 Instrumentation and experiment

### 5.2.1 Tandem time-of-flight mass spectrometer with an ESI ion source "ESI-TOF/TOF"

A new tandem TOF mass spectrometer with an ESI ion source, ESI-TOF/TOF, was designed and constructed in order to achieve high resolution in fragment ion analysis, high quality structural information via high-energy CID, and simultaneous detection of all fragment ions. A schematic diagram and photograph of the device are shown in Figs. 5.1 and 5.2, respectively. This system consisted of an orthogonal acceleration type ESI ion source, a linear TOF mass spectrometer (MS-1), a collision cell, a quadratic-field ion mirror (MS-2) [1,2], and a microchannel plate (MCP) detector. The size of this device is 1.1 m. Each part of this assembly is described in detail below.

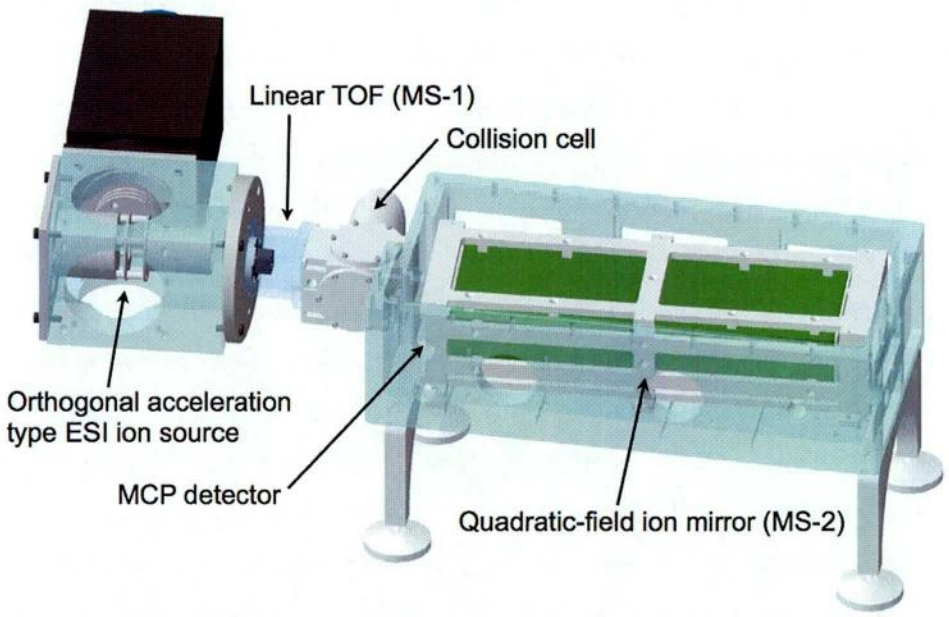


**Fig. 5.1.** A schematic drawing of ESI-TOF/TOF.

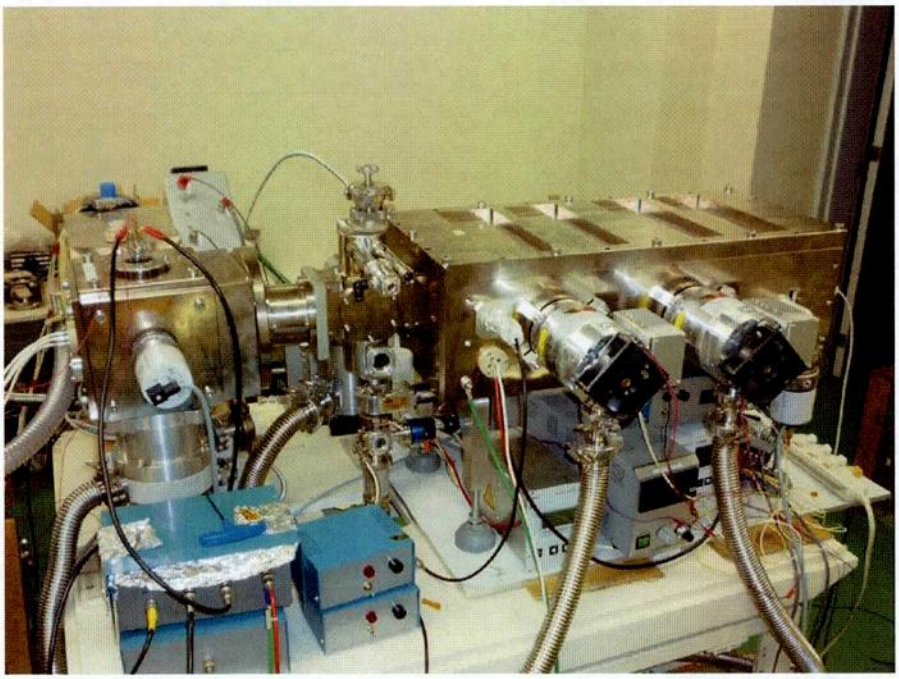

**Fig. 5.2.** Photograph of ESI-TOF/TOF. The orthogonal acceleration type ESI ion source is at the left, linear TOF (MS-1) and collision cell in the center, and quadratic-field ion mirror (MS-2) on the right.

### 5.2.2 Orthogonal acceleration type ESI ion source

The connection between the ESI ion source and the tandem TOF mass spectrometer is discussed below. A TOF spectrometer must accelerate ions in a pulsed manner in the ion acceleration region in order to analyze variations in *m/z* as elapsed times starting from a given time. Therefore, TOF spectrometers are very compatible with pulsed ionization methods such as MALDI. However, ESI is a continuous ionization method. Continuous ion sources such as ESI are generally interfaced to TOF spectrometers by an "orthogonal acceleration device" (OA) [3,4]. The continuous ion beam with kinetic energies of tens of V introduced into the OA region is accelerated along an axis perpendicular to its initial direction of motion. When the ESI ion source was connected to the TOF spectrometer, two methods were considered in order to achieve high-energy acceleration. One was that the ESI ion source and the TOF instrument were to be operated at high positive voltage and ground potential, respectively, for the analysis of positive ions. However, it was difficult to operate this source at a high positive voltage since the associated rotary pumps also needed to be

operated at a high positive voltage. The other alternative was to operate the ESI ion source and the TOF instrument at ground potential and a high negative voltage, respectively, as in the case of ESI-TOF mass spectrometers in general. In the case of ESI-TOF/TOF, however, the collision cell, the ion mirror, and the detector were also operated at high negative voltage in order to achieve high-energy CID, making the design of the tandem TOF instrument more complicated in order to prevent electric discharges. Therefore, it was decided to operate both the ESI ion source and the collision cell at ground potential.

In order to achieve this, a potential-lift [5-8] was used to connect the ESI ion source to the tandem TOF instrument. A potential-lift is a device for increasing the energy of ions in a TOF mass spectrometer. A schematic drawing of a potential-lift is shown in Fig. 5.3; it is essentially one flight-tube electrode. A high negative voltage is initially applied to the potential-lift.

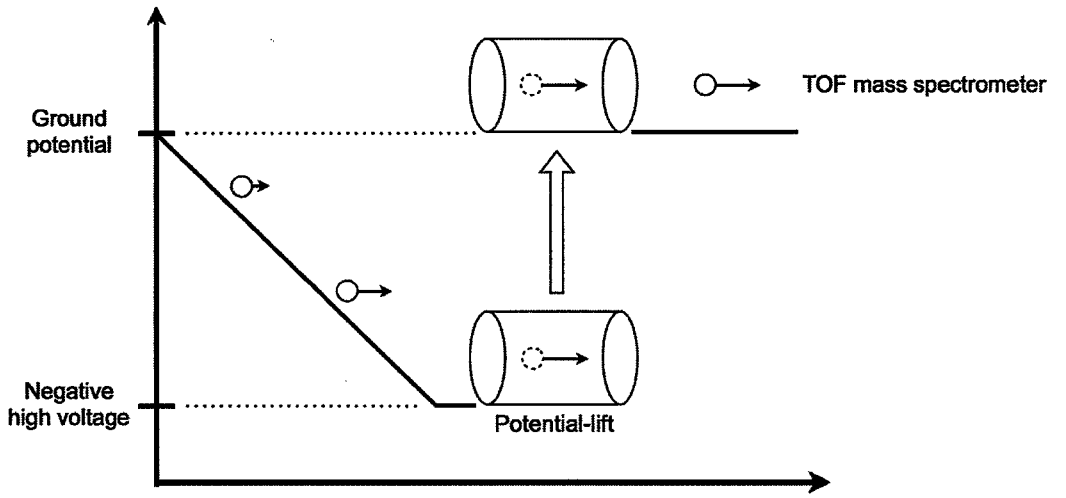


**Fig. 5.3.** Schematic diagram of the potential-lift.

For example, when positive ions are accelerated from the initial position at ground potential and enter the potential-lift, they are accelerated by the difference in potential between that at their initial position and that of the potential-lift. When the voltage of the potential-lift was kept at a high negative voltage, the velocity of the positive ions decreased before they reached the TOF mass spectrometer at ground potential, and they were not accelerated to high energies. Thus, the voltage on the potential-lift was switched from a negative voltage to ground potential during the passage of the ions

through the potential-lift. Their velocities were conserved when the voltage of the potential-lift was changed as described above, resulting in fully accelerated ions leaving the potential-lift. The kinetic energy of the ions was calculated from the sum of the voltages of the initial position and of the potential-lift. Therefore, the potential-lift increased the kinetic energy of the ions obviating the need to float the potential of the initial position or that of the TOF mass spectrometer.

The orthogonal acceleration type ESI ion source developed for ESI-TOF/TOF is shown in Fig. 5.4. It consisted of an ESI ion source (ESI ion source for AccuTOF, JEOL, Akishima, Japan), einzel lens, and OA-block. The OA-block was composed of a ground electrode, acceleration grid, and potential-lift. The $x$, $z$ coordinate system in the illustration was defined to interpret the ion trajectories in ESI-TOF/TOF. The $x$-axis was the direction of the ion beam from the ESI ion source, and the $z$-axis was perpendicular to this direction.

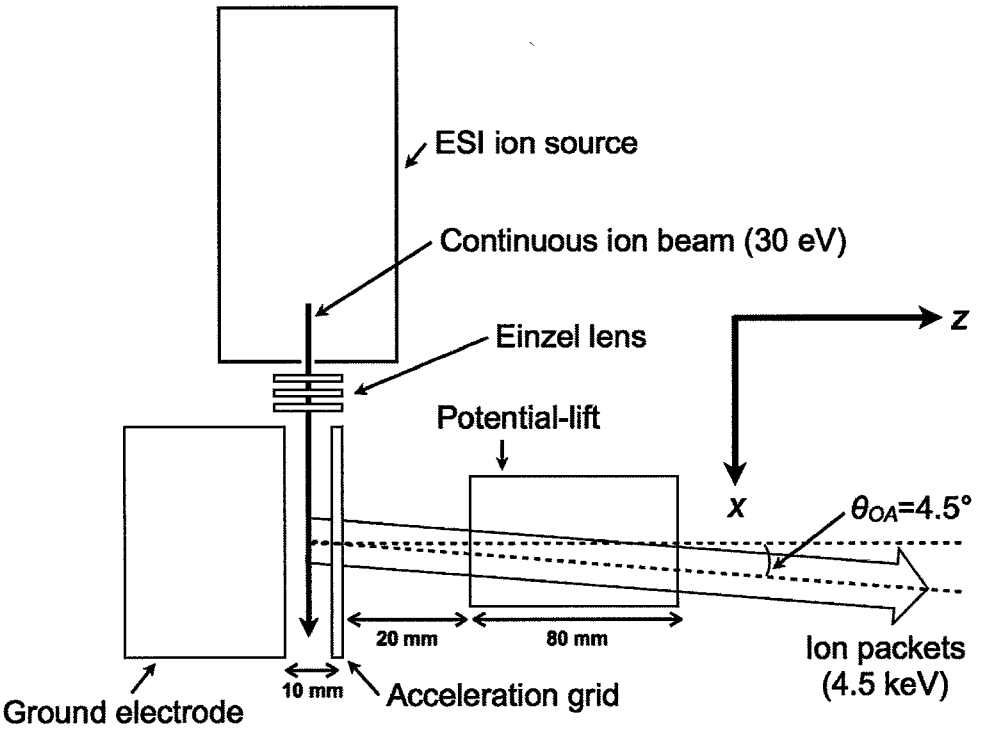


**Fig. 5.4.** Orthogonal acceleration type ESI ion source of ESI-TOF/TOF.

The samples were introduced into the ESI source by a syringe pump (No. 70-2205, Harvard apparatus, Ma, USA). The analyte ions traveled along an RF ion

guide system, which collisionally reduced their kinetic energies to less than 1 eV. They were accelerated toward the OA-block by the 30 V center potential of the RF ion guide. The ion beam from the RF ion guide was spatially focused by an einzel lens and introduced into the center of the 10-mm gap between the ground electrode and acceleration grid with a kinetic energy of 30 eV.

The schematic electric potentials of the OA-block ion are shown in Fig. 5.5, where the bold lines indicate the voltage of each component. The ground electrode and acceleration grid were both kept at 0 kV before the OA. A pulsed voltage of -1.0 kV applied to the acceleration grid accelerated the ion beam orthogonally as ion packets toward the potential-lift. The distance between the acceleration grid and potential-lift was 20 mm. The potential-lift consisted of one flight-tube electrode whose length and internal diameter were 80 and 45 mm, respectively. A high negative voltage of -5.0 kV was initially applied to the potential-lift. When an ion packet passed through the acceleration grid, it was accelerated by the difference in potential between the acceleration grid and the potential-lift. The voltage on the potential-lift was switched from -5.0 kV to ground potential (0 V) during the passage of the ions through the potential-lift, as shown in Fig. 5.5, without affecting the velocities of the ions: the analyte ions left the potential-lift region fully accelerated.

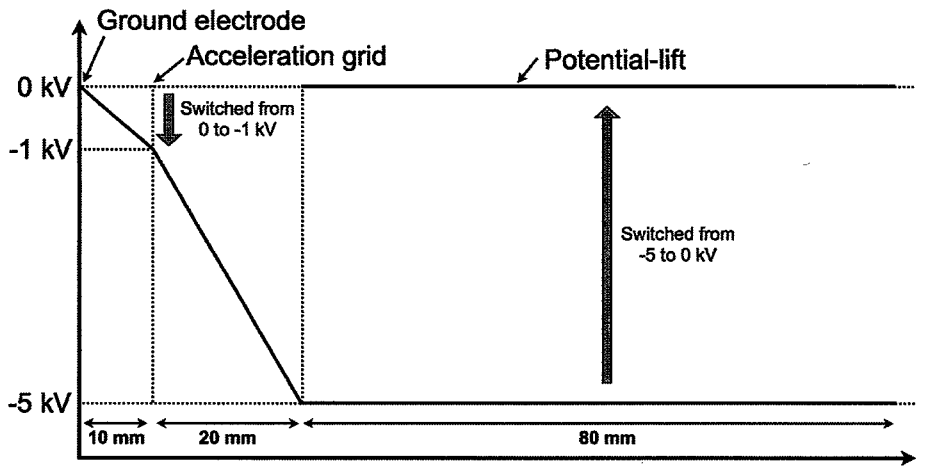


**Fig. 5.5.** Schematic electric potentials of the OA-block.

Therefore, it was possible to increase the kinetic energy of the ions without floating the potentials of the ESI ion source or the tandem TOF mass spectrometer. The kinetic

energy of the analyte ions was the sum of half the float voltage of the acceleration grid and the voltage of the potential-lift. One-half of the float voltage of the acceleration grid amounted to -0.5 kV, and the voltage of the potential-lift was -5.0 kV, implying that after passing through the potential lift, the kinetic energy of the ion packet reached 4.5 keV. The direction of the ion packet was inclined at approximately 4.5° with respect to the *z*-axis, and was given by the equation (5-1):

$$\theta_{OA} = \tan^{-1}\sqrt{30/4500} \qquad (5\text{-}1)$$

### 5.2.3 Linear TOF mass spectrometer (MS-1) and ion isolation

The linear TOF mass spectrometer was used as MS-1, which was a field-free region 160 mm long between the exit of potential-lift and the entrance to the collision cell. An ion gate, consisting of two square parallel plates of 10-mm width spaced 21 mm apart, was placed between the linear TOF mass spectrometer and the collision cell. One plate was always kept at ground potential, while the second plate was pulsed from +1 kV to ground with a pulse duration of 600 – 1000 ns. The minimum selection width for precursor ion selection was about 5 Da.

### 5.2.4 Collision cell for alkali metal and rare gas targets

A differentially pumped collision cell was placed between MS-1 and MS-2. This 37-mm-long cell was mounted in a vacuum chamber consisting of a perpendicular cylinder with an inner diameter of 63 mm and a height of 87 mm. The size of the collision cell is the same of the tandem magnetic sector mass spectrometer. The entrance hole of the collision cell was 10 mm wide and 1.5 mm high and the exit hole was 10 mm wide and 2 mm high. The position of the collision cell was adjusted using an *x*, *y*, and *z* coordinate positioning mechanism so that the incident ions did not collide with the exterior of either the entrance hole or the exit hole. The alkali metal target is introduced into the collision cell as a vapor from a reservoir. A number of different collision gases (He, Ne, Ar, Kr, Xe) can be used as collision gas by changing the same size of collision cell for rare gas target. The pressures were regulated with the use of a needle valve.

### 5.2.5 Quadratic-field ion mirror (MS-2)

A quadratic-field ion mirror was used to analyze fragment ions formed by collision with the rare gas target. In this apparatus, the potential $U$ changes along the optical axis $z$ of the instrument according to the equation (5-2):

$$U(z)=\frac{k}{2}(z-a)^2+C \tag{5-2}$$

where $k$ and $C$ are constants and $a$ is the value of $z$ at the position of the potential minimum. Interestingly, the TOF of ions in a quadratic-field mirror is given by the equation:

$$T=\pi\sqrt{\frac{m}{q}k} \tag{5-3}$$

where $q$ is the charge number. That is, the TOF in the quadratic-field ion mirror could in principle be made independent of the initial velocity of the ions and dependent only on the *m/z*. This meant that the quadratic-field ion mirror inherently achieved time focusing independent of the kinetic energy of the fragment ion, and could therefore simultaneously focus all the fragment ions with their different kinetic energies. Hence it was unnecessary to raise the potential of the collision cell in order to reduce the energy variation of fragment ions. Thus, ions accelerated in the ion source entered the collision cell without deceleration, i.e., high-energy CID operated effectively in this apparatus.

A schematic drawing and photograph of the quadratic-field ion mirror is shown in Fig. 5.6. This ion mirror was formed of four side walls made of polyimide boards and two anteroposterior aluminum plates. The front plate was rectangular, with a quadrilateral hole (30 mm wide and 62 mm high) for the ion beam incident on the ion mirror, and the back plate was planar, 60 mm wide and 121.5 mm high. The four polyimide boards were aligned and set in place using frames made of an aluminum alloy. Overall, the ion mirror was 136 mm wide, 80 mm high, and 536 mm long. Gold bands of specific shape were deposited on the polyimide boards. The bands were hyperbolic on the side boards (i.e., plates parallel to the $y-z$ plane) and linear on the top and bottom boards (i.e., plates parallel to the $x-z$ plane). The positions of the bands were determined and optimized by potential field calculations using the ion optics simulation program SIMION 3D™ version 8.0 (Scientific Instrument Services, Inc., NJ, USA). The electrodes were numbered 1 (front plate) to 67 (back plate), in order. The calculated distances of the bands are listed in Table 5.1. All the bands were 1.5 mm

wide. The field sustaining electrodes fell into three groups: electrodes 1–18 with a potential difference of 62.5 V, electrodes 18–30 with a potential difference of 125 V, and electrodes 30–67, at the end of the ion mirror, with a potential difference of 250 V. The final electrode at the rear part of the mirror was maintained at 12.00 kV. These potentials were generated using a chip resistor (RVC20, Kamaya Electric, Kawasaki, Japan) on the polyimide board.

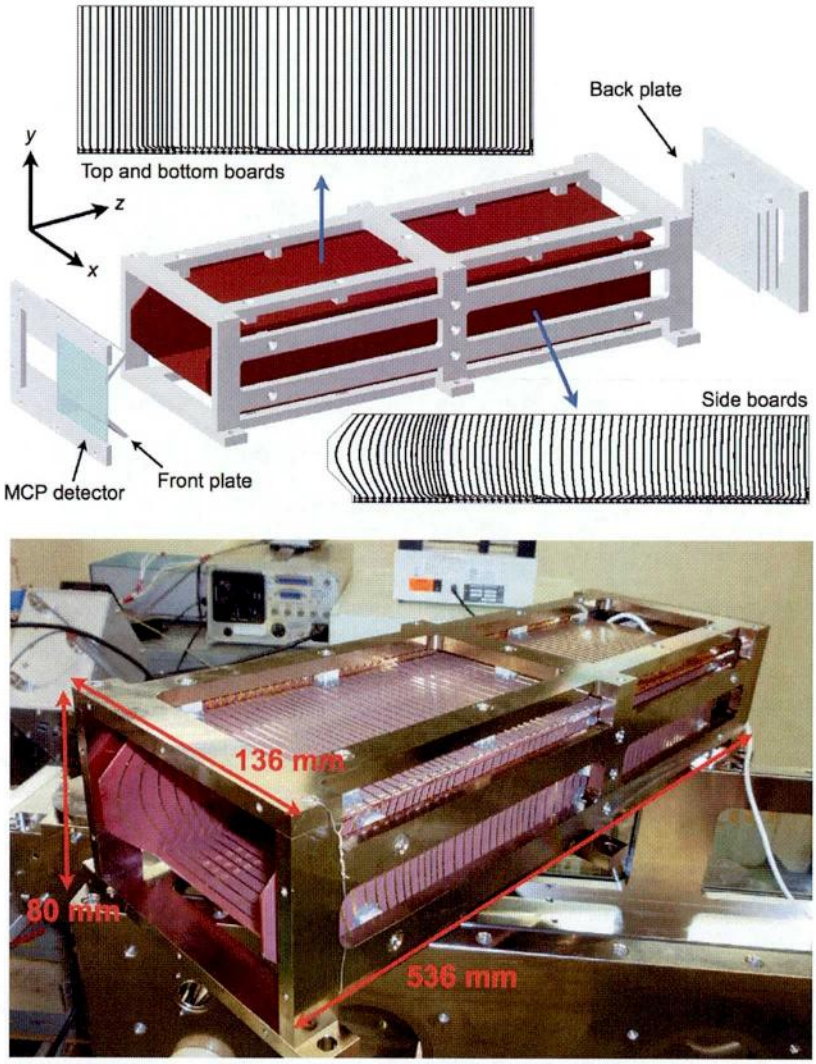


**Fig. 5.6.** A schematic drawing and photograph of the quadratic-field ion mirror.

The optimum distance between the exit of the collision cell and the mirror entrance was found to be about 78 mm. The ions entered the ion mirror from a position 58 mm from the center of the electrode. The ion mirror was tilted at 3.5° to the

horizontal plane in order to facilitate ion collection at the MCP detector (F1943-02, Hamamatsu Photonics, Hamamatsu, Japan). The dimensions of this detector were determined by ion optics simulations to be 81 mm (horizontal) × 31 mm (vertical), and it was fabricated under special order for use in this new ion mirror.

**Table 5.1.** The calculated distances of electrodes and applied voltages.

| Electrode number | Position of electrode (mm) | Distance between electrodes (mm) | Applied voltage (V) | Potential between electrodes (V) |
|---|---|---|---|---|
| 1 | 0 | | 0 | 62.5 |
| 2 | 23 | 23 | 62.5 | 62.5 |
| 3 | 36 | 13 | 125 | 62.5 |
| 4 | 47 | 11 | 187.5 | 62.5 |
| 5 | 57 | 10 | 250 | 62.5 |
| 6 | 65 | 8 | 312.5 | 62.5 |
| 7 | 73 | 8 | 375 | 62.5 |
| 8 | 80 | 7 | 437.5 | 62.5 |
| 9 | 86 | 6 | 500 | 62.5 |
| 10 | 93 | 7 | 562.5 | 62.5 |
| 11 | 99 | 6 | 625 | 62.5 |
| 12 | 104 | 5 | 687.5 | 62.5 |
| 13 | 110 | 6 | 750 | 62.5 |
| 14 | 115 | 5 | 812.5 | 62.5 |
| 15 | 120 | 5 | 875 | 62.5 |
| 16 | 125 | 5 | 937.5 | 62.5 |
| 17 | 130 | 5 | 1000 | 125 |
| 18 | 139 | 9 | 1125 | 125 |
| 19 | 147 | 8 | 1250 | 125 |
| 20 | 155 | 8 | 1375 | 125 |
| 21 | 163 | 8 | 1500 | 125 |
| 22 | 171 | 8 | 1625 | 125 |
| 23 | 178 | 7 | 1750 | 125 |

| | | | | |
|---|---|---|---|---|
| 24 | 185 | 7 | 1875 | 125 |
| 25 | 192 | 7 | 2000 | 125 |
| 26 | 198 | 6 | 2125 | 125 |
| 27 | 204 | 6 | 2250 | 125 |
| 28 | 211 | 7 | 2375 | 125 |
| 29 | 217 | 6 | 2500 | 250 |
| 30 | 228 | 11 | 2750 | 250 |
| 31 | 239 | 11 | 3000 | 250 |
| 32 | 250 | 11 | 3250 | 250 |
| 33 | 260 | 10 | 3500 | 250 |
| 34 | 270 | 10 | 3750 | 250 |
| 35 | 280 | 10 | 4000 | 250 |
| 36 | 289 | 9 | 4250 | 250 |
| 37 | 298 | 9 | 4500 | 250 |
| 38 | 307 | 9 | 4750 | 250 |
| 39 | 315 | 8 | 5000 | 250 |
| 40 | 323 | 8 | 5250 | 250 |
| 41 | 332 | 9 | 5500 | 250 |
| 42 | 340 | 8 | 5750 | 250 |
| 43 | 347 | 7 | 6000 | 250 |
| 44 | 355 | 8 | 6250 | 250 |
| 45 | 362 | 7 | 6500 | 250 |
| 46 | 370 | 8 | 6750 | 250 |
| 47 | 377 | 7 | 7000 | 250 |
| 48 | 384 | 7 | 7250 | 250 |
| 49 | 391 | 7 | 7500 | 250 |
| 50 | 398 | 7 | 7750 | 250 |
| 51 | 404 | 6 | 8000 | 250 |
| 52 | 411 | 7 | 8250 | 250 |
| 53 | 418 | 7 | 8500 | 250 |
| 54 | 424 | 6 | 8750 | 250 |
| 55 | 430 | 6 | 9000 | 250 |

| | | | | |
|---|---|---|---|---|
| 56 | 437 | 7 | 9250 | 250 |
| 57 | 443 | 6 | 9500 | 250 |
| 58 | 449 | 6 | 9750 | 250 |
| 59 | 455 | 6 | 10000 | 250 |
| 60 | 461 | 6 | 10250 | 250 |
| 61 | 467 | 6 | 10500 | 250 |
| 62 | 472 | 5 | 10750 | 250 |
| 63 | 478 | 6 | 11000 | 250 |
| 64 | 484 | 6 | 11250 | 250 |
| 65 | 489 | 5 | 11500 | 250 |
| 66 | 495 | 6 | 11750 | 250 |
| 67 | 502 | 7 | 12000 | |

### 5.2.6 Control program for measurements of high-energy CID and ETD spectra

A timing chart for the measurements in these high-energy CID experiments is shown in Fig. 5.7. A digital pattern generator (Model 555 pulse generator, Berkeley Nucleonics, Ca, USA) supplied the timing signals to the ion source, the ion gate, and the digital oscilloscope.

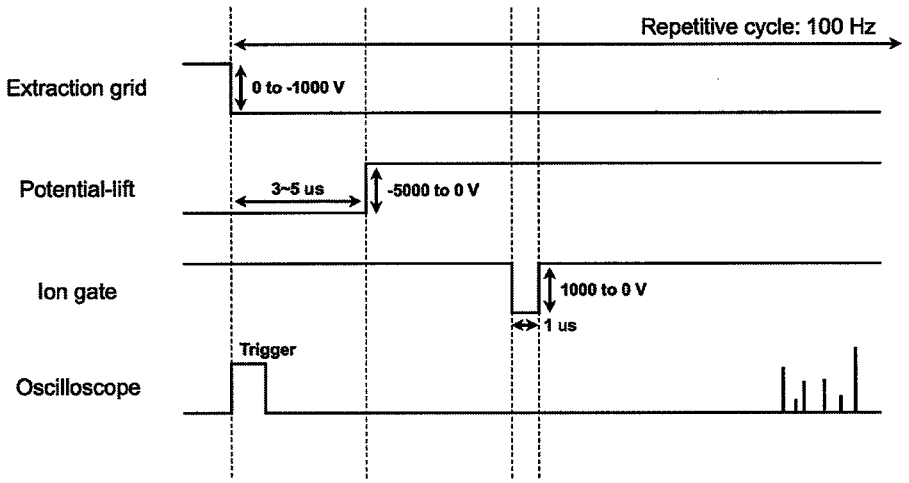


**Fig. 5.7.** A timing chart of the measurements in high-energy CID and ETD experiments.

The ions generated by ESI were directed to the potential-lift by applying a pulsed voltage to the extraction grid. The voltage on the potential-lift was switched from a negative voltage to ground potential during the passage of ions, as described earlier. Precursor ions were mass-selected by applying a pulsed voltage to the ion gate. Fragment ions formed by collision with the target gas were analyzed by the quadratic-field ion mirror and detected by the MCP detector. The TOF was recorded by a digital oscilloscope (LC564DL, LeCroy Japan, Osaka, Japan) coupled to a computer. The sampling rate of the digital oscilloscope was 2 GS/s. High-energy CID spectra were obtained from 5000 accumulations at a repetition frequency of 100 Hz.

**Sample preparation**

Water, methanol, and acetic acid were purchased from Wako Pure Chemical Industries, Ltd (Osaka, Japan). Two polypeptides, angiotensin II and bradykinin, were used to benchmark these high-energy CID experiments. Three polypeptides (angiotensin II, bradykinin, substance P) and a phosphopeptide (amino acid sequence:

MHRQETpVDC) were investigated for the evaluation of the high-energy ETD experiments. The polypeptides were obtained from Peptide Institute (Osaka, Japan). The phosphopeptide was synthesized by Toray research center (Tokyo, Japan). These peptides were used as obtained without further purification. For electrospray, 30 pmol/μL solutions in 49/49/2 methanol/water/acetic acid were prepared for each peptide, and were infused into an electrospray emitter at a flow rate of 1 μL/min.

## 5.3 Results and discussion

### 5.3.1 Precursor ion selection

The ESI-TOF spectra of angiotensin II are shown in Fig. 5.8. Before precursor ion selection, various ions were generated by ESI, as shown in Fig. 5.8(a), including doubly protonated angiotensin II (*m/z* 524.1).

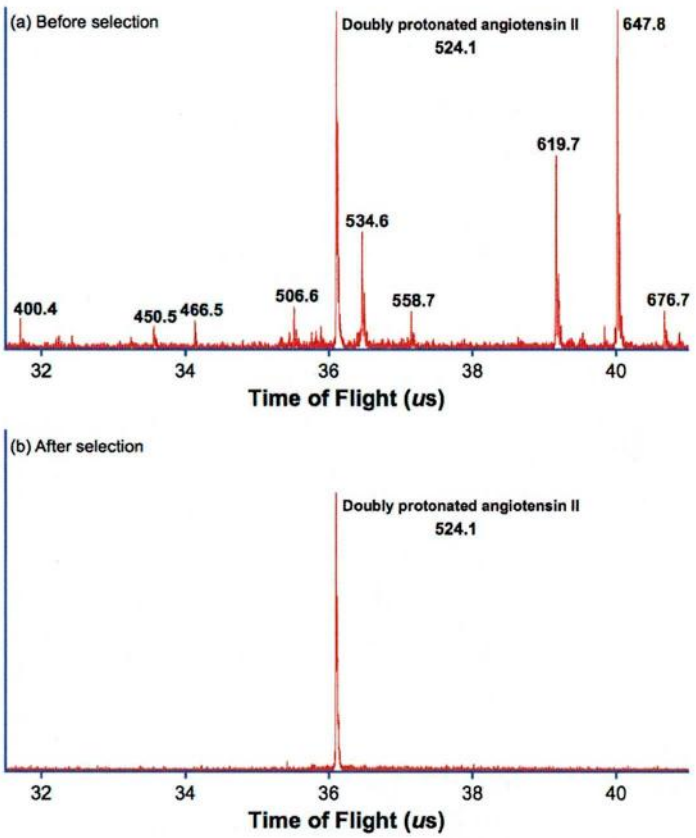


**Fig. 5.8.** ESI-TOF spectra of angiotensin II. (a) Before precursor ion selection, all the ions generated by ESI are included. (b) After precursor ion selection, the doubly protonated angiotensin II has been isolated by the ion gate.

After precursor ion selection, only the doubly protonated angiotensin II precursor ions were isolated by the ion gate, Fig. 5.8(b). However, the ion intensity in Fig. 5.8(b) was about 80% of that in Fig. 5.8(a) because of the low resolving power in precursor ion selection.

### 5.3.2 High-energy CID experiments

High-energy CID spectra of doubly protonated angiotensin II $[AngiotensinII+2H]^{2+}$ ($\equiv[M+2H]^{2+}$) and doubly protonated bradykinin $[Bradykinin]^{2+}$ ($\equiv[M+2H]^{2+}$) with the He target are shown in Fig. 5.9(a) and (b), respectively. The attenuation of the precursor ions in the high-energy CID spectra was 30%.

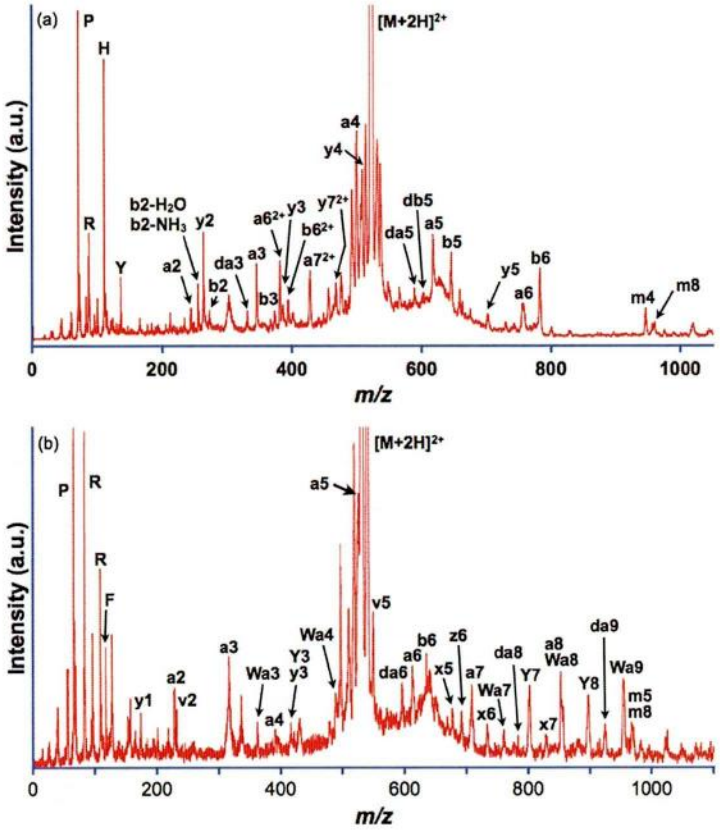


**Fig. 5.9.** High-energy CID spectra of doubly protonated angiotensin II and bradykinin with a helium target. The attenuations of precursor ions are 30%.

The peak of doubly protonated angiotensin II is seen at 524.1 in Fig. 5.9(a). A large number of singly charged fragments (*a*-, *b*-, *d*-, and *y*-types) and some doubly

charged fragments ($a^{2+}$-, $b^{2+}$-, and $y^{2+}$-types) were observed. These singly and doubly charged fragment ions were formed by the high-energy CID processes shown in Scheme (5-1) and Scheme (5-2), respectively.

**Scheme (5-1)**

$$AB^{2+} + He \rightarrow AB^{2+*} + He,$$
$$AB^{2+*} \rightarrow \text{N-terminal } A^{+} + \text{C-terminal } B^{+}.$$

**Scheme (5-2)**

$$AB^{2+} + He \rightarrow AB^{2+*} + He,$$
$$AB^{2+*} \rightarrow \text{N-terminal } A^{2+} + B \text{ (or } A + \text{C-terminal } B^{2+}).$$

In these schemes, $AB^{2+}$ is the $[M+2H]^{2+}$ ion. The excited species ($AB^{2+*}$) were produced from their corresponding positive ions ($AB^{2+}$) by collision with the He target. The fragment ions were formed from the dissociation of these excited species. These doubly charged precursor ions yielded singly charged fragment ions by the charge separation reactions shown in Scheme (5-1), and doubly charged fragment ions by the process detailed in Scheme (5-2). Among the singly charged fragment ions, *a*-type ions (*a*2-*a*6) were clearly observed, together with some *d*-type ions (*d*3 and *d*5) at lower intensity, as is characteristic of high-energy CID, which, for protonated peptides, usually results in more cleavages along the peptide chain compared to low-energy CID. In addition, high-energy CID may also result in amino-acid side-chain cleavages. It is well known that basic amino acids such as arginine, histidine, and lysine, when present at or near the peptide N terminus (angiotensin II has an arginine near the N terminus), result in a preponderance of *a*- and *d*-type fragment ions in the MS/MS spectrum [9-13]. In some cases, *d*-type ions can be used for the elucidation of isobaric amino acids (e.g., leucine and isoleucine) [9-13]. For example, the existence of *da*5 and *db*5 ions in Fig. 5.9(a) provided the information that the fifth amino acid from the N terminus of angiotensin II was not leucine but isoleucine. In the low mass region, some immonium ions could be seen. The appearance of these ions indicated the existence of particular amino acids in the structure. The presence of doubly charged ions ($a6^{2+}$, $a7^{2+}$, $b6^{2+}$, and $y7^{2+}$) indicated that the two protons were localized at the arginine and histidine, respectively, in angiotensin II. In fact, fragments such as *a*1 and *y*1 were not observed since these species were neutral. Although *y*2 fragments (expected to be neutral species since the two protons were localized at the arginine and histidine) were clearly observed, the *y*2 ions were formed by the facile amide bond cleavage on the N-terminal side of a

proline residue. This phenomenon is known as the proline effect [14-17]. Although protonation initially occurs at the most basic sites such as arginine, histidine, and lysine, collisional activation enables the proton to move to less basic sites along the peptide chain. Protonation of an amide nitrogen weakens the peptide bond, thereby promoting cleavage into *y*- or *b*-type ions. The proline amide nitrogen is the most basic of the amide nitrogens in a polypeptide and this accounted for the presence of *y*2 ions in these spectra.

The peak associated with doubly protonated bradykinin is seen at 531.1 in Fig. 5.9(b). As was seen in the high-energy CID spectrum of doubly protonated angiotensin II, a number of *a*-type fragment ions (*a*2-*a*8) together with some *d*-type fragment ions (*d*6, *d*8, *d*9) were clearly observed. In addition, the spectrum contained an abundance of C-terminal *w*-type fragment ions (*w*3, *w*4, *w*7-*w*9) and some *v*-type ions (*v*2 and *v*5). The series of *w*-type and *v*-type ions were formed from the side-chain losses of *z*-type ions and *y*-type ions, respectively, also characteristic of high-energy CID. These *w*-type ions, as well as *d*-type ions, are useful in distinguishing the isobaric amino acids. Some *b*-type, *x*-type, *y*-type, and immonium ions were also observed. The high intensities of *y*3, *y*7, and *y*8 ions were also attributed to the proline effect [14-17]. In contrast to angiotensin II, all fragment ions were singly charged species. Doubly charged fragment ions were not seen at all. That is, the fragment ions observed in the high-energy CID spectrum of bradykinin were formed by the process in Scheme (5-1). These results could be explained on the basis of the amino acid sequence of bradykinin. Two arginines (N-terminal and C-terminal) exist in bradykinin, and therefore any attached protons were expected to be localized at these termini. Thus when backbone cleavage occurred, only fragment ions containing one N- or C-terminal protonated arginine were observed. The protonation of both termini accounted for the lack of doubly charged fragment ions. The high-energy CID spectrum of doubly protonated bradykinin obtained here was markedly similar to a published spectrum obtained with a four sector mass spectrometer [18].

The foregoing results demonstrated that high-energy CID could provide complete sequence information for peptides. In addition, the collision energies attained in this study permitted the formation of *d*-, and *w*- ions, which were important in differentiating between isomeric amino acids. The present results indicated that high-energy CID could be performed in ESI-TOF/TOF. There have been no reports on

high-energy CID of multiply protonated peptides generated by ESI in a tandem TOF mass spectrometer.

### 5.3.3 High-energy ETD experiments

Next, high-energy ETD spectra of angiotensin II, bradykinin, and substance P with the Cs target are shown in Figs. 5.10(a)-(c), respectively.

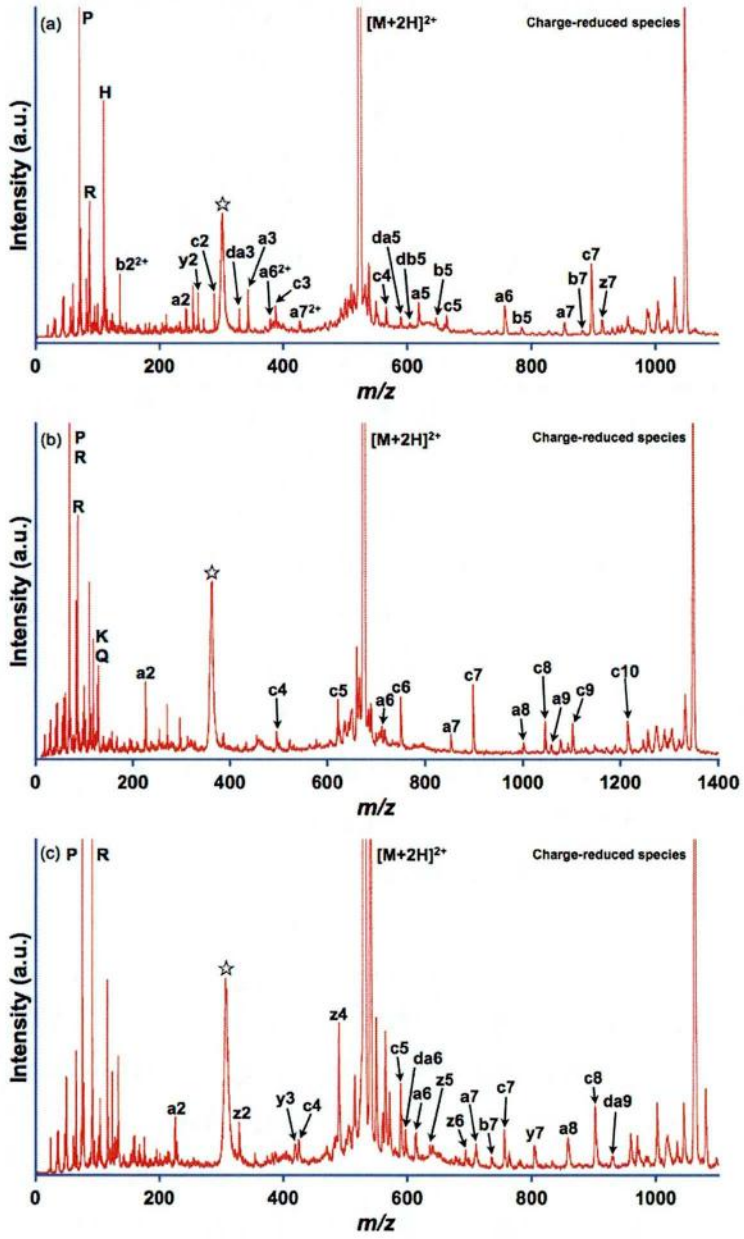


**Fig. 5.10** High-energy ETD spectra of doubly protonated polypeptides and phosphopeptide. (a) angiotensin II, (b) substance P, and (c) bradykinin.

In Fig. 5.10(a), the peak of the doubly protonated angiotensin II [AngiotensinII+2H]$^{2+}$ ($\equiv$[M+2H]$^{2+}$) was observed at 524.1. Several singly and doubly charged *a*-, *b*-, *d*-, and *y*-type ions were observed in Fig. 5.10(a). In some cases, *d*-type ions can be used for the elucidation of isobaric amino acids (e.g. leucine and isoleucine) [9-13]. For example, the existence of *da*5 and *db*5 ions in Fig. 5.10(a) offered the information that the fifth amino acid from N terminus in angioteinsin II was not leucine but isoleucine. In the low mass region, some of immonium ions could be seen. These fragment ions were also observed in the high-energy CID spectrum with the He target. It seems reasonable to conclude that these fragment ions in Fig. 5.10(a) resulted from the high-energy CID process. The fragment ion peaks associated with the charge-reduced species, which were not seen in the high-energy CID with the He target, were newly observed in Fig. 5.10(a). Additionally, it was also clearly seen that there was a strong enhancement of peaks corresponding to *c*-type fragment ions (*c*2-*c*4, *c*5, *c*7). These *c*-type ions were characteristic of ETD and ECD [19-25]. For this reason, it was concluded that these *c*-type fragment ions were formed by the high-energy ETD processes. Although the peaks corresponding to *c*6 were missing, it is noted that ETD and ECD are unable to break the amine backbone bonds on the N-terminal side of proline [19]. The predominance of N-terminal *c*-type fragment ions could be understood from the amino acid sequence of angiotensin II. The N-terminal amino acid is arginine that is likely to carry the charge since it is the most basic amino acid. Only the *z*7 ion was observed among *z*-fragment ions. This is because the C-terminal *z*-fragment ions including arginine is only *z*7 ions, then complementary *z*-type fragments except for *z*7 ions are hence neutral and can not be detected in this experiment.

Two more polypeptides have been investigated for the evaluation of the high-energy ETD experiments. The first one is substance P and it has a basic amino acid in the N terminus, as the case of angiotensin II. High-energy ETD spectrum of doubly protonated substance P [Substance P+2H]$^{2+}$ ($\equiv$[M+2H]$^{2+}$) with the Cs target is shown in Fig. 5.10(b). The peak associated with doubly protonated substance P are at 675.3. The spectrum contains a dominating series of *c*-type fragment ions from *c*4 to *c*10 along with the charge-reduced species. The series of *c*-ions could be also understood from the amino acid sequence of substance P. Several *a*-type ions were also observed, as in the case of angiotensin II.

The second one is bradykinin with two basic amino acid in both the N and C terminuses. High-energy ETD spectrum of doubly protonated bradykinin $[Bradykinin+2H]^{2+}$ ($\equiv[M+2H]^{2+}$) with the Cs target is shown in Fig. 5.10(c). Not dissociated $[M + 2H]^{2+}$ is at *m/z* 531.1. As seen above two spectra of angiotensin II and substance P, the charge-reduced species was the dominating peak. Additionally, in contrast to the cases of angiotensin II and substance P, both *c*-type fragment ions (*c*4-*c*5, *c*7, *c*8) and their complementary *z*-type fragment ions (*z*2, *z*5-*z*6) were observed. This phenomenon can be explained by the presence of two arginine amino acids (N-terminal and C-terminal) in the bradykinin.

Finally, in order to test the ability of high-energy ETD, doubly protonated phosphopeptide $[Phosphopeptide+2H]^{2+}$ ($\equiv[M+2H]^{2+}$) were investigated. High-energy ETD spectrum of the doubly protonated phosphopeptide with the Cs target are shown in Fig. 5.11. Six *c*-type ions (*c*3-*c*8) and two *z*-type ions (*z*7, *z*8), which preserved the phosphate group, were clearly observed. The position of phosphate groups and amino acid sequence of this phosphopeptide could be determined by the space of the fragment ion peaks of *c*- and *z*-type fragment ions.

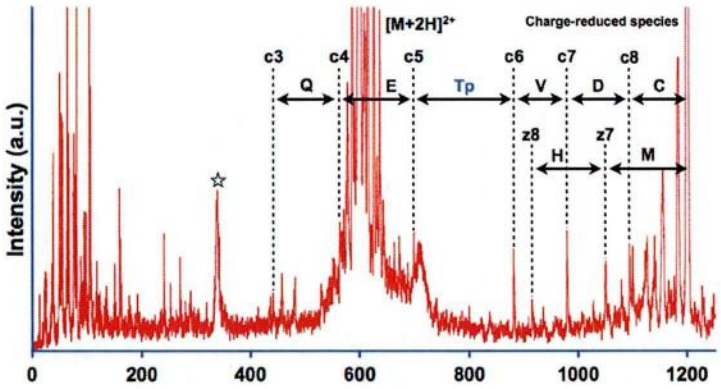


**Fig. 5.11** High-energy ETD spectrum of doubly protonated phosphopeptide.

The present experimental results are summarized as follows. In all the high-energy ETD spectra with the Cs target, *c*- and *z*-type fragment ions were clearly observed. These results led us to the conclusion that high-energy ETD experiments could be performed in ESI-TOF/TOF. There have been no report on high-energy ETD of multiply protonated peptide generated by ESI in a tandem TOF mass spectrometer. Unfortunately, although high intensity peaks, which are indicated with stars above the

peaks in each spectrum, were observed in all the spectra, they have been not identified. These unknown peaks remain a matter of research.

Although the sensitivity (ca. 200 pmol of sample consumed) and mass resolution in fragment ion separation (FWHM: 1000) of ESI-TOF/TOF were modest, ESI-TOF/TOF showed great promise for the analysis of biological samples.

## References


[1] A.W. Colburn, A.E. Giannakopulos, P.J. Derrick, M. Von Raumer, Eur. J. Mass Spectrom. 6 (2000) 523.

[2] Y. Yoshida, U.S. Patent. No. 4,625,112 (November 25, 1986).

[3] J.H.J. Dawson, M. Guilhaus, Rapid Commun. Mass Spectrom. 3 (1989) 155.

[4] O.A. Mirgorodskaya, A.A. Shevchenko, I.V. Chernushevich, A.F. Dodonov, A.I. Miroshnikov, Anal. Chem. 66 (1994) 99.

[5] K. Iwamoto, H. Nagao, M. Toyoda, Eur. J. Mass. Spectrom. (Chichester, Eng) 15 (2009) 249.

[6] M. Ishihara, Japan Patent. No. 3,354,427, September 27 (2002)

[7] D. Okumura, K. Kumondai, S. Yamaguchi, M. Toyoda, M. Ishihara, I. Katakuse, J. Mass Spectrom. Soc. Jpn. 48 (2000) 357.

[8] D. Suckau, A. Resemann, M. Schuerenberg, P. Hufnagel, J. Franzen, A. Holle, Anal. Bioanal Chem. 376 (2003) 952.

[9] K. Biemann, S.A. Martin. Mass Spectrom. Rev. 6 (1987) 1.

[10] R.S. Johnson, S.A. Martin, K. Biemann, Int. J. Mass Spectrom. Ion Process. 86 (1988) 137.

[11] R.A.J. O'Hair, M.L. Styles, G.E. Reid, J. Am. Soc. Mass Spectrom. 9 (1998) 1275.

[12] I.A. Papayannopoulos, Mass Spectrom. Rev. 14 (1995) 49.

[13] J.T. Stults, J. Lai, S. McCune, R. Wetzel, Anal. Chem. 65 (1993) 1703.

[14] G.E. Reid, J. Wu, P.A. Chrisman, J.M. Wells, S.A. McLuckey, Anal. Chem. 73 (2001) 3274.

[15] J.A. Loo, C.G. Edmonds, R.D. Smith, Anal. Chem. 65 (1993) 425.

[16] B.L. Schwartz, M.M. Bursey, Biol. Mass Spectrom. 21 (1992) 92.

[17] T. Vaisar, J. Urban, J. Mass Spectrom. 31 (1996) 1185.

[18] K.M. Downard, K. Biemann, J. Am. Soc. Mass Spectrom. 5 (1994) 966.

[19] R.A. Zubarev, N.L. Kelleher, F.W. McLafferty, J. Am. Chem. Soc. 120 (1998) 3265.

[20] R.A. Zubarev, N.A. Kruger, E.K. Fridriksson, M.A. Lewis, D.M. Horn, B.K. Carpenter, F.W. McLafferty, J. Am. Chem. Soc. 121 (1999) 2857.

[21] R.A. Zubarev, D.M. Horn, E.K. Fridriksson, N.L. Kelleher, N.A. Kruger, M.A. Lewis, B.K. Carpenter, F.W. McLafferty, Anal. Chem. 72 (2000) 563.

[22] R.A. Zubarev, Mass Spectrom. Rev. 22 (2003) 57.

[23] J.E.P. Syka, J.J. Coon, M.J. Schroeder, J. Shabanowitz, D.F. Hunt, Proc. Natl. Acad. Sci. U. S. A. 101 (2004) 9528.

[24] J.J. Coon, J.E.P. Syka, J.C. Schwartz, J. Shabanowitz, D.F. Hunt, Int. J. Mass Spectrom. 236 (2004) 33.

[25] P.A. Chrisman, S.J. Pitteri, J.M. Hogan, S.A. McLuckey, J. Am. Soc. Mass Spectrom. 16 (2005) 1020.

# Chapter 6

## Summary

A tandem sector mass spectrometer for high-energy ETD was developed as a prototype instrument of ESI-TOF/TOF in order to improve the high-energy CID efficiency of MALDI-TOF/TOF.

Dissociation of inorganic ions induced by collision with rare gas targets and alkali metal targets were investigated. In the investigation of unimolecular dissociation and high-energy CID of $Ag_xBr^+$ ($x$ = 2, 4, 6, 8, 10) clusters, the difference in the relative intensities of the $Ag_{x-1}^+$ peaks between unimolecular dissociation and CID spectra led us to conclude that the weakest bond in the excited cluster $Ag_xBr^{+*}$ is the $Ag_{x-1}^+$–AgBr bond and the structure of $Ag_xBr^+$ is a metallic $Ag_{x-1}^+$ ion cluster adduct with AgBr. In addition, the primary fragments observed in the CID spectra were also explained by the stabilities of the generated ion products and neutral fragments, both having even delocalized valence electrons. In the investigation of various dissociation channels of silver bromide cluster ion $Ag_2Br^+$ and silver cluster ion $Ag_3^+$ using the Cs target, the difference in the fragment patterns between the high-energy CID and the other dissociation methods was explained in terms of the internal energy distributions. The dissociation mechanisms of neutral silver bromide cluster $Ag_2Br$ and silver cluster $Ag_3$ were also investigated by charge inversion mass spectrometry using the Cs target. The dissociation behavior of $Ag_2Br^*$ can be explained on the basis of the calculated thermochemical data. Contrary to this, the predominant existence of the undissociated $Ag_3^-$ cannot be explained by the reported thermochemical data. The existence of undissociated $Ag_3^-$ suggests that the dissociation barrier is higher than the internal energy of $Ag_3^*$ estimated from the ionization potentials of $Ag_3$ and Cs. In the investigation of high-energy ETD of doubly charged tungsten hexacarbonyl $W(CO)_6^{2+}$ ions using alkali metal targets (K and Cs), the internal energy deposition resulting from the electron transfer with the Cs target was very narrow and centered at a particular energy, 8.2 eV above the energy level of the charge reduced $W(CO)_6^+$ ion, which was higher than 7.2 eV with the K target. These internal energies correspond to energy differences of 2.9 and 3.5 eV between the entrance channel of $W(CO)_6^{2+}$ + Cs (or K) and the exit channel of $W(CO)_6^{+*}$ + $Cs^+$ (or K+), respectively. The internuclear

separation of the Landau–Zener potential crossing of the electron transfer between a $W(CO)_6^{2+}$ ion and the Cs target was evaluated as 6.8 Å~$10^{-8}$ cm, which was larger than the value for the K target (5.9 Å~$10^{-8}$ cm). The difference in the cross sections between K and Cs target indicates that a target having lower ionization energy is more effective for electron transfer.

These measurement results indicated that this instrument has a potential to obtain high-energy ETD spectra of biomolecular ions. Before high-energy ETD experiments of biomolecular ions, the instrument was improved because the sensitivity and mass range of this instrument are poor and narrow to obtain high-energy ETD spectra of the biomolecular ions, respectively. The ion intensity after the improvement became over ten times higher than that before the improvement. In addition while only the fragment ions with *m/z* 600 to 1400 are observed in the MS/MS spectrum before the improvement, the fragment ions with *m/z* 0 to 1400 are observed in MS/MS spectrum after the improvement. After the improvement, high-energy ETD of polypeptides and phosphopeptides were investigated. Doubly protonated angiotensin II ions obtained by ESI were collided with Xe and Cs targets to give singly and doubly charged positive ions via high-energy CID and ETD. Whereas doubly charged fragment ions resulting from CID were dominant in the high-energy CID spectrum with the Xe target, singly charged fragment ions resulting from ETD were dominant in the high-energy ETD spectrum with the Cs target. The most intense peak resulting from ETD was estimated to be associated with the charge-reduced ion. Five *c*-type fragment ions with amino acid residues detached consecutively from the C-terminal were clearly observed. These ions must be formed by N–C$\alpha$ bond cleavage, in a manner similar to the cases of electron capture dissociation (ECD) and ETD from negative ions. The present results demonstrated that high-energy ETD allowed determination of the amino acid sequence of the polypeptides. In addition, the high-energy ETD efficiency was about 6 times higher than high-energy CID efficiency. High-energy ETD spectra of doubly protonated phosphopeptides could be obtained. In all spectra, *c*- and *z*-type fragment ions formed by high-energy ETD were clearly observed. These results indicated that high-energy ETD is useful in determining the amino acid sequence and the position of phosphoric acid of phosphopeptides.

The mass resolution and sensitivity of the tandem sector mass spectrometer were not enough to measure larger biological molecules, although high-energy ETD is useful

in the structural analysis of biomolecular ions. Therefore a tandem time-of-flight mass spectrometer with ESI ion source "ESI-TOF/TOF" was newly developed in order to improve the mass resolution and sensitivity. The present results indicated that high-energy CID and ETD could be performed in ESI-TOF/TOF, and then the mass resolution and sensitivity could be improved. There have been no reports on high-energy CID and ETD of multiply protonated peptides generated by ESI in a tandem TOF mass spectrometer. Although the sensitivity (ca. 200 pmol of sample consumed) and mass resolution in fragment ion separation (FWHM: 1000) of ESI-TOF/TOF were modest, ESI-TOF/TOF showed great promise for the analysis of biological samples.

## List of Achievements

1. Original Articles (Main)

(1) S. Hayakawa, K. Minami, K. Iwamoto, M. Toyoda, T. Ichihara and H. Nagao: Potential crossing position in electron transfer of a doubly charged ion and alkali metal target measured using thermometer molecule $W(CO)_6$., *Int. J. Mass Spectrom.*, **266** (2007) 122-128.

(2) 新間秀一, 長尾博文, 豊田岐聡: Charge-remote fragmentation of phospholipids by high energy CID in a multi-turn tandem time-of-flight mass spectrometer "MULTUM-TOF/TOF"., *J. Mass Spectrom. Soc. Jpn.*, **343** (2007) 343-351.

(3) H. Nagao, K. Awazu, S. Hayakawa, K. Iwamoto, M. Toyoda, and T. Ichihara: Dissociation channels of silver bromide cluster $Ag_2Br$, silver $Ag_3$ and their ions studied by using alkali metal target., *Eur. Phys. J. D.*, **45** (2007) 279-287.

(4) S. Shimma†, H. Nagao†, Anastassios E. Giannakopulos, S. Hayakawa, K. Awazu, and M. Toyoda: High-energy collision-induced dissociation of phosphopeptides using a multi-turn tandem time-of-fliss spectrometer "MULTUM-TOF/TOF"., *J. Mass Spectrom.*, **43** (2008) 535-537.

†These authors equally contributed to this work

(5) S. Hayakawa, M. Hashimoto, H. Nagao, K. Awazu, M. Toyoda, T. Ichihara and Y. Shigeri: Study of the dissociation of charge-reduced phosphopeptide formed by electron transfer from alkali metal target., *Rapid Commun. Mass Spectrom.*, **22** (2008) 567-572.

(6) K. Iwamoto, H. Nagao, M. Toyoda: Development of an ion trap/multi-turn time-of-flight mass spectrometer with potential-lift., *Eur. J. Mass Spectrom.*, **22** (2009) 249-260.

(7) H. Nagao, M. Toyoda, S. Hayakawa, K. Iwamoto, T. Ichihara, K. Kawamura, and K. Awazu: Unimolecular and collision-induced dissociation of singly charged mono-bromide silver clusters $Ag_xBr^+$ ($x$ = 2, 4, 6, 8, 10)., *Eur. J. Mass Spectrom.*, **15** (2009) 459–469.

(8) 長尾博文, 早川滋雄, 橋本雅美, 岩本賢一, 豊田 岐聡, 茂里康, 地頭所眞美子, 粟津邦男: Development of MS/MS instrument providing high-energy electron transfer dissociation., *J. Mass Spectrom. Soc. Jpn.*, **57** (2009) 123-132.

2. Original Articles (Related)

(1) H. Hazama, H. Nagao, R. Suzuki, M. Toyoda, K. Masuda, Y. Naito, and K. Awazu: Comparison of mass spectra of peptides in different matrices using matrix-assisted laser desorption/ionization and a multi-turn time-of-flight mass spectrometer, MULTUM-IMG., *Rapid Commun. Mass Spectrom.*, **22** (2008) 1461–1466.

(2) H. Hazama, J. Aoki, H. Nagao, R. Suzuki, T. Tashima, K. Fujii, K. Masuda, K. Awazu, M. Toyoda, Y. Naito: Construction of a Novel Stigmatic MALDI Imaging Mass Spectrometer., *Applied Surface Science.* **255** (2008) 1257-1263.

3. Award

(1) 優秀論文賞（第 55 回質量分析総合討論会）共同受賞：「川村和哉，久保歩，長尾博文，石原盛男，豊田岐聡：MULTUM-TOF/TOF を用いたチャージリモートフラグメンテーションの確認」

(2) 2008 年度 BMS トラベルアワード（日本質量分析学会 BMS 研究会）受賞:「長尾博文:アルカリ金属ターゲットを用いたリン酸化ペプチドの電子移動解離」

## Acknowledgement

This study was carried out under the guidance of Prof. Kunio Awazu, the head of Medical Beam Physics Laboratory, Division of Sustainable Energy and Environmental Engineering, Graduate School of Engineering, Osaka University. The author would like to express my great appreciation to Prof. Kunio Awazu for his guidance, encouragement, many valuable advices and continuous supports.

The author would like to express my appreciation to the reviewers of this thesis, Prof. Hiroshi Horiike and Shigehiro Nishijima, Division of Sustainable Energy and Environmental Engineering, Graduate School of Engineering, Osaka University, for their valuable advices. The author would like to express my special appreciation to the reviewer of this thesis, Associate Prof. Michisato Toyoda, Mass spectrometry laboratory, Department of Physics, Graduate School of Science, Osaka University, for the valuable advice and instructing many experimental ideas and techniques during a course of study.

The author would like to express my thanks to the staffs of Medical Beam Physics Laboratory, Dr. Katsunori Ishii, Dr Takaya Terada, Ms. Masako Kudo, Ms. Takako Tajiri, and Ms. Noriko Hattori for their scientific cooperation, valuable advices, and encouragement. The author also would like to express my special thanks to former staffs, Dr. Sachiko Suzuki, for her cooperation and encouragement.

The author would like to express my appreciation to Dr. Toshihiro Kushibiki and Dr. Hisanao Hazama, Frontier Research Center, Graduate School of Engineering, Osaka University, for his scientific cooperation and valuable advices.

The author would like to express the staffs of Mass spectrometry laboratory, Department of Physics, Graduate School of Science, Osaka University. The author would like to express my special appreciation to Associate Prof. Morio Ishihara for the valuable advice and instructing ion optics and many useful suggestions. The author would like to express my special thanks to the staffs, Dr. Jun Aoki, Dr. Shuichi Shimma, and Dr. Shingo Ebata for helpful discussion and encouragement. The author wishes to express the sincere gratitude to Mr. Toshio Ichihara for technical supports and useful advice.

The author would like to express my special appreciation to Prof. Shigeo Hayakawa and Assistant Prof. Kenichi Iwamoto, Department of Chemistry, Graduate School of Science, Osaka Prefecture University, for their technical cooperation in the

experiments.

The author would like to express my special appreciation to Dr. Yoshinao Wada, Osaka Medical Center and Research Institute for Maternal and Child Health, for the technical cooperation in the ETD experiments using the LTQ-XL.

The author would like to express my special appreciation to Dr. Yasushi Shigeri, National Institute of Advanced Industrial Science and Technology, for providing the samples and scientific cooperation.

The author would like to express my special thanks to Dr. Toshio Tashima, Central Pharmaceutical Research Institute, JAPAN TOBACCO INC., for advice on sample preparation and helpful discussion.

The author would like to express my special thanks to Prof. Yasuo Nozue, Department of Physics, Graduate School of Science, Osaka University, for helpful discussion and encouragement.

The author would like to express my special thanks to the students of Medical Beam Physics Laboratory and Mass spectrometry laboratory, for their cooperation and encouragement.

Finally, the author would like to express my appreciation to my parents, Ken and Hiroko, for their daily support.

March, 2010.

Hirofumi Nagao